DISSERTATION

Hydrothermal synthesis as green route towards amide- and imidazole-based organic materials

This dissertation was carried out for the
purpose of obtaining the academic degree of a
Doctorate in Natural Sciences

under the supervision of
Prof. Dipl.-Chem. Dipl.-Ing. Dr.rer.nat. Miriam M. Unterlass, MSc.
Department of Chemistry at Universität Konstanz

submitted to the
Technische Universität Wien
Fakultät für Technische Chemie

by
Mohamed Musthafa Iqbal
011802397

Wien, 05 June 2024

Abstract

In order to enable the development of future technologies, it is essential to create new materials with adjustable properties. In many cases it is of paramount importance that these materials are not only functional but also lightweight and highly resistant towards various external influences. Organic high-performance materials (HPMs) are highly sought after to meet these requirements, as they are composed of abundant, lightweight elements that form stable moieties. However, the synthesis of organic HPMs typically requires harsh and harmful conditions.

In recent years, it has been successfully demonstrated that so-called hydrothermal (HT) conditions allow to directly synthesize highly crystalline low-molecular weight carbonyl dyes as well as linear polyimides. Enhancing the crystallinity of an organic HPM by applying such a "green" strategy is not only highly intriguing but also of significant importance for a multitude of practical applications. In general, the thermal and chemical stability of materials improves with increasing crystallinity, allowing the materials to withstand more extreme working conditions.

Due to their ability to generate outstandingly high crystallinity in organic low-molecular weight compounds as well as linear polymers, HT methods can also be considered as highly promising for realizing crystalline frameworks and conjugated ladder polymers.

In this thesis, the development and synthesis of crystalline frameworks and conjugated ladder polymers using three different linkages were achieved through HT method.

The goal of the first and second part was to synthesize crystalline frameworks with benzimidazole and amide linkages using HT synthesis. It was observed that under HT conditions, crystalline and thermally stable polyamide and polybenzimidazole materials were produced. However, instead of achieving long-range extended frameworks, the synthesis led to the formation of short-range fused macrocycle structures.

The third part focused on the preparation of conjugated ladder polymers with imidazopyrrolone linkages using HT synthesis. The synthetic procedure was modified by incorporating microwave (MW) synthesis, resulting in a faster and less tedious synthesis process that yielded thermally stable, processable, yet amorphous polymers.

In summary, this thesis aims to develop "green" and innovative pathways toward organic HPMs with various linkages using only water under high-temperature and high-pressure conditions.

Kurzfassung

Um die Entwicklung zukünftiger Technologien zu ermöglichen, müssen neue Materialien mit einstellbaren Eigenschaften entwickelt werden. Organische Hochleistungsmaterialien (HPMs) sind sehr gefragt, um diese Anforderungen zu erfüllen, da sie aus reichlich vorhandenen, leichten Elementen bestehen, die stabile Einheiten bilden. Die Synthese von organischen HPMs erfordert jedoch in der Regel raue und schädliche Bedingungen.

In den letzten Jahren wurde erfolgreich nachgewiesen, dass sich unter sogenannten hydrothermalen (HT) Bedingungen hochkristalline niedermolekulare Carbonylfarbstoffe sowie lineare Polyimide direkt synthetisieren lassen. Im Allgemeinen verbessert sich die thermische und chemische Stabilität von Materialien mit zunehmender Kristallinität, so dass die Materialien auch extremeren Arbeitsbedingungen standhalten können.Aufgrund ihrer Fähigkeit, organische Verbindungen mit niedrigem Molekulargewicht sowie lineare Polymere mit außergewöhnlich hoher Kristallinität zu erzeugen, gelten HT-Methoden auch als vielversprechend für die Herstellung von kristallinen Gerüsten und konjugierten Leiterpolymeren.

In dieser Dissertation wurde die Entwicklung und Synthese von kristallinen Gerüsten und konjugierten Leiterpolymeren mit drei verschiedenen Bindungen durch HT-Methoden erreicht.

Das Ziel des ersten und zweiten Teils war die Synthese von kristallinen Gerüsten mit Benzimidazol- und Amidbindungen unter Verwendung von HT synthese. Es wurde festgestellt, dass unter HTP-Bedingungen kristalline und thermisch stabile Polyamid- und Polybenzimidazolmaterialien hergestellt wurden. Allerdings führte die Synthese nicht zu langreichweitigen ausgedehnten Gerüsten, sondern zur Bildung von kurzreichweitigen kondensierten Makrozyklusstrukturen.

Der dritte Teil befasste sich mit der Herstellung von konjugierten Leiterpolymeren mit Imidazopyrrolon-Bindungen unter Verwendung von HT synthese. Das Syntheseverfahren wurde durch die Einbeziehung der Mikrowellensynthese (MW) modifiziert, was zu einem schnelleren und weniger langwierigen Syntheseprozess führte, der thermisch stabile, verarbeitbare und dennoch amorphe Polymere ergab.

Zusammenfassend lässt sich sagen, dass diese Dissertation darauf abzielt, "grüne" und innovative Wege zu organischen HPMs mit verschiedenen Verknüpfungen zu entwickeln, die nur Wasser unter Hochtemperatur- und Hochdruckbedingungen verwenden.

Acknowledgement

First and foremost, I would like to express my deepest gratitude to Prof. Miriam Unterlass for her scientific guidance, for her understanding in all matters and for her unparalleled support. These have been very productive years in which I have developed both as researcher and personally.

I would also like to thank IMC and TU Wien for the infrastructure, library facilities, research facilities and for exposing myself to the working environment of a full–fledged research institute. I acknowledge the financial support from Austrian Science Fund (FWF) under the grant "HYDROCOF" (START Y1037-N28).

I am so extremely thankful to my colleagues from UnterlassLab, Michael, Tobia, Elias, Fabian, Marianne, Patrick, Eleonora, Lukas, Alonso, Hipassia and Marwan for making the lab lively and lending a hand at times when I needed. Their support, assistance, and intellectual input during critical moments were indispensable for the completion of this dissertation.

I am thankful to all those who supported me with the measurements and their technical knowledge including Werner Artner for help in PXRD analytics, Prof. Karin Föttinger and Dr. Nevzat Yigit for help in surface area measurements, Dr. Michael Puchberger for ^{13}C-NMR measurements, Prof. Herwig Peterlik for SAXS measurements, Prof. Katharina Schröder and Dr. Aitor Martinez for $scCO_2$ experiments, Prof. Arne Thomas and Dr. Jérôme Roeser for crystal framework simulations, gas sorption measurements and many fruitful discussions. I am also grateful for the support from my current employer, AC2T research GmbH and my new colleagues during the thesis writing phase.

I convey my warm appreciation and most respectful regards to my thesis examiners for their valuable suggestions and comments.

I express my immense love and affection to my parents, Iqbal and Sabeena, as well as to my partner Najma, my sister Fathima and my grandparents for all their unconditional love and support which I have always received. I am grateful to my dear friends Athul, Aarathy, Hari, Anju, Kathu, Ashish, Thapasya, Sreejith, Parvathy, Swathi and all others who motivated me and made my time in Vienna a true pleasure. Finally, I praise and thank the almighty for being the unfailing source of support, comfort and strength throughout the completion of my project work.

<div align="right">Mohamed Musthafa Iqbal</div>

"To my parents, who always believed in me"

"In loving memory of my grandfather,
who planted the seed of curiosity in my mind and nurtured it."

Contents

List of Figures

iii

List of Tables

List of Schemes

List of Abbreviations and Symbols

Abbreviations

^{13}C CP-MAS	^{13}C cross polarization magic angle spinning
2D	two dimensional
3D	three dimensional
6FDA	4,4-(Hexafluoroisopropylidene) diphthalic anhydride
AC	non-stirred steel autoclave
Amp	sealed glass ampoule
ATR	Attenuated total reflectance
BE	Binding energy
BET	Brunauer-Emmett- Teller
BTDA	3,3′,4,4′-Benzophenonetetracarboxylic dianhydride
Bz	Benzidine / 1,1'-biphenyl-4,4'-diamine
CAF	Covalent amide framework
CMP	Conjugated microporous polymers
COF	Covalent organic framework
CP	Critical point
CTF	Covalent triazine framework
DABz	3,3'-Diaminobenzidine
DCC	Dynamic covalent chemistry
DMAc	Dimethylacetamide
DMF	Dimethyl formamide
DMSO	Dimethyl sulfoxide
EtOH	Ethanol
FT-IR	Fourier transform infrared spectroscopy
HCP	Hypercrosslinked polymers
HOAc	Acetic acid
HPP	High-performance polymer
HT	Hydrothermal
HTP	Hydrothermal polymerization
HTW	High-temperature water

IUPAC	International Union of Pure and Applied Chemistry
MeOH	Methanol
MOF	Metal organic framework
MW	Microwave
NMP	N-methyl pyrrolidone
OPDA	o-phenylene diamine
PAM	Polyamide material
PBI	Polybenzimidazoles
PBIM	Polybenzimidazole material
PI	Polyimide
PIM	Polymers of intrinsic microporosity
POP	Porous organic polymers
PPPI	poly(p-phenylene pyromellitimide)
PPy	Polybenzimidazopyrrolones / Polypyrrolones
PXRD	Powder X-ray diffraction
RT	Room temperature
SAED	Selected area electron diffraction
SAXS	Small angle X-ray scattering
scCO$_2$	Supercritical carbon dioxide
SEM	Scanning Electron Microscope
ssNMR	Solid state nuclear magnetic resonance
TEM	Transmission electron microscopy
TGA	Thermogravimetric analysis
THF	Tetrahydrofuran
TmA	Trimesic acid / benzene-1,3,5-tricarboxylic acid
XPS	X-ray photoelectron spectroscopy
ZIF	Zeolitic imidazolate frameworks

Symbols

Cu-Kα	X-ray wavelength used for PXRD and SAXS measurements
d	Interplanar distance in the crystal lattice
K_w	Ionic product
ν	Wavenumber
p	Pressure
q	Scattering vector
R_w	Residual weight
T	Temperature
T_d	Thermal decomposition temperature
T_R	Reaction temperature
t_R	Reaction time
$V\%$	volume percent
ε	Static dielectric constant
η	Viscosity
ρ	Density

1. Introduction

One of the major challenges of the 21st century is to find better materials for the growing demands of humankind. Porous polymers are widely used in our daily lives directly or indirectly, such as in water purifiers, petroleum production, battery membranes etc. Recently the field of these polymers has gained significant attention with the advent of many porous organic polymers. They have been exploited not only for their stability and strength but also because they can perform vital applications in gas adsorption[1,2], separation[3,4], catalysis[5], sensing[6–8], drug delivery and release[9], detection and removal of contaminants/pollutants[10–12], photocatalysis[13–15], optoelectronics[16,17] and in clean energy storage[18,19].

Meanwhile, people are becoming increasingly aware of the health and environmental issues. Yet, organic polymer syntheses are to date mostly revolving around organic solvents which are inflammable, expensive, toxic and environmentally harmful, also it requires energy-intensive procedures to prepare and purify. Most often these solvents are derived from petrol, which itself is a depleting resource. It is therefore an urgent need for organic and materials chemist to further develop green chemical synthetic pathways, without forfeiting the material properties. One way to develop green and innovative pathways is to take inspiration from chemical processes in nature. Water, in particular, is considered as non-toxic, non-hazardous, noninflammable and an abundant solvent used in most of the natural processes. "Hydrothermal crystallization" is a natural mineral formation process, by which highly crystalline networks such as quartz form on earth.[20] Mimicking this, similar process was implemented industrially on very large scales for artificial synthesis of quartz and other inorganic materials. By taking this further, it was possible to synthesize heterocycle-linked organic polymers in a novel and green route, using nothing but high-temperature water as reaction medium: Hydrothermal polymerization (HTP).[21] The main edge of this pathway is that, water is already cheap and most

readily available green solvent, in addition to that it is easy to recycle and it eases hectic synthetic procedure due to the hydrophobicity and apolar nature of majority of organic products.

Analogous to natural hydrothermal crystallization, several works have shown that hydrothermally generated organic compounds and materials have impressive crystallinity, which leads to improved chemical and thermal stability.[22] Hence it is possible to put the outstanding crystallinity obtained via HTP in use to further generate new crystalline linear polymers and frameworks. In the case of frameworks, crystallinity results in regular, ordered structure which leads to extended porosity. This is indeed a prerequisite for generating covalent organic frameworks (COFs).

The main target of this thesis is set on the molecular design strategy and synthesis of linear polymers and frameworks solely by HTP. Further, to explore its enhanced functionality imparted by HTP that can be put in use for high performance applications. The material properties of the designed polymers such as morphology, porosity and thermal stability were investigated.

2. Theoretical background

2.1 Classification of Porous materials

Nature has already provided many visual examples that help us to understand porous materials. For example, a honeycomb consisting of hexagonal cells appears like a "house" where honeybees can "enter, stay, and leave" this structure (Figure 2.1a). These hexagonal pores are formed by surrounding walls. The honeycomb could be regarded as the "host" and honeybee the "guest". At the microscopic level, porous materials are defined as, materials in which the atoms are not densely packed but form voids.[23] One of the first nano-porous materials discovered were natural zeolites, the well-known aluminosilicates, coined by Swedish mineralogist A.F. Cronstedt in 1756.[24] The nano-porous zeolites act as hosts that are permeable to small guest molecules. To be as informative as possible, it is crucial to provide detailed information on the size and shape of the pores. According to International Union of Pure and Applied Chemistry (IUPAC) recommendations, pores having continuous connection with the outer surface of the material are called open pores. Whereas, pores that are isolated or detached from other pores are called closed pores (Figure 2.1b).[25]
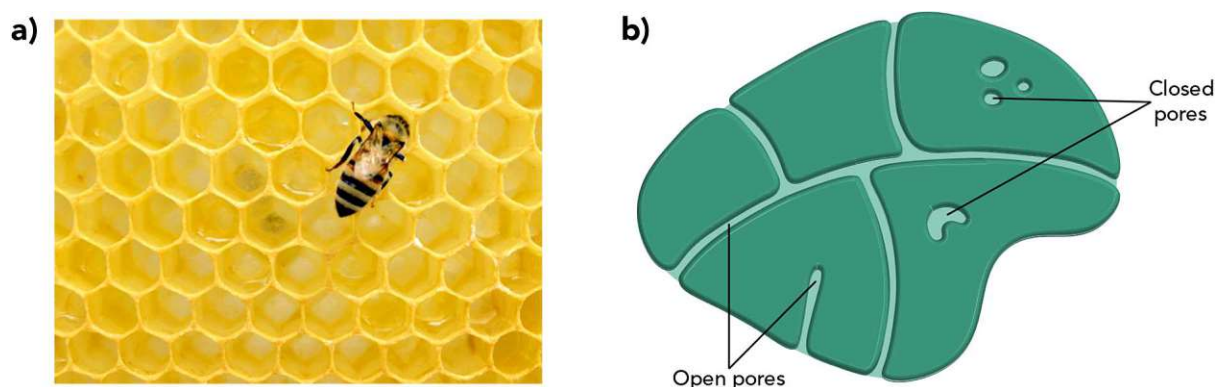
Figure 2.1: Examples of porous materials: **a)** Honey comb, a visual example of porosity in nature. **b)** Cross-section of a porous material illustrating open and closed pores.
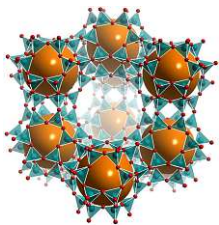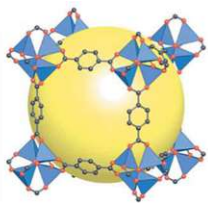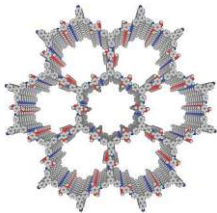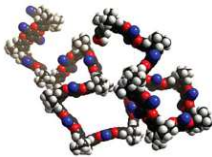
A large number of porous materials have been designed and synthesized in the past half century, they can be classified according to several important structural characteristics such as pore size, composition, pore geometry. According to the nomenclature recommended by IUPAC, porous materials can be classified as microporous materials (with pore diameters of less than 2 nm), mesoporous materials (with pore diameters of between 2 and 50 nm), and macroporous materials (with pore diameters of greater than 50 nm) based on their pore sizes.[26] Besides, based on their structural and chemical compositions porous materials include inorganic materials (natural zeolites, synthetic zeolites, porous metal oxides, etc.), carbon-based materials (graphene, carbon nanotube etc.), inorganic–organic hybrid materials (metal–organic frameworks (MOFs) and zeolitic imidazolate frameworks (ZIFs)) and porous organic polymers (POPs). On the basis of the structural order, all materials can be divided into ordered-crystalline materials, and disordered- amorphous materials.

2.2 Crystalline frameworks vs Amorphous polymers

Even though the list of porous materials is large, porous frameworks which are crystalline and having periodic and regular pores are few. Most well-known examples are synthetic zeolites, MOFs and COFs (Table 2.1). Zeolites which are purely inorganic, are prepared by hydrothermal method.[27] They are very stable and are widely used as catalysts in the petrochemical industry for chemical cracking.[28] Despite their wide usage in adsorption and separation, their pores are restrained to the subnanometer scale (< 2.0 nm), limiting their application. Along with the development of purely inorganic porous materials, remarkable innovation for synthesis of porous materials has been made with the incorporation of organic molecules as building units, forming inorganic–organic hybrid compounds like MOFs.[19] They are comprised of metal ion clusters ('nodes') connected by 'struts' made from organic molecules. It is possible to control not just the composition of metal clusters but also the pore

size by changing the struts. MOFs attract attention as future materials for adsorptive hydrogen storage because of their high specific surface areas and surface to volume ratios, as well as their chemically tunable structures.[29] But they are frequently sensitive to moisture in the air or the metal clusters are too toxic to be employed practically. Another emerging field of a new class of materials called COFs, which is a fully organic analogue of MOFs.

Table 2.1: Comparison of crystalline frameworks and amorphous POP.

	Zeolite	MOF	COF	Amorphous POP
Building unit	Inorganic	Hybrid	Organic	Organic
Connectivity	Covalent bond	Coordination bond	Covalent bond	Covalent bond
Synthesis	Hydrothermal	Solvothermal	Solvothermal	Solvothermal
Porosity	Mostly microporous	Micro/ mesoporous	Micro/ mesoporous	Micro/ mesoporous
Density	High	High	Low	Low
Crystallinity	High	High	Typically high	Amorphous
Chemical stability	Excellent	Sensitive to water/moisture	Good	Excellent
Recyclability	Troublesome, weak	Troublesome, weak	Troublesome, Good	Troublesome, Good
Designability	Poor	Excellent	Excellent	Good

One characteristic shared by all of these materials is that, under certain reaction circumstances, the polymerization reactions that create them are reversible. Meanwhile, irreversible polymerization reactions are anticipated to generate amorphous POPs. For example, Friedel–Crafts alkylation, Yamamoto coupling, Suzuki cross-coupling, Buchwald reaction etc. will tend to amorphous porous polymers with interconnected disordered pores such as hypercrosslinked polymers (HCPs)[30], conjugated microporous polymers (CMPs)[31], polymers of intrinsic microporosity (PIMs)[32] etc. Since amorphous porous polymers are prepared by irreversible reaction, most of these materials exhibit higher physicochemical stability and wide range of hierarchical pore sizes.

2.2.1 Covalent organic frameworks (COFs)

COFs are class of crystalline porous frameworks, entirely built up of light elements held together by strong covalent bonds, reported in 2005 by Yaghi and co-workers.[33] They have periodic arrangement of organic linking units, which are covalently bound and have definite pore geometry. COFs offer uniform nanometer-scale pores. The size, shape and incorporated functionality of these pores can be designed by the monomers used. This has given rise to frameworks with low densities (0.17 gcm^{-3})[34], high surface areas (4210 m^{2}g^{-1})[34], large pore sizes (up to 4.7 nm)[35].

COFs are mainly classified on the basis of linking reactions used (illustrated in Figure 2.2), most common types are *boronate linkage* based COF,[33,34] *imine linkage* based COF,[36] *β-ketoenamine linkage* based COF[37] and *triazine* based COF or CTF[38]. Other less explored linkages include *Imide linkage* based COFs[39], which are less reversible and require a reaction temperature as high as 250 °C. Additionally, COFs based on *C=C linkages* have been successfully achieved through the Knoevenagel condensation of aldehydes and benzyl cyanides in the presence of a base catalyst.[40]
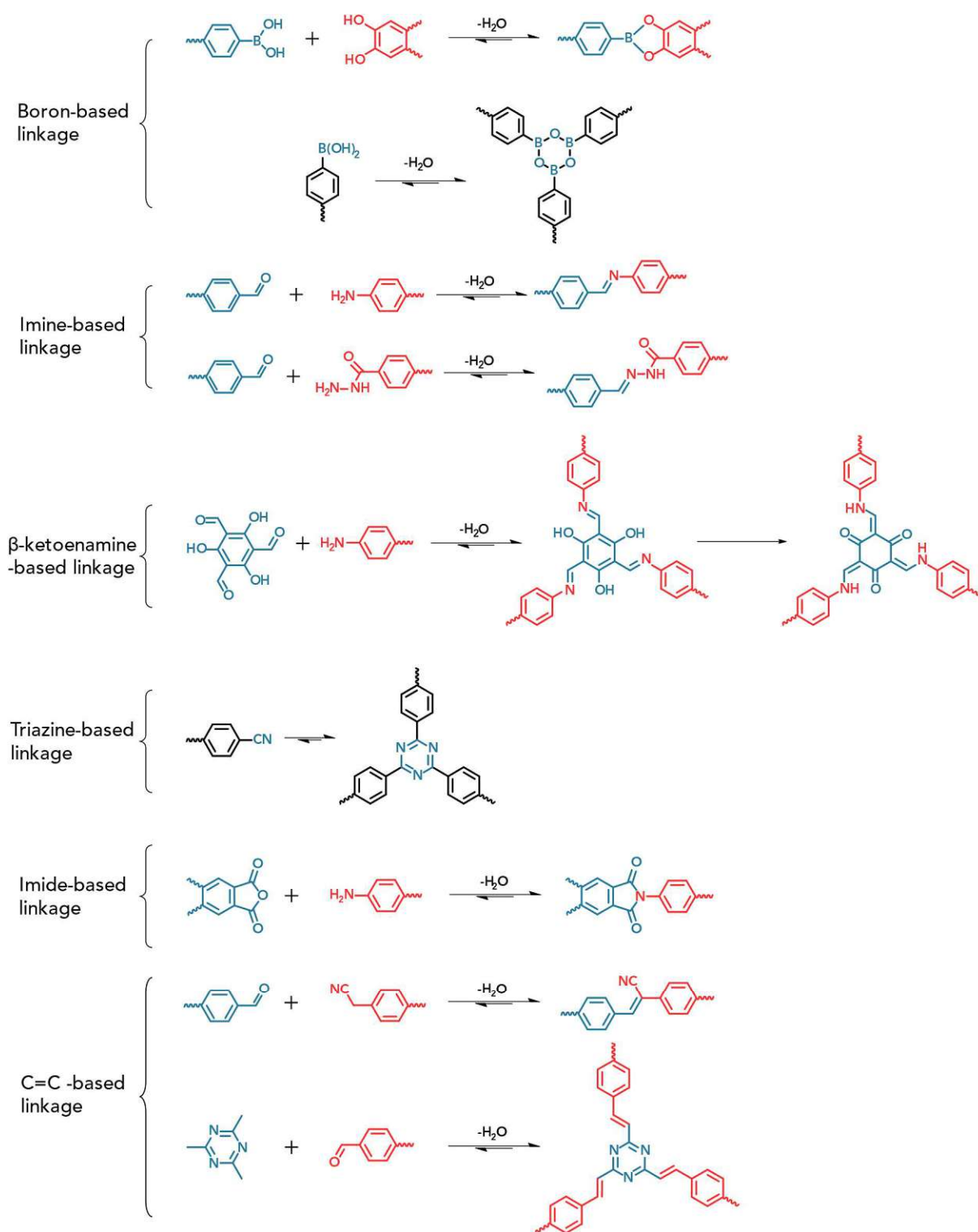
Figure 2.2: Common linkages used for generating COFs: Boronate-based linkage (boronate ester and boroxine), imine-based linkage (for example, azine and hydrazone), two-step β-ketoenamine based linkage, triazine-based linkage, imide-based linkage and C=C based linkages.

7

On the basis of dimensionality there are two and three dimensional (2D and 3D) COFs. In 2D COFs, the monomers combine to form 2D nano-sheets which assemble on top of each other with help of weak interactions (such as π–π stacking). 3D COFs are often made using tetrahedral-structured building units like adamantine[41] or tetraphenylmethane[36] linkers.

COFs have gained wide attraction due to its features such as the robust stability due to covalent bonding, great structural diversity due to the versatile combination of building units, large surface area, low density, periodic and homogenous pores, tunable pore size, insolubility etc. In 2D COFs, continuous nano-channels are formed as a result of stacking the planar sheets. Their diameter can be varied by linkers or the favoured configuration. The primary application of COF is in the field of gas adsorption and storage. It is the most studied characteristic of COFs. Their porosity, large surface area and low densities enable them to store and separate gases such as carbon dioxide, methane, ammonia and even hydrogen.[42,43] Due to the green combustion and high energy density, hydrogen is considered as the ideal power source of future. But the main problem faced is its efficient and safe storage, which is addressed by COF. COFs are also used for sensing and detection of small molecules, metal ions etc.[44]

Additionally, COFs have been effectively applied to catalytic applications. There are examples of base functionalised COFs which are used for Knoevenagel condensation reactions[41] and for Micheal addition reactions.[45] They are also used as a catalyst after loading with metal centres. Pd loaded COF-LZU1, synthesized by Wang and co-workers showed very good catalytic activity in the Suzuki-Miyaura coupling reaction.[46] Water splitting reactions are also carried out with help of COF. Lotsch and co-workers synthesised hydrazone-based COFs doped with Pt which can act as hydrogen evolution catalyst from water in presence of visible light.[47] Banerjee and co-workers made COF modified with Co ions as a water oxidation electrocatalyst.[48] Carbon dioxide reduction has also been carried out using cobalt porphyrin-based COF in aqueous medium.[49]

In the field of energy storage and opto-electronics also COF is a viable option. Incorporating electron donors and acceptors moieties as linkers for making COFs make them suitable for organic opto-electronic devices. This donor-acceptor interface and aligned π arrays help them achieve light adsorption, electron transfer and charge separation thus they can be used for photo-induced electron transfer.[50] COFs prepared from aromatic building units and luminescent π systems like pyrene, porphyrine, perylene etc. show possible application in these fields. For light emitting applications also emmisive COFs are being developed.[51] Their π–π stacked layered structure makes them suitable for these applications. Recently, a boronate ester linked naphthalene diimide based 2D COF showed interesting application as cathode material in Li-ion batteries.[52] A new porphyrin based 2D COF was used as host materials for sulphur impregnation in Li-S batteries and thus able to improve its performance and stability.[53]

2.2.2 Design principles

COFs are a class of fully predesignable polymer that is achieved by topology-directed polymer growth along with geometry matching between monomers (Figure 2.3). In principle the synthesis of COF is based on reticular chemistry. Reticular chemistry is the study of linking discrete chemical entities through strong bonds to get predictable extended frameworks and large discrete molecular structures.[54] Before making a framework, we break it apart and start from simple materials and connect it in a logical fashion. To ensure a clear direction of each covalent bond, the monomers are required to have relatively rigid backbones with a specific geometry that reflects the relative positions of reactive sites. The covalent bonds guide the spatial orientation and determine the relative positions of the next monomer units; repeating this rule in each reactive site restricts the chain growth directions in a manner that strictly follows the predesigned topology diagram. The geometry and dimensions of the organic building blocks and linkages determine the size and topological structures of pores in the

resulting COFs. For instance, a combination of C_3- symmetrical (trigonal) monomer and C_2-symmetrical (linear) monomer will create a COF with hexagonal pores. This kind of structural designability is difficult to achieve using other POPs.
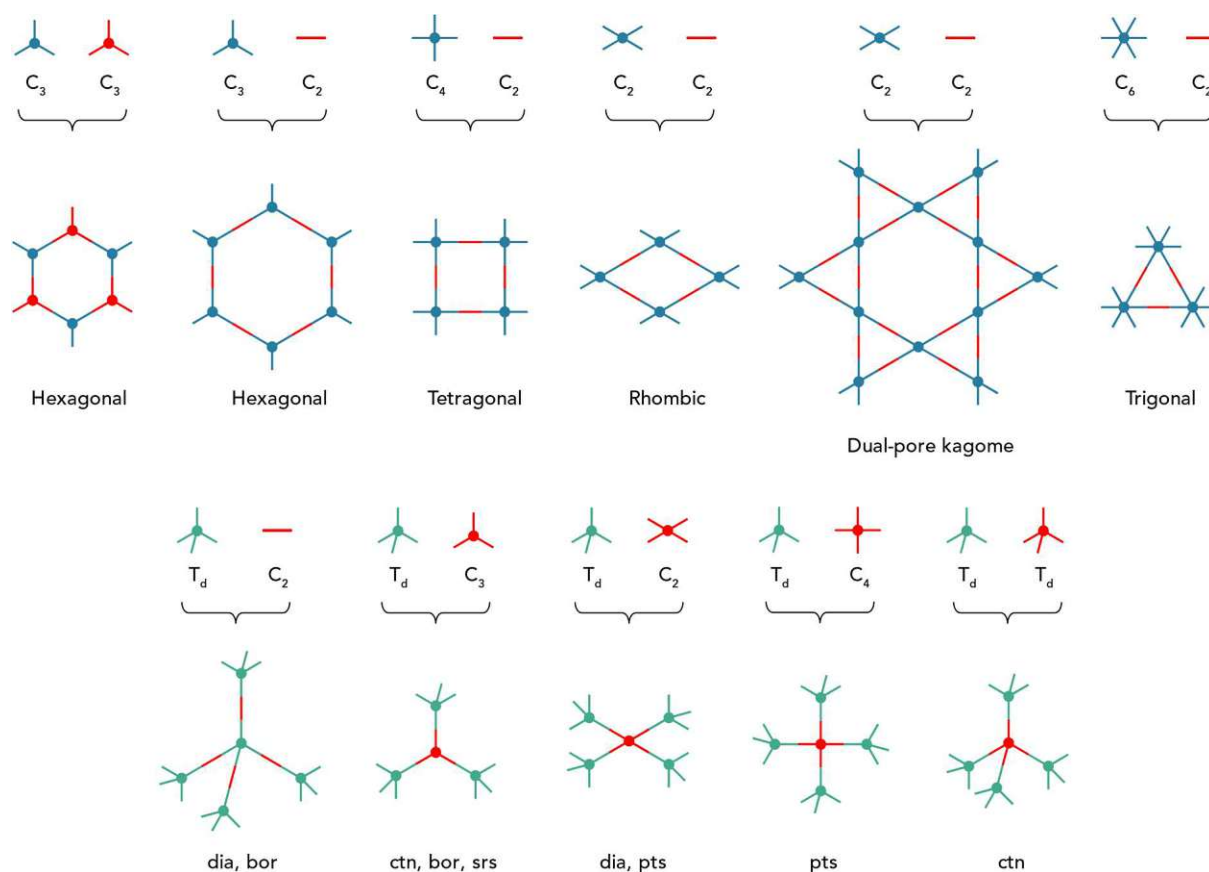
Figure 2.3: Basic topological diagrams for the design of 2D and 3D COFs.

COFs are generally prepared by connecting monomers through reversible linkages to ensure its structural regularity and porosity. Dynamic covalent chemistry (DCC) and reversibility of the linking functions contribute to the self-reconstruction of the oligomers, till a stable framework is formed. When the monomers react with each other, amorphous networks (the kinetic product) form first. The reaction conditions allow the amorphous network to break into smaller fragments followed by reconnecting them as many times as needed until a long-range order is achieved. This act as an agent of error checking and proof-reading during synthesis and ensures a crystalline framework (the thermodynamic product) structure is formed (Figure

2.4). This also means that conditions that render the linkages reversible have to be found for each COF. Previous studies have proved that the introduction of heteroatoms such as oxygen, nitrogen, and boron improve crystallinity to the framework.
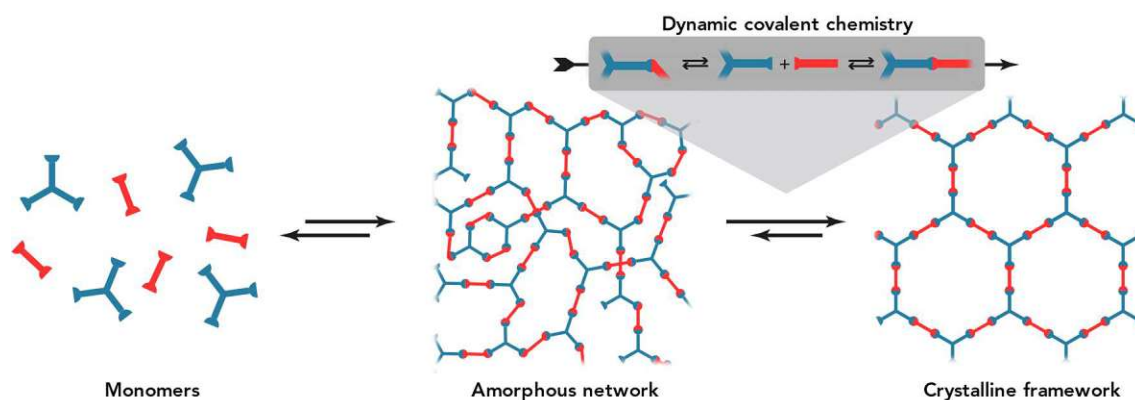
Figure 2.4: Dynamic covalent chemistry and reversibility of the linking functions are involved in yielding crystalline, thermodynamic product, even if amorphous, kinetic product is formed first.

2.2.3 Amorphous polymers

The chemical synthetic strategy behind the construction of complex architectures of POPs is to incorporate desired components as building units to achieve targeted applications. The choice of monomers, mode of synthesis and reaction parameters, such as temperature, pressure, solvent etc. play a crucial role in 'stitching up' molecular building units in a particular fashion in order to form the macrostructure. Occasionally crystallinity is not a much-needed attribute while making these polymers. Hence a plethora of reactions ranging from cross-coupling to cyclo-condensations can be carried out to synthesize porous networks with targeted structures and properties, which in turn can be profited with better acid/base stability of the material. The extensively cross-linked hyper crosslinked polymers or HCPs were one of the first kinds of pure microporous organic materials described in the early 1970s, mainly synthesized by Friedel–Crafts alkylation, Ullmann and Buchwald coupling reaction according to the

monomers used.[55] The basic principle behind HCP synthesis involves preparation of a polymer precursor, which is then further cross-linked. This copolymer is then swollen in a suitable solvent and subjected to Lewis-acid-aided Friedel–Crafts alkylation for hypercrosslinking of polymers, resulting in a rigid, extended and highly solvated 3D-network.

Conjugated microporous polymers (CMPs) were first reported in 2007 Cooper and coworkers.[56] These are microporous, amorphous, 3D-network polymers with decent surface areas and extended π-conjugation between aromatic subunits giving rise to conductive properties. Primarily, metal-catalyzed C-C coupling reactions, such as Sonogashira–Hagihara, Suzuki, and Yamamoto coupling reactions, have been employed. Even though they are not completely crystalline, they offer some degree of molecular preorganization with help of specific cross-coupling reactions and templated pathways. CMPs are exceptionally synthetically diverse with wide range of monomers available, this also enables the control of the surface areas, pore sizes and functionality.

Polymers with intrinsic microporosity (PIMs) were developed for the first time by McKeown and coworkers in the early 2000s.[57] The general design strategy of PIMs involves incorporation of rigid aromatic monomers that are having a bent or also known as the "site of contortion", linked by non-reversible condensation reactions to form a polymer. These polymers cannot efficiently fill the space and pack together due to the site of contortion, and thus force the backbone of the polymer to twist or turn, which results in intrinsic microporosity. Unlike conventional microporous materials, they can be processed readily using solvent-based techniques and many are soluble in polar aprotic solvents (e.g. THF, DMAc).

Other than these porous polymers there are many organic polymers used especially for high-performance application such as in batteries,[58] electronics,[59] engine components,[60] aircraft and aerospace vehicles,[61] because of their thermal stability, chemical resistance and mechanical performance. The properties of such high-performance polymers (HPPs) are in turn a direct

consequence of the molecular structure. HPPs, which feature materials of top performance e.g. aromatic polyimides, polyquinoxalines, polybenzothiazoles, polybenzimidazoles and polybenzoxazoles have been synthesized and widely studied in the past three decades.[62]

A subclass of HPPs featuring utmost chain-stiffness are so-called conjugated ladder polymers. They have polymer backbone units exclusively composed of π-conjugated fused rings (Figure 2.5a). They have attracted great interest owing to their superior properties, remarkable chemical and thermal stability, and potential suitability as functional organic materials.[63]
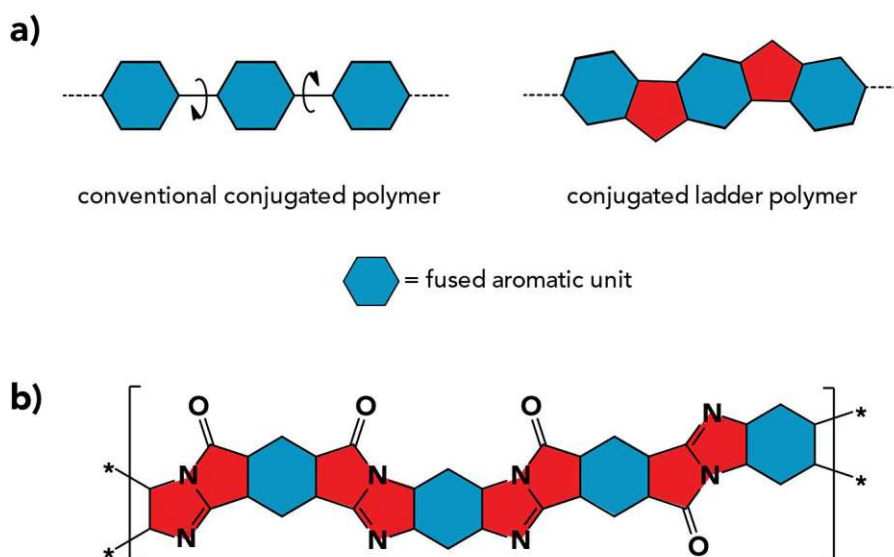
Figure 2.5: a) Graphical representation of conventional conjugated polymer and conjugated ladder polymer. **b)** Schematic of a Polypyrrolone (PPy), an example of conjugated ladder polymer.

Polybenzimidazopyrrolones or simply, Polypyrrolones (PPys) are such type of conjugated ladder polymers with rigid backbones and fused heterocyclic linkages (Figure 2.5b). They were first synthesized in 1965, by two-step procedure including the polycondensation of aromatic dianhydrides and tetraamines followed by thermal cyclization.[64,65] PPys are presumed to be stiffer and have greater tensile strength than those of similar polyimides.[66] The greater rigidity

and thermal stability of the PPys lead to high glass transition temperatures, therefore extending their temperature range of application.[67] Furthermore, PPys have been reported to depict greater chemical stability in acidic and basic conditions, tolerance to ionizing radiation allows for application in gas-permeable membrane, electron-transporting materials and conductive polymers.[68–70]

2.3 Green Chemistry

Another important aspect in addition to the aforementioned materials design, lies in the choice of reaction media. Traditionally, chemical processes primarily utilize organic solvents, resulting in the generation of a significant amount of organic waste in the chemical industries. To make meaningful comparisons among the different routes to obtain products via organic synthesis, metrics are needed to measure the environmental friendliness of the procedures. Ever since the introduction of the twelve principles of Green chemistry by Anastas and Warner in 1998,[71] a wide range of metrics to classify organic reactions and processes have emerged (e.g. E factor, atom economy, etc.). The most common green chemistry metric is the environmental factor (E factor), which was introduced by R. Sheldon to quantify the amount of waste produced in a chemical process.[72] The E factor is based on mass and is calculated by-

$$E\ factor = \frac{Total\ mass\ of\ waste\ from\ process}{Total\ mass\ of\ product}$$

Table 2.2 provides an overview of the annual waste production from major industries worldwide. In response, the use of so-called "green chemicals" has recently been implemented in chemical manufacturing and pharmaceuticals to eliminate organic waste as well as to avoid hazardous and toxic reagents or solvents through energy-efficient and highly atom-efficient procedures.

Water can be considered a cleaner and more sustainable solvent compared to organic solvents, meeting the criteria for being "green." The advantages of using water as a reaction medium in chemical processes include low costs, high availability, safety, non-volatility, non-toxicity, and non-carcinogenicity.

Table 2.2: Typical annual production sums and E factors in the chemical industry.[72]

Industry segment	Product tonnage	E-factor
Oil refining	$10^6 - 10^8$	< 0.1
Bulk chemicals	$10^4 - 10^6$	$< 1 - 5$
Fine chemicals	$10^2 - 10^4$	$5 - 50$
Pharmaceuticals	$10 - 10^3$	$25 - 100$

2.4 Hydrothermal synthesis

Deep inside earth's crust crystalline minerals such as natural quartz form via process of "hydrothermal crystallization". The water from groundwater reservoirs such as hydrothermal veins which are in close proximity to a hot area such as a magma chamber, gets heated up. At this high temperature (T) typically 100–500 °C and pressure (p) from 1 bar-10 kbar, ions and atoms from delimiting rocks dissolve in the water. Once the temperature drops, the dissolved species can recrystallize into large crystals, if the cooling rate is low enough.[73] This is possible because the physicochemical properties of water at increased temperatures are significantly different from that of ambient temperature. The H-bonding network of H_2O breaks down with increase in temperature, that is, the average number of H-bonds per molecule of H_2O is 3.9 at room temperature (tetrahedral H-bonded network), it reduces to 2.4 at 300 °C (loosely/non-connected H_2O clusters) (Figure 2.6a-b).[74] Several physical characteristics of High-temperature water (HTW) differ greatly from ambient water due to this decrease in H-bonding

of H_2O. Most important of them are the density ρ, the viscosity η, the static dielectric constant ε and the ionic product K_w.[75–77] The variation of ρ, η, ε and K_w as a function of T for both H_2O (l) (blue curve) and H_2O (g) (orange curve) at saturation pressure are plotted in Figure 2.6c-f.
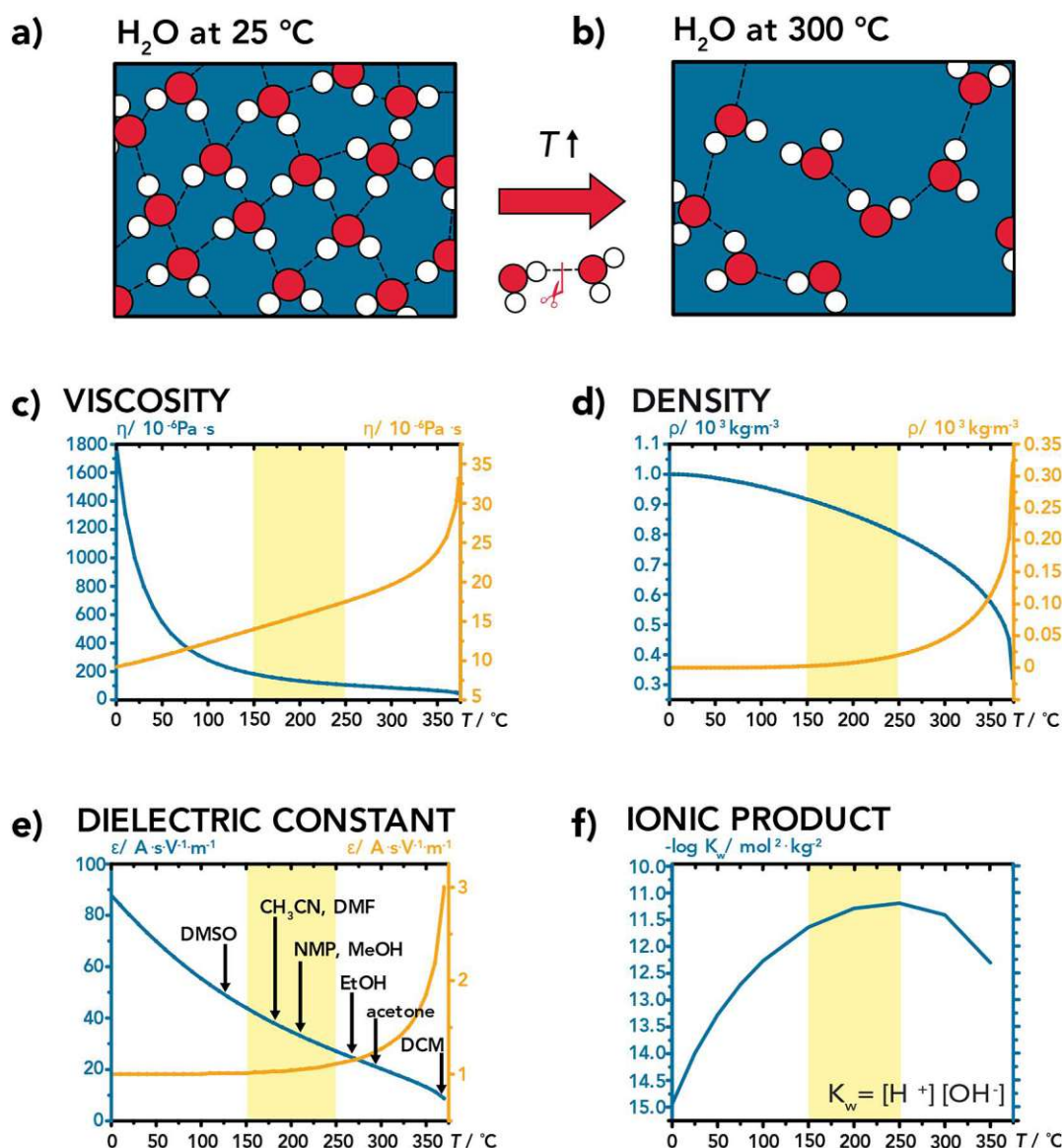
Figure 2.6: Physicochemical properties of water at elevated temperatures. (**a, b**) Schematic of the H-bonding situation in H_2O at room temperature (**a**) and at 300 °C (**b**). (**c- f**) Evolution of physicochemical properties with T for both saturated $H_2O_{(l)}$ (blue) and $H_2O_{(g)}$ (orange): density ρ (**c**); viscosity η (**d**); static dielectric constant ε (**e**) with ε of other common organic solvents (DMSO- Dimethyl sulfoxide, CH_3CN- Acetonitrile, DMF- Dimethyl formamide, NMP- N-methyl pyrrolidone, MeOH- Methanol, EtOH- Ethanol, Acetone, DCM- Dichloromethane) for comparison; and ionic product K_w (**f**). The T-range (150–250 °C), where the majority of artificial hydrothermal syntheses are carried out, is highlighted by the yellow box.

i. Both ρ and η rapidly decrease with T for $H_2O_{(l)}$, which has significant impact on transport properties: as ρ and η decrease, the diffusivity in H_2O increases.[77] This helps in dispersing the reactants in the medium and thus affects diffusion-controlled chemical reactions.

ii. The static dielectric constant, ε, which indicates the polarity of a solvent, also decreases with T. This means that, water- a polar protic solvent, is comparable to polar aprotic solvents such as N-methyl pyrrolidone (NMP), acetonitrile (CH_3CN) or dimethylformamide (DMF) at this elevated T, p regime. Which makes it possible for HTW to dissolve and recrystallize certain mineral species.[78]

iii. The ionic product of water, K_w, increases with T, and has its maximum at 250 °C. Since K_w of H_2O is the product of $[OH^-]$ and $[H^+]$, its increase reflects the increasingly dissociated nature of H_2O with T.[77] Hence the reaction medium water itself can act as an acidic, basic or even powerful acid/base bi-catalyst. This increased K_w is clearly beneficial for driving many mineral formation reactions forward.

Since these changes in the physiochemistry of water strongly impact the solubility of solutes and driving the chemical reactions, this make HTW a highly interesting reaction medium.

The term 'hydrothermal synthesis' is commonly used for reactions carried out in water as a reaction medium above its atmospheric boiling point (100 °C) and under autogenous pressure.[79] The "typical" temperatures at which artificial hydrothermal synthesis are carried out is around 150–250 °C (below the critical point, CP= 374 °C). The elevated T- and p- conditions are generally obtained by heating a certain amount of water in a closed steel reactor, so-called autoclave (Figure 2.7a) under isochoric conditions. Under ideal conditions, when the autoclave with water (eg: 30 $V\%$ $H_2O_{(l)}$) is heated to $T > 100$ °C, it retains a mixture of high-temperature liquid and vapour (Figure 2.7a). Since the autoclave is a closed system, autogenous pressure builds up, thus the system operates at the liquid-vapour coexistence line of water (Figure 2.7b). The most common set-ups to generate hydrothermal conditions artificially are

the already mentioned autoclaves, and sealed thick-walled glass tubes.[80] Employing steel vessels allows for various adaptions of the set-up, including the use of, e.g., gas inlets, stirrers, or diaphragms for the generation of different concentration zones.[81] In contrast, the use of glass tubes is cheaper but also less sophisticated. Large-scale hydrothermal crystallizations additionally employ designed cooling protocols, and can be engineered to profit from temperature gradients, as well as the use of seed crystals.[80]
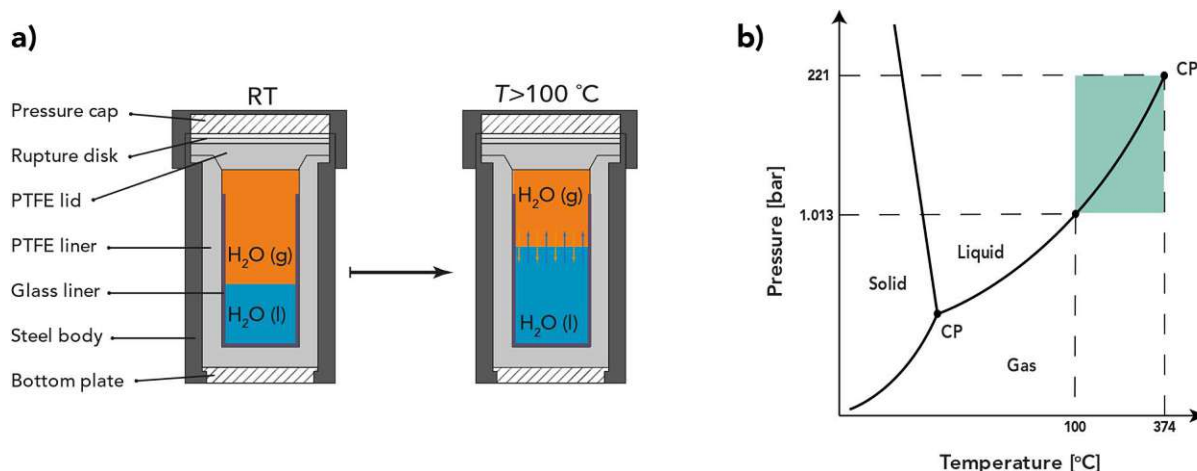
Figure 2.7: a) Schematic of a non-stirred autoclave used to generate HT conditions. HTW is generated by heating H_2O from RT to $T > 100$ °C in an autoclave **b)** Phase diagram of H_2O showing the HT region (green background) situated at $T > 100$ °C and $p > 1$ bar, but below the supercritical region (critical point, CP = 374 °C, 221 bar).

Inorganic ionic compounds are inherently easy to crystallize. So, it's possible to mimic this process and generate crystalline inorganic materials at laboratory via hydrothermal syntheses. The possible material classes that are most synthesized hydrothermally include synthetic analogues of naturally formed materials like zeolites[82], gemstones such as quartz[83] and sapphire[84], and a variety of inorganic salts such as oxides, fluorides, carbonates, sulfides or sulfates.[81] The advantages of employing artificial hydrothermal crystallization include:

i.   the precursors are mostly soluble in HTW, even if they are insoluble in ambient H_2O

ii.   the acid/base catalysis drives the formation of the desired products in HTW.

iii. highly crystalline products can be obtained.

Moreover, as a result of the increased apolarity of HTW, enhanced diffusion in HTW and possibility of HTW to act as a powerful acid/base bi-catalyst, it can also be used for the synthesis of organic compounds. This gives a great advantage since most of the organic materials are inherently hard to crystalize.

2.4.1 Hydrothermal synthesis of organic materials

At first glimpse, water seems like a counter-intuitive medium for the synthesis and crystallization of organic materials. However, several examples have shown that under hydrothermal conditions, water can be an excellent medium for synthesizing and crystallizing organic materials ranging from small molecules, through linear polymers, to 3D frameworks. One of the first organic polymer made hydrothermally was polyimides, synthesized by Chiefari and coworkers in 2003.[85–87] Polyimides (PIs) are generated by polycondensation of diamines and dianhydrides. Hence, they are condensation polymers, i.e., they are obtained by the elimination of a low-molecular weight byproduct (here H_2O) upon each monomer addition step. All hydrothermal syntheses of PIs reported until 2014 lead to amorphous PIs. In 2014, Unterlass and coworkers reported the first highly crystalline PI, poly(*p*-phenylene pyromellitimide) (PPPI) synthesized by Hydrothermal polymerization (HTP) under carefully chosen reaction conditions.[21] Due to the outstanding crystallinity obtained via HTP, PPPI's crystal structure could be obtained from powder X-ray diffraction, which is extraordinary for an organic, polymeric material. Further crystalline PIs, such as poly(*p*-phenylene benzophenone imide) and poly(4,4-biphenyl benzophenone imide), were similarly made.[88,89] All three of these polyimides were obtained as fine powders, composed of microparticles of flower-shaped morphology, which is further indicative of high crystallinity. Later in a follow-

up work, Unterlass and coworkers reported that polybenzimidazoles and pyrrolone polymers can also be generated by similar HTP method.[90]

Rosseinsky and coworkers reported the hydrothermal synthesis of crystalline polyamides, another class of condensation polymer.[91] Interesting fact is that, with this contribution they have extended hydrothermal crystallization from linear organic polymers to frameworks, namely to 2D and 3D amide-linked COFs (CAFs). Hydrothermal synthesis of small molecules, imides such as perylene and naphthalene bisimides, are also reported using similar reaction conditions.[92] This was further extended to Perinone, i.e., naphthalene tetracarboxylic acid bisbenzimidazole, a carbonyl dye. It is a double condensation product of naphthalene bisanhydride and o-phenylene diamine which was synthesized solely in HTW.[93]

The main synthetic approaches to yield organic products via HTP include:

i.   Monomer salt synthesis: When the comonomers dianhydride and diamine are brought into contact in water at an elevated T, the dianhydride first hydrolyzes to the corresponding tetracarboxylic acid and then reacts via acid/base reaction with the diamine to form an intermediate monomer salt. This was subsequently subjected to hydrothermal synthesis. Monomer salt imparts the 'ideal' stoichiometry needed for the reaction.[88–90]

ii.   Direct synthesis: A stoichiometric physical mixture of the comonomers was homogenized through grinding or sonication and then subjected to the hydrothermal synthesis conditions.[91]

iii.   Devitrification: First, an amorphous organic network was prepared through conventional polycondensation reaction solvothermally (in DMF, NMP, DMAc etc). The isolated amorphous networks were then hydrothermally treated in sealed ampoules to yield crystalline frameworks.[91]

3. Aim of the work

The initial objective of this thesis was to develop stable porous crystalline COFs via greener hydrothermal synthesis. Different molecular design principles for water-compatible frameworks as well as the development of reaction strategies for HT reactions have been pursued. The main objectives were planned, starting from the new preparation methods to the structural and morphological impact study of the materials. Our strategy was to use strong functional linkages like amide and imidazole, which are not much explored in COF literatures to achieve such crystalline polymers.

During the process of COF formation there can be a variety of intermediate structures that can form (Figure 3.1).[94] For example, when combining C_3 and C_2 geometric monomers, it can form small hexagonal oligomers/ macrocycles. Which further combine to form structures composed of several fused macrocycles. Now this can repeat on and become an extended sheet and meanwhile it can also act as a template, so that other oligomers can stack on it via Vander-Waals interactions and eventually end up as a COF. However, such a fully extended COF was not achieved during the reaction. Instead, intermediate fused macrocycle structures were successfully generated, which were equally interesting.

Monomers   Macrocycle   Fused macrocycles   COF
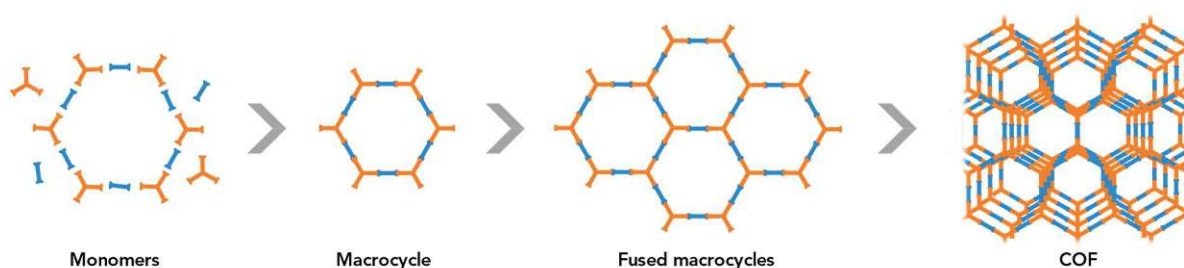
Figure 3.1: Illustration of various possible intermediate structures during framework formation.

Along with the objective of exploring various linking chemistries, it was found that imidazopyrrolone linked materials can be generated via the HT route. Therefore, another objective was to generate imidazopyrrolone linked conjugated ladder polymers. These are known to be very robust materials. The linkage is stable and hardly reversible, in addition to that random cis/trans positioning of the linkage makes the material hard to crystallize. The synthetic procedure of this material was modified from the previously reported methods by introducing the utilization of microwave (MW). This resulted in rapid and less tedious synthesis process.

Summing up, the general feasibility of synthesizing organic materials with various linkages generated via the HT route was aimed to be established.

4. Results and discussion

This chapter is divided in three main sections, which are based on three projects about

1. Hydrothermal synthesis of crystalline amide-linked organic materials

2. Hydrothermal synthesis of crystalline benzimidazole-linked organic materials.

3. Hydrothermal synthesis of polybenzimidazoles and their conversion into polypyrrolones

The main purpose of this chapter is to demonstrate the synthesis and characterization of the organic materials generated via HTP.

4.1 Hydrothermal synthesis of crystalline aromatic amide-linked organic materials

4.1.1 Introduction

For generating COFs, the most exploited linking chemistries are boronic ester/ boroxine and imine linkages. While these linkages are easily reversible and thus allow for error-correction via DCC. Unfortunately, they also disintegrate relatively easily under hydrolytic strain.[37,95] Therefore, recent efforts focus on generating COFs linked by strong functions like imide[96], triazine[38], pyrazine[97], β-ketoenamine[37,98] and amide[99,100]. Till now, there are only a few prior reports of amide-linked COFs. Amide functions, which are proven to be stable and strong,[101] are found as peptide linkages in proteins. It is also used in industrially well-known organic polymers such as Nylon 66. Combined with aromatic building units, results in one of the toughest of all polymers, the aramid Kevlar[TM]. Through H-bonding and π- π stacking, Kevlar is in fact crystalline.[102] Clearly, generating an aramide COF would potentially allow for

combining the outstanding mechanical and chemical properties of Kevlar with ordered porosity.

To date, amide linked COFs have been generated by: (i) Linkage conversion,[99,100] in which an imine linked COF is made and subsequently oxidised to amide. Surprisingly, this retains the crystallinity and porosity of the initial COF. (ii) Devitrification route by Rosseinsky and coworkers.[91] The monomers were precondensed in DMF to obtain an amorphous polyamide network, which was subsequently 'devitrified' using HT treatment. This process resulted in the generation of a crystalline COF by rendering the amide linkage reversible. It is reported to be very stable in acid and basic conditions, despite the fact that their framework is not fully aromatic. Apart from this two-step approach, a direct "green" route for synthesizing crystalline organic low-molecular weight compounds as well as high-performance polymers like polyimides has been reported, using nothing but high-temperature water as reaction medium: hydrothermal polymerization.[88,89] Most interestingly, HT synthesis generates fully crystalline materials, therefore it significantly enhances several material properties such as thermal, mechanical, and chemical stabilities.[22]

In this attempt, an extended porous crystalline amide-linked framework was sought to be created using HT synthesis. However, the achievement of such fully extended frameworks was not possible. Instead, crystalline polyamide macrocycle structures were generated, which held equal interest.

4.1.2 Synthesis and characterizations

In this study, for generating the crystalline aromatic polyamide material (PAM), the monomers benzene-1,3,5-tricarboxylic acid/ trimesic acid (TmA) and benzidine (Bz) were combined in water. It was then employed under HT conditions, which enabled the polycondensation reaction to produce the crystalline polyamide material (Scheme 4.1).
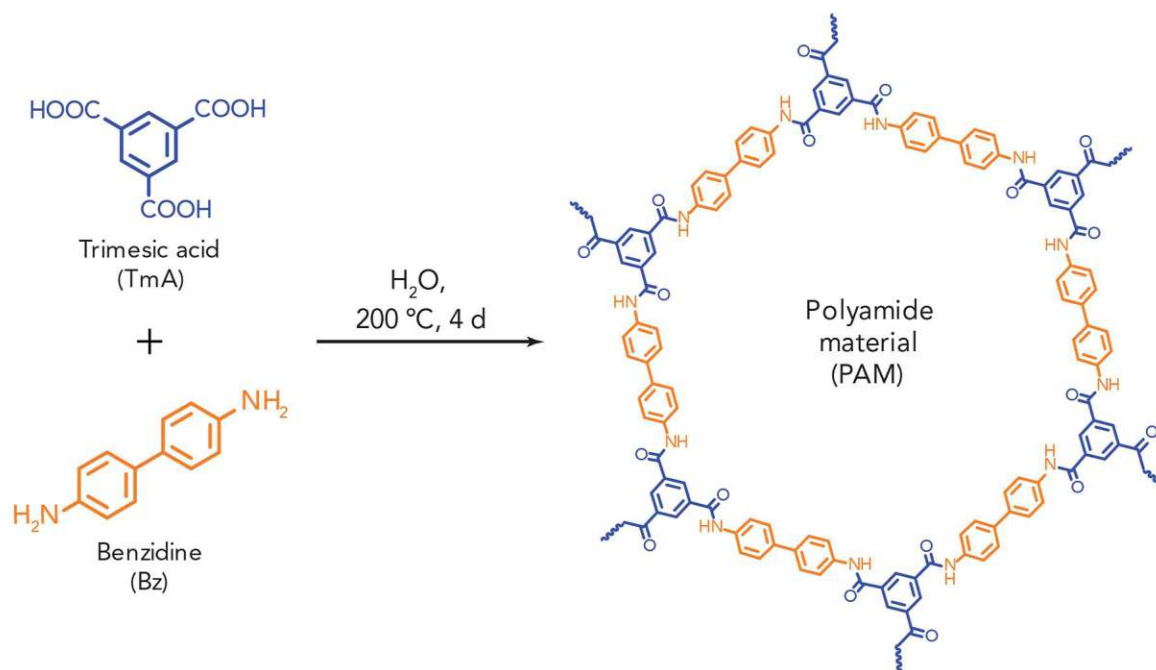
Scheme 4.1: Synthesis of PAM from TmA and Bz

All syntheses were carried out by suspending TmA and Bz at stochiometric ratios of 1:1.5 in distilled water, followed by sonication at room temperature. Even though HTW can act as a bi-catalyst, a distinct batch was prepared in which acetic acid (HOAc) was introduced as a modulator: PAM-HOAc. It has been reported to facilitate the reversibility of linking function, which is crucial for the crystallization process. The reaction mixture was then sealed in a steel autoclave and heated to reaction temperature (T_R) of 200 °C under autogenous pressure. The reaction was screened at various reaction time (t_R) from 1 day to 6 days and the optimum t_R to yield the crystalline product was found to be 4 days after screening.

After cooling down the autoclave, the solid was isolated via filtration and then washed repeatedly with water, ethanol and acetone until the washing solution appeared clear. The solid was dried at 80 °C under vacuum. The obtained product was found insoluble in common solvents like water, acetone, methanol and ethanol.

The progress of the reaction was monitored with FT-IR spectroscopy (refer section 5.1.2). The complete conversion to product was confirmed by the absence of FT-IR modes of TmA

and Bz, as well as by the presence of new bands caused by amide-linkage. In the FT-IR spectra (Figure 4.1), the strong NH_2 doublet band located at ~3350 cm^{-1} was absent and new C=O (amide) stretching modes at ~1630 cm^{-1} of the network were visible. But even after prolonged reaction times (t_R= 6 days), there were still C=O (acid) stretching bands at ~1700 cm^{-1} in the FT-IR spectra, confirming the presence of peripheral -COOH groups in both batches. Moreover, broad modes in the H-bonding region (~3100 cm^{-1} - 2700 cm^{-1}) further point at -COOH endgroups. It is evident from the FT-IR spectra that presence of modulator has not altered the chemical conversion, as spectra of both batches were almost identical.
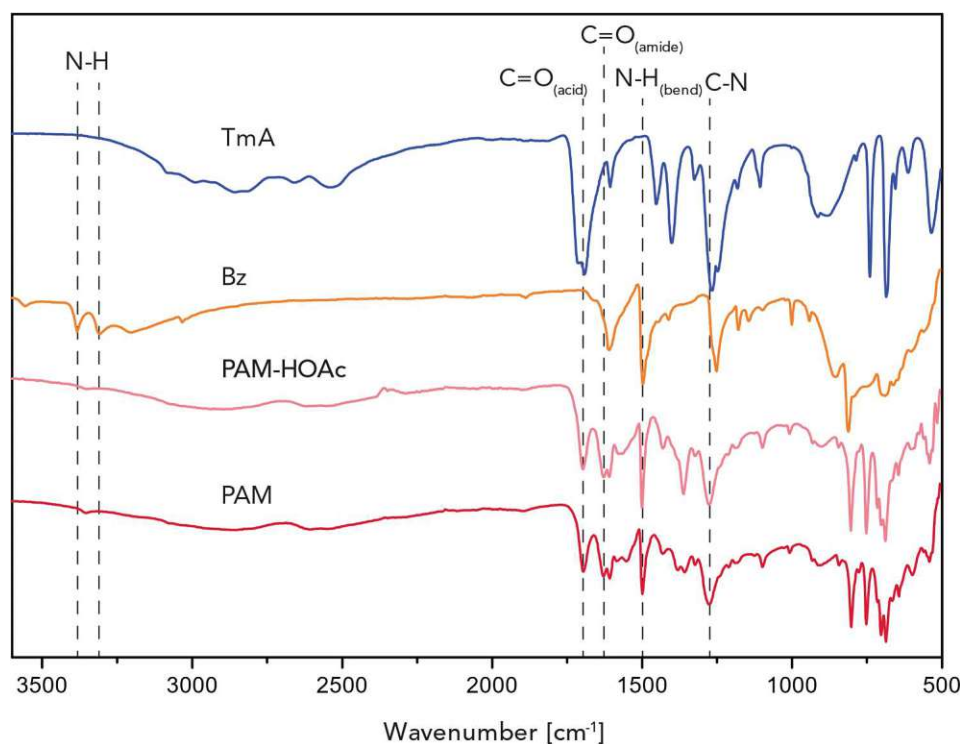
Figure 4.1: FT-IR spectra of TmA, Bz, PAM-HOAc and PAM

^{13}C cross-polarization magic-angle-spinning (CP-MAS) solid state NMR was collected for further characterization of the PAMs. The spectra obtained for the synthesized PAMs (AC, T_R= 200 °C, t_R= 4d) were compared with those of the conventionally synthesized similar polyamide from literature.[103] Both PAMs display a signal at 170 ppm which corresponds to the amide

carbonyl. The signals between 122 and 138 ppm correspond to the aromatic carbons of phenyl moieties of both the PAMs (Figure 4.2).
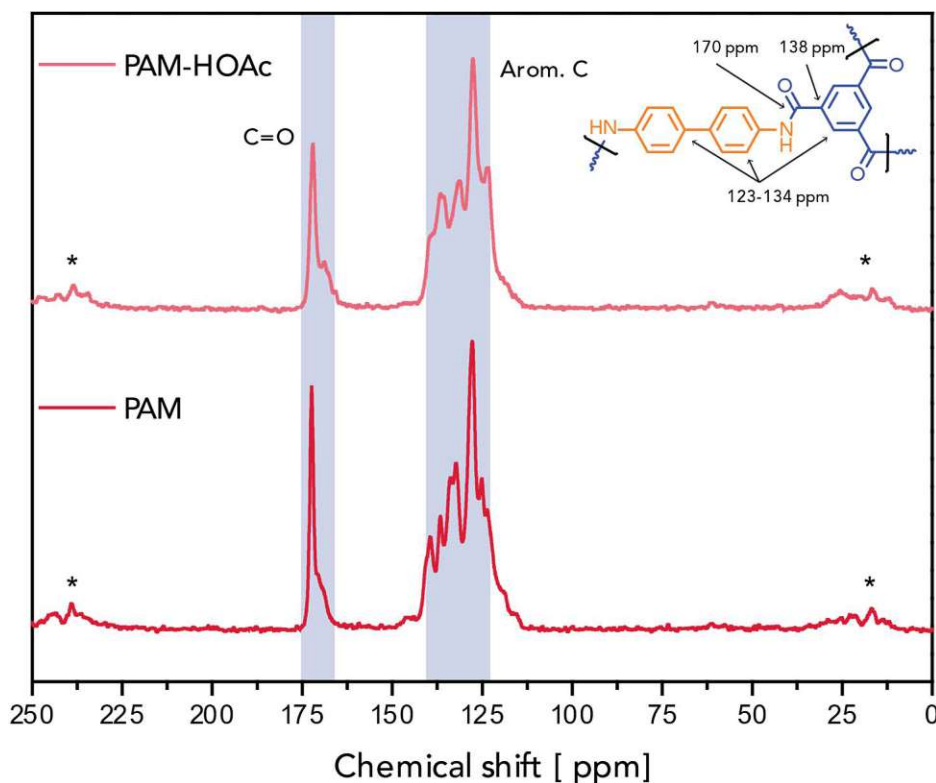
Figure 4.2: ^{13}C CP-MAS solid state NMR spectra of PAM-HOAc and PAM. * indicates peaks arising from spinning side bands.

The experimental powder X-ray diffraction (PXRD) pattern of the obtained solids (AC, $T_R=$ 200 °C, $t_R=$ 4d) showed a high degree of crystallinity and long-range order resulting from the HT synthesis (Figure 4.3). Moreover, the observed Bragg peaks of the products were found to be different from the ones of the respective monomers. It also became evident that the addition of acetic acid as a modulator did not play a major role to promote the formation of an extended framework. From the spacing of the peaks, it was found that the product has hexagonal lattice arrangement, same as that of the expected COF structure. An attempt was made to align the PXRD pattern with simulated patterns from various optimized framework structures, yet none of them yielded a precise match (refer section 5.1.4).
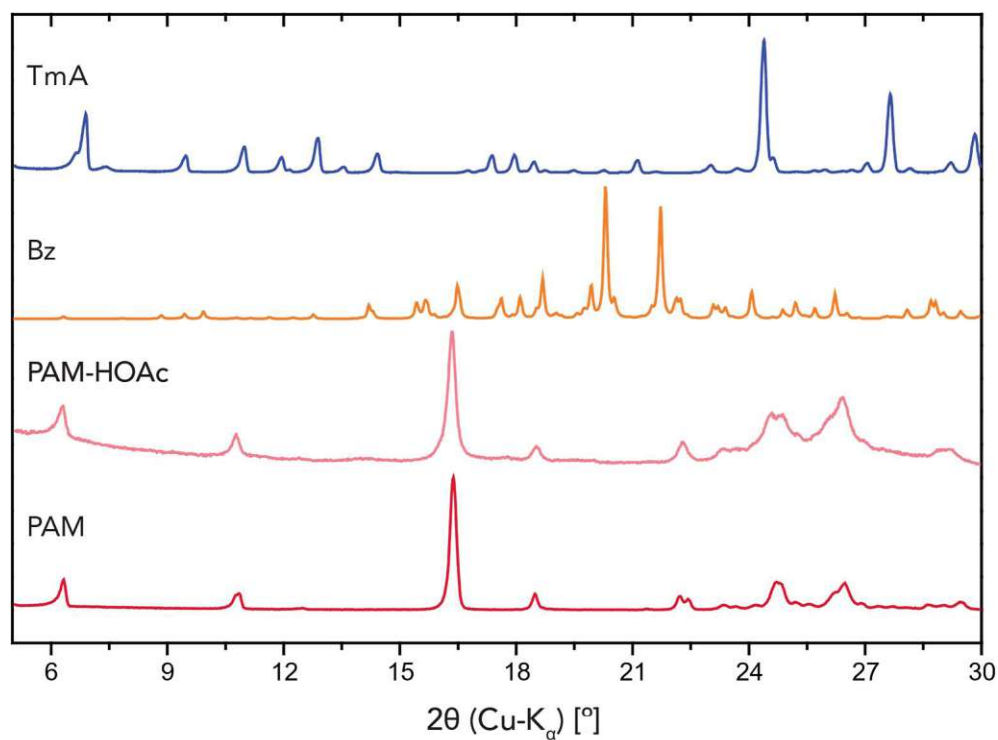
Figure 4.3: PXRD patterns of TmA, Bz, PAM-HOAc and PAM

Thermal gravimetric analysis (TGA) measurements showed that the polyamide material feature significant thermal structural stability (Figure 4.4). Both batches showed similar TGA curves.
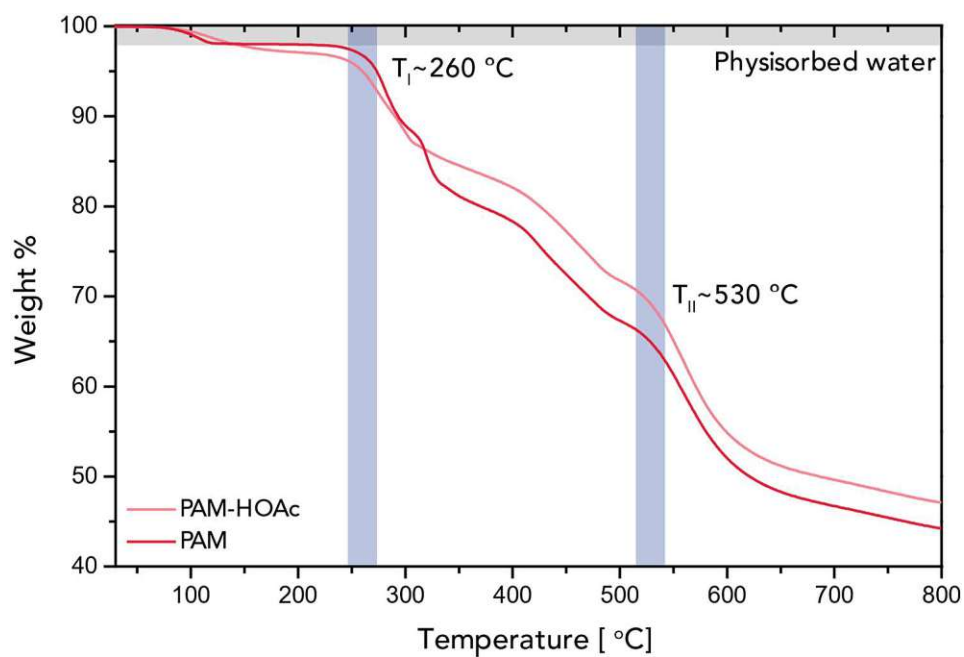
Figure 4.4: TGA thermograms of PAM made with HOAc and without HOAc

28

Both batches showed an initial weight loss around ~100 °C, which can be attributed to the removal of moisture and trapped gas. A second weight loss was seen around ~260 °C, which could be due to the decarboxylation of peripheral -COOH groups. This was followed by a multistage decomposition with a major weight loss around ~530 °C. This corresponds to total decomposition of the polyamide product, since long polymeric aromatic amides decompose between 520-580 °C.[104]

When observing the morphology of the polyamide materials it was found that there is a difference between the batches made with HOAc and without HOAc (Figure 4.5). The morphology was examined using an optical microscope and was subsequently verified through scanning electron microscopy (SEM) (Figure 4.5). The product made without HOAc was found to be having enlongated fibre-like morphology. Meanwhile the product made with HOAc was spheroidal particles (potato-like). It appears that the addition of HOAc can modify the polarity of the medium, consequently altering the precipitation rate of the polyamide material from the reaction mixture once it is formed. This could lead to the difference in morphology observed.
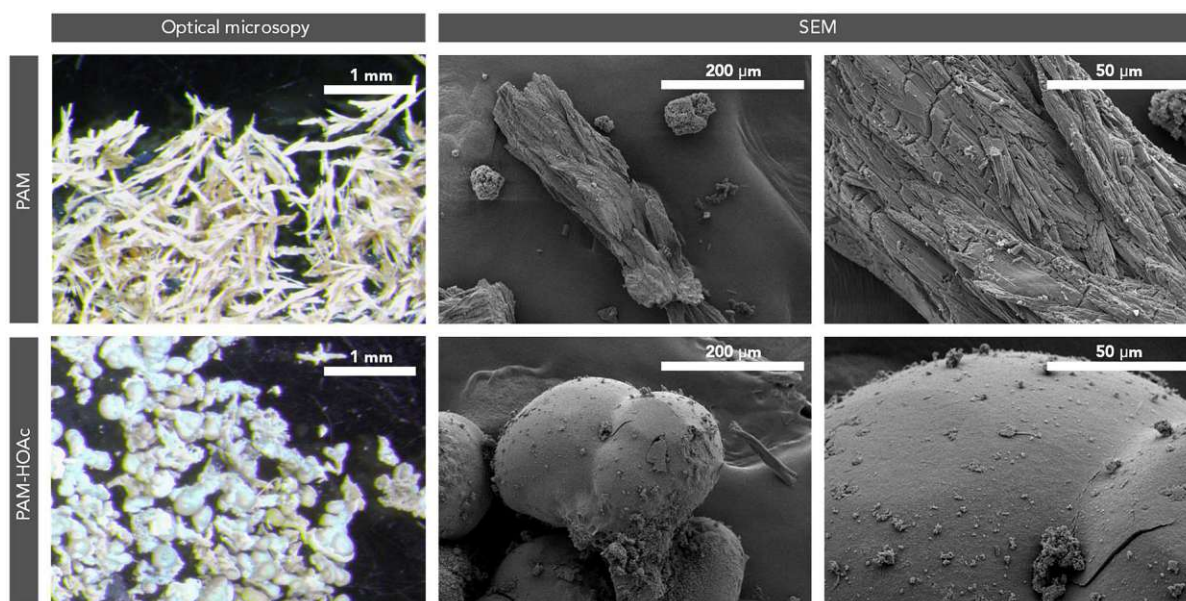
Figure 4.5: Morphology of PAM and PAM-HOAc in optical microscope and SEM.

4.1.3 Conclusion

In conclusion, the initial goal was the hydrothermal one-pot synthesis of fully aromatic extended covalent amide frameworks (CAFs). However, the outcome was the creation of a crystalline polyamide material, which is believed to be constituted by numerous fused polyamide macrocycles, similar to those present in a framework. This was achieved by building on prior works on the direct HT synthesis of crystalline aromatic heterocycles and Rosseinsky's approach on semi-aliphatic CAFs by HT treatment. This procedure is a stark contrast to classical synthetic route towards COFs, which rely on harsh and toxic conditions (*e.g.* mesitylene/dioxane mixtures). Their crystal structures, to that date still unknown, could also be refined from PXRD data. After screening it was found that HOAc, which is typically employed as a modulator to facilitate the formation of crystalline framework, had no effect in synthesis, except for the morphology of the material.

4.2 Hydrothermal synthesis of crystalline benzimidazole-linked organic materials

4.2.1 Introduction

Aromatic polybenzimidazoles (PBIs), are another class of high-performance polymers that have received considerable attention in recent years. They represent a class of high-temperature resistant/high-performance polymers that are attractive because of their outstanding mechanical and dielectric properties at high temperatures.[105,106] PBIs, such as Celazole®, have high values of limited oxygen index in combination with sufficient thermal stability to withstand extreme conditions without a substantial loss of properties.[107] To date, there are only very few prior reports of imidazole-linked COFs, but they employ toxic solvents like NMP, mesitylene or dioxane.[108-110] However, recently high-performance polymers like polybenzimidazoles and polypyrrolones have been prepared using nothing but high-temperature water as reaction medium.[90] Expanding upon this, the aim was to fabricate a crystalline polybenzimidazole covalent organic framework, by combining together Benzene-1,3,5-tricarboxylic acid/ Trimesic acid (TmA) and 3,3'-Diaminobenzidine (DABz) using water as the reaction medium to produce the extended 2D framework structures. To facilitate the dynamic covalent chemistry (DCC) ie. the breaking and reforming of bonds in the reaction condition, and to ensure that a crystalline framework was formed, a modulator was also introduced. A separate batch was created by adding acetic acid (HOAc) as a modulator: PBIM-HOAc. The obtained grey solid was found insoluble in water, THF, acetone, methanol and other common organic solvents.

4.2.2 Synthesis and characterizations

The strategy is to condense aromatic carboxylic acids with o-diamines hydrothermally to get imidazole linked product (Scheme 4.2a). Typically, syntheses were carried out by suspending TmA and DABz in water and heating the reaction mixture to hydrothermal regime (200 °C) in a closed steel autoclave (Scheme 4.2b). After HTP, the solid was isolated *via* filtration and then washed with water, ethanol and acetone until the washing solution appears clear. The solid is dried at 80°C under vacuum.
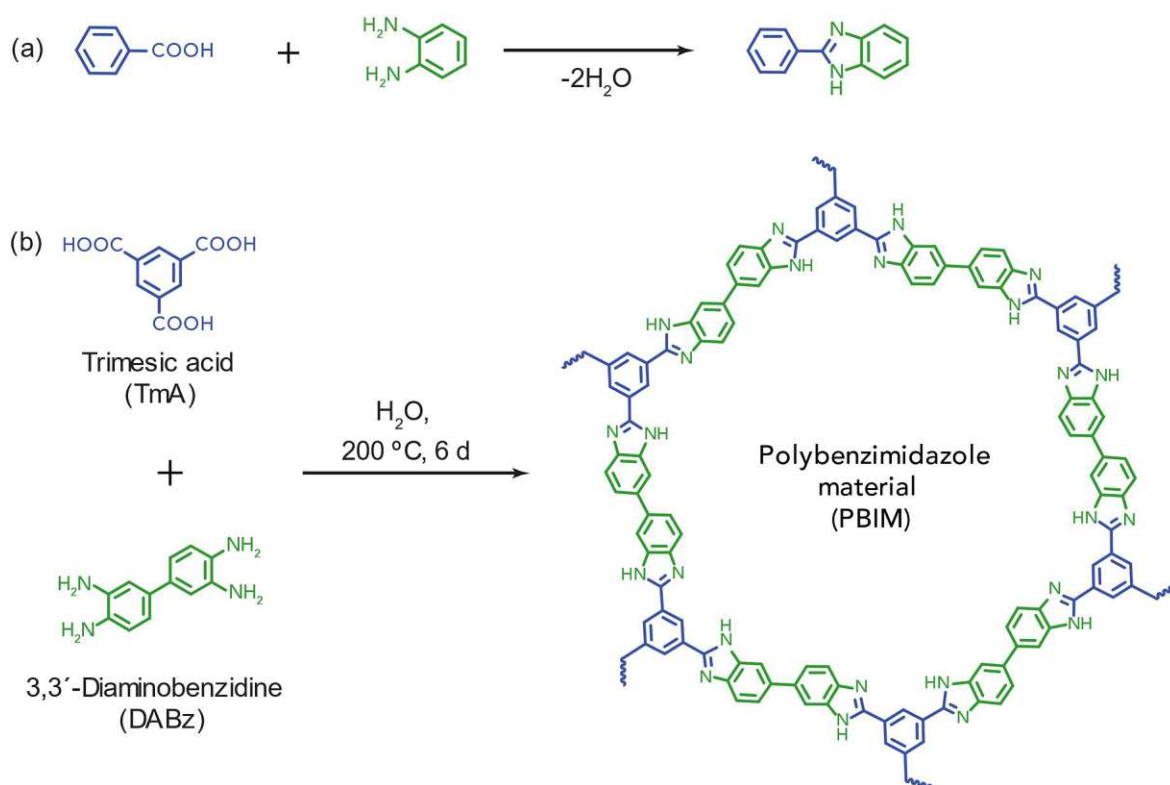
Scheme 4.2: a) Strategy to get imidazole linked product by condensation of aromatic carboxylic acid with o-phenylenediamine. b) Synthesis of PBIM from TmA and DABz

Formation of benzimidazole linkage can be confirmed by the absence of IR modes present in TmA and DABz respectively, as well as by the presence of bands caused by imidazole ring. In the FT-IR spectra (Figure 4.6), the absence of strong NH_2 doublet band located at ~ 3400 cm^{-1} and new C=N stretching modes (~1600 cm^{-1}) of the network were visible from t_R=18 h

onwards (refer section 5.2.2). Even after prolonged reaction times (t_R= 6 days), there were still C=O stretching bands (~1700 cm^{-1}) in IR, confirming the presence of peripheral -COOH groups in both batches. Moreover, several modes in the H-bonding region (~3400 cm^{-1}- 2800 cm^{-1}) further point at -COOH endgroups.
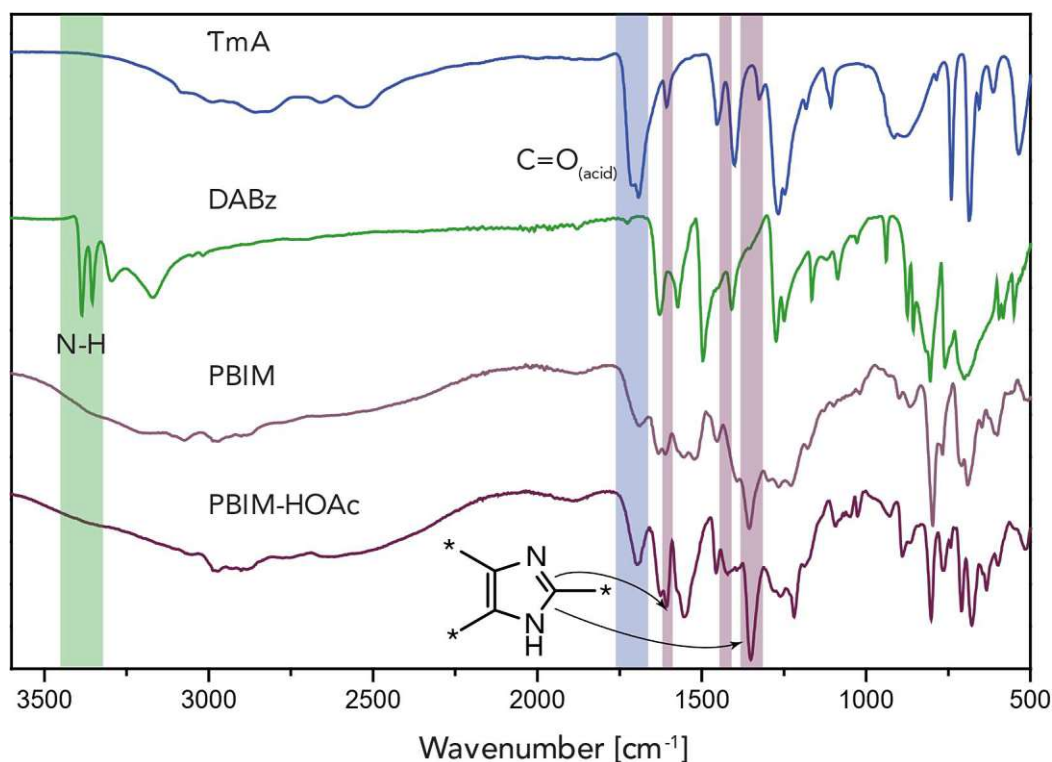
Figure 4.6: FT-IR spectra of TmA, Bz, PBIM and PBIM-HOAc

The chemical connectivity of the PBIMs (AC, T_R= 200 °C, t_R= 6d) were further confirmed by ^{13}C cross polarization magic angle spinning (CP-MAS) NMR (Figure 4.7). The chemical shifts in the range 100-130 ppm in the NMR spectrum can be ascribed to phenyl carbon atoms PBIMs. The peaks corresponding to imidazole unit can be seen around 140 ppm, thereby confirming the presence of imidazole linkages. But the observed signal at 162 ppm showed the presence of the carbonyl carbon, can be due to peripheral -COOH which confirms FT-IR analysis.
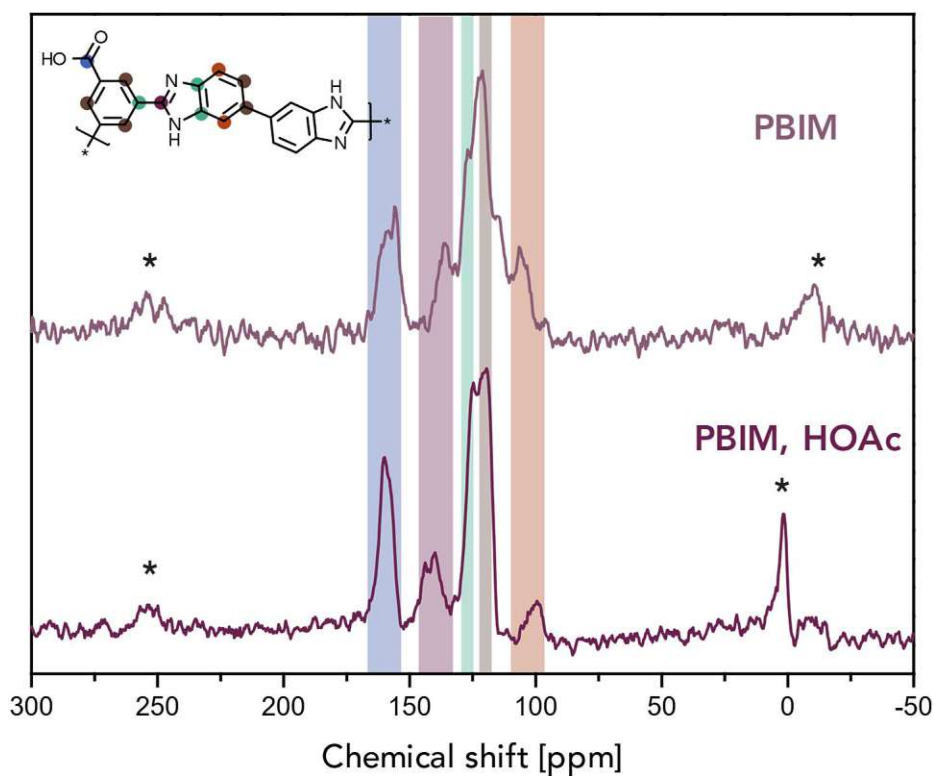
Figure 4.7: ^{13}C CP-MAS solid state NMR spectra of PBIM and PBIM-HOAc. * indicates peaks arising from spinning side bands.
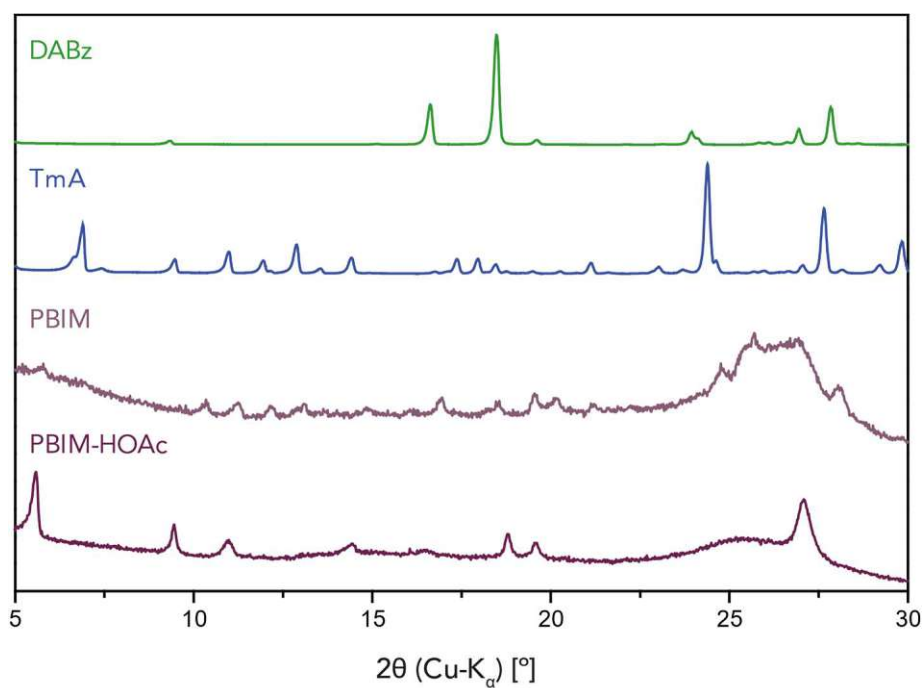
Figure 4.8: PXRD patterns of TmA, DABz, PBIM and PBIM-HOAc

When the PXRD pattern of the synthesized PBI materials (AC, T_R= 200 °C, t_R= 6d) were investigated, it showed that PBIM-HOAc had very sharp reflections compared to PBIM (Figure

4.8). PBIM-HOAc was obtained as polycrystalline powder. Unfortunately, due to its poor solubility in H_2O and alcohols, no single crystals could be obtained via recrystallization. The crystallinity of the products was monitored with PXRD pattern, it showed very weak peaks for the sample till t_R= 3 days, whereas at t_R= 6 days the PBIM-HOAc products with good crystallinity were confirmed by their PXRD patterns (refer section 5.2.3).

The small angle region shows that there are regular frameworks within the PBIM-HOAc (AC, T_R= 200 °C, t_R= 6d, with HOAc). In addition, small angle X-ray scattering (SAXS) revealed that PBIM-HOAc have a hexagonal lattice arrangement (Figure 4.9). In PXRD, the (001) diffraction peak at 2θ= 27.1° corresponds to an interlayer distance of 3.28 Å, suggesting a typical Vander-Waals contact between the aromatic layers in PBIM-HOAc. An effort was made to correlate the PXRD pattern with simulated patterns derived from multiple optimized COF structures that could potentially form within the system. However, none of these comparisons yielded an exact match (refer section 5.2.4). Consequently, it is inferred that the PBIM-HOAc is having structure similar to COF but not as extended frameworks.
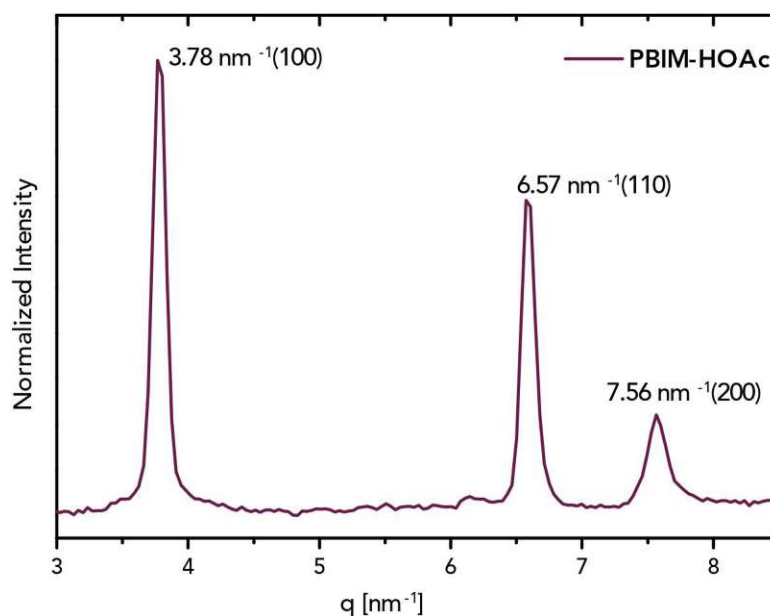
Figure 4.9: SAXS pattern of PBIM-HOAc (AC, T_R= 200 °C, t_R= 6d, with HOAc).

The thermal stability of PBI materials (AC, T_R= 200 °C, t_R= 6d) were investigated by collecting thermogravimetric analysis data. The results exhibited that PBI materials features significant thermal structural stability up to 350 °C (Figure 4.10) and both batches showed similar TGA curves. TGA shows mainly 3 weight loss slopes in both batches when kept for longer reaction time.
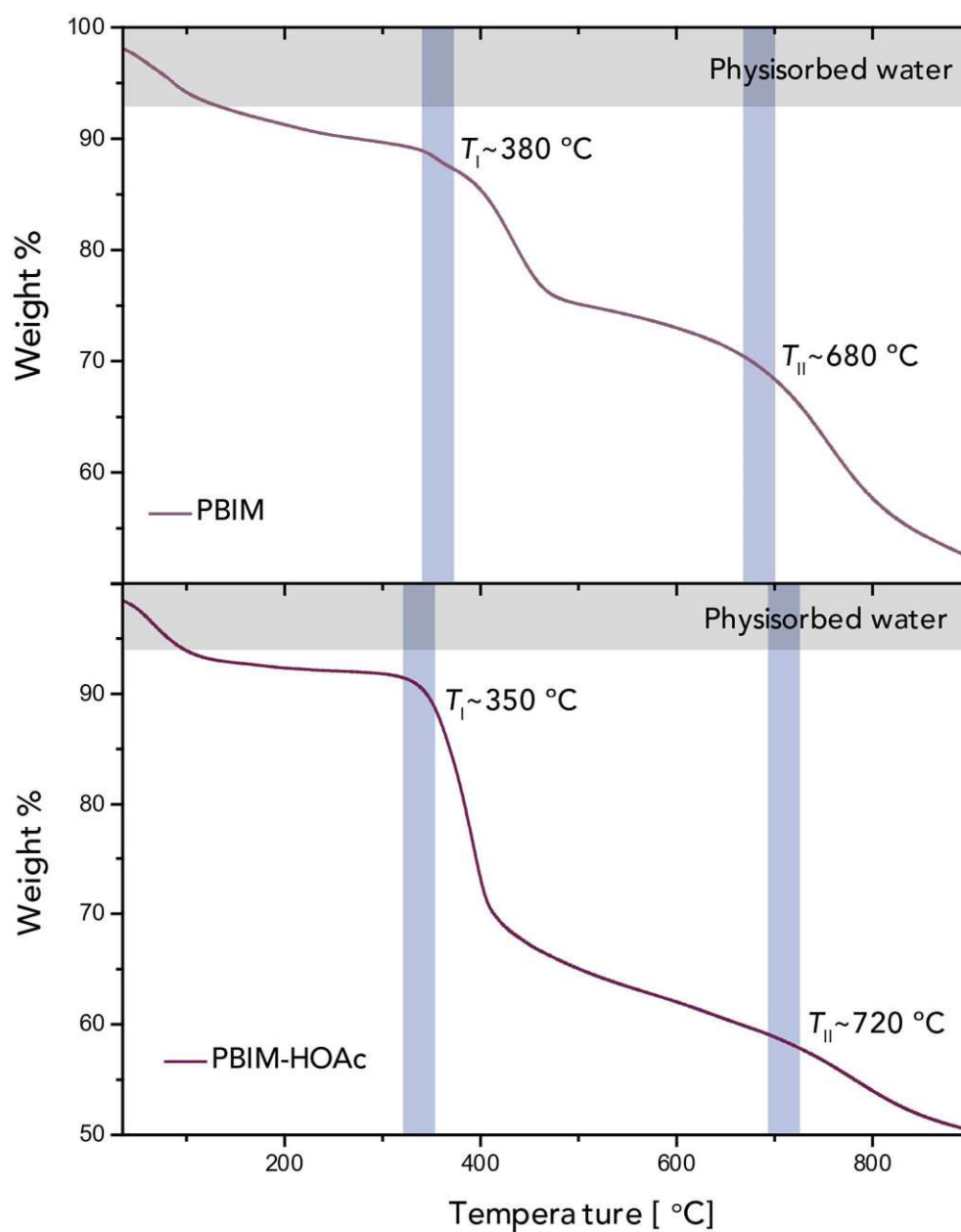
Figure 4.10: TGA curve of PBIM and PBIM-HOAc

An initial weight loss occurs in the range of 80-100 °C in all samples, which can be attributed to the removal of moisture and trapped gas. The next weight loss occurred in the temperature range of 350-400 °C (T_I) and was associated with the decomposition of peripheral -COOH groups in PBIMs and trapped small oligomers.[111] Then a final weight loss in the broad range around ~700 °C (T_{II}). This could be associated with the total decomposition of the PBI material with large polymer size, which is usually >600 °C. It was also observed that with an increase in the reaction time, the slope shifts towards higher temperatures. This shift signifies the enlargement of the framework's size.
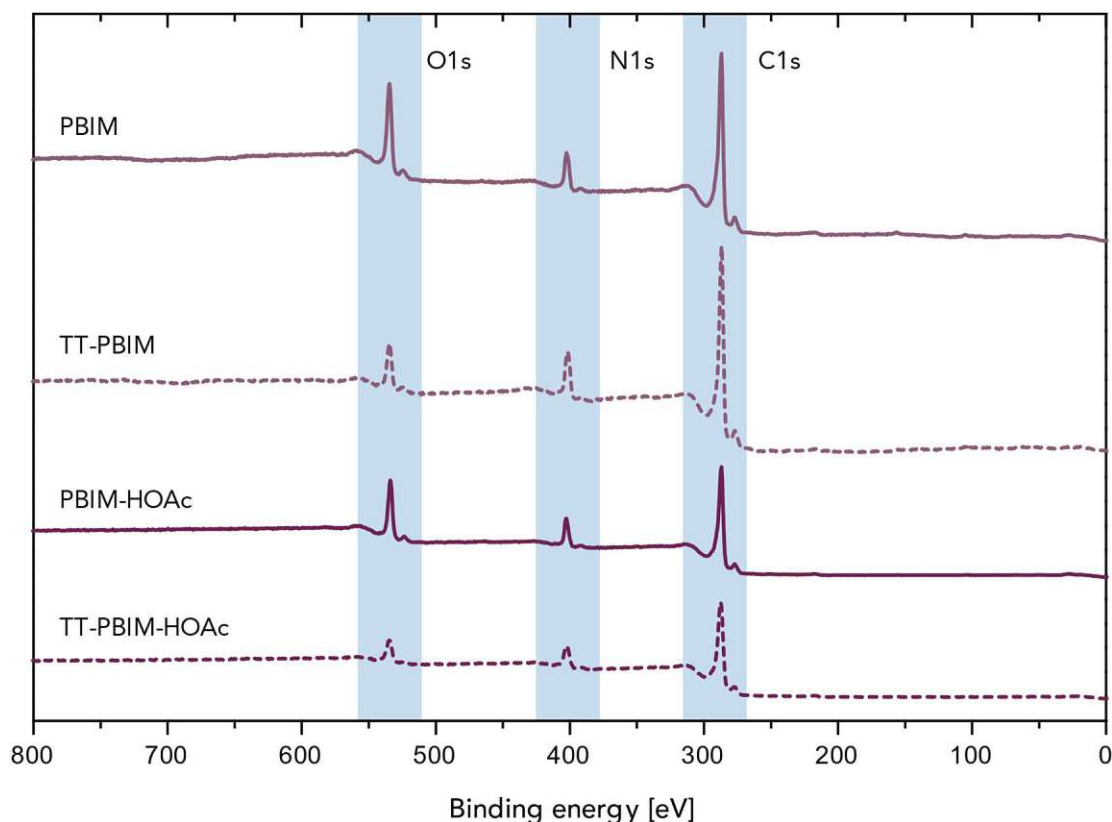
Figure 4.11: Full XPS survey spectra

The decarboxylation of PBIMs at elevated temperatures and the chemical connectivity of the materials were confirmed by XPS analysis. Both pristine PBIMs and thermally treated PBIMs (TT-PBIMs) were studied. TT-PBIMs were prepared by annealing PBIMs at 400 °C under nitrogen atmosphere. The XPS survey spectra of PBIMs showed three dominant peaks centered

at 284.5, 339.5, and 532.4 eV, corresponding to the presence of C1s, N1s, and O1s respectively (Figure 4.11). One notable change after the thermal treatment is the considerable decrease in the intensity of the O1s peak. This result indicated that a substantial portion of peripheral -COOH groups were stripped off.

The deconvoluted high-resolution C1s spectra further confirmed changes in chemical bonds before and after thermal-treatment (Figure 4.12a-b). The intensity of the deconvoluted C1s peak due to -COOH bonds (red box) was reduced after the heat treatment. Therefore, these results provide further evidence for the selective removal of peripheral carboxyl groups.
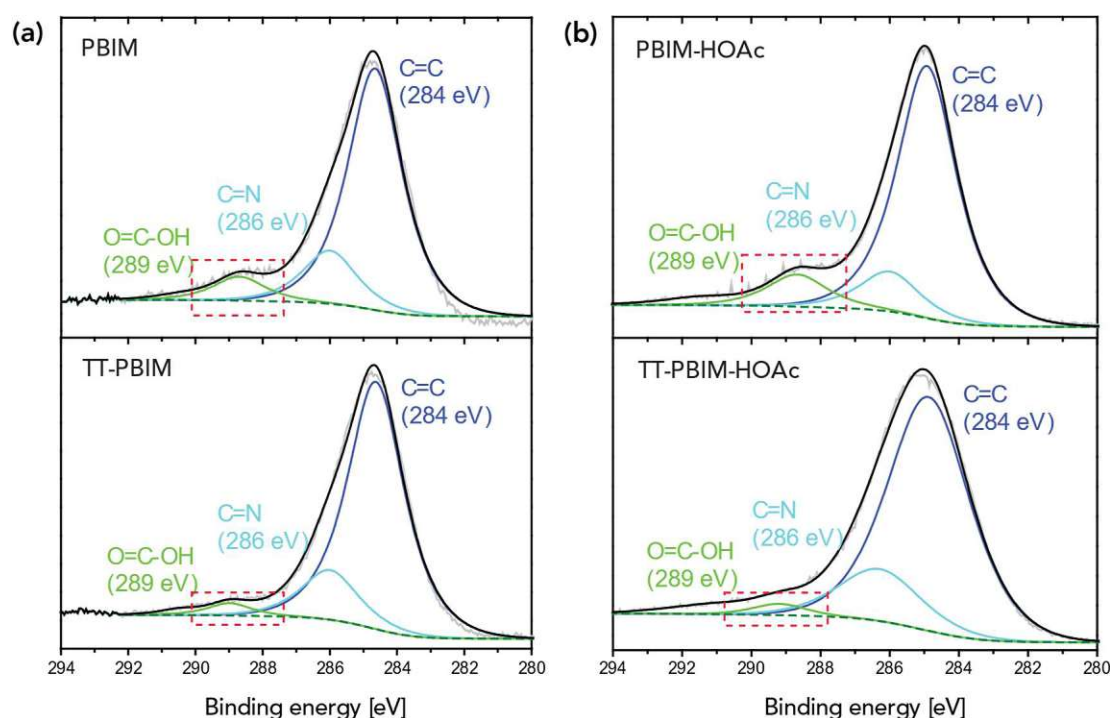
Figure 4.12: High-resolution C1s spectra: a) PBIM and TT-PBIM; b) PBIM-HOAc and TT-PBIM-HOAc

The morphology of the PBI materials (AC, T_R= 200 °C, t_R= 6d) were studied under SEM. The micrographs of PBIM and PBIM-HOAc show significantly different morphologies (Figure 4.13a). PBIM showed flake-like or flower shaped morphology, which often corresponds to crystallinity. While the PBIM-HOAc exhibited micro-structures like thick sheets and tubules.

It has been reported that crystallites of similar organic frameworks can aggregate and fuse together to form a sheet-like structures due to high pressure and hydrophobicity of the polymer. To minimize unfavorable and destabilizing interactions in water they further undergo bending and scrolling to form tubular arrangements (Figure 4.13b).[112] These observed morphologies were indicative for crystallinity and layered structure.
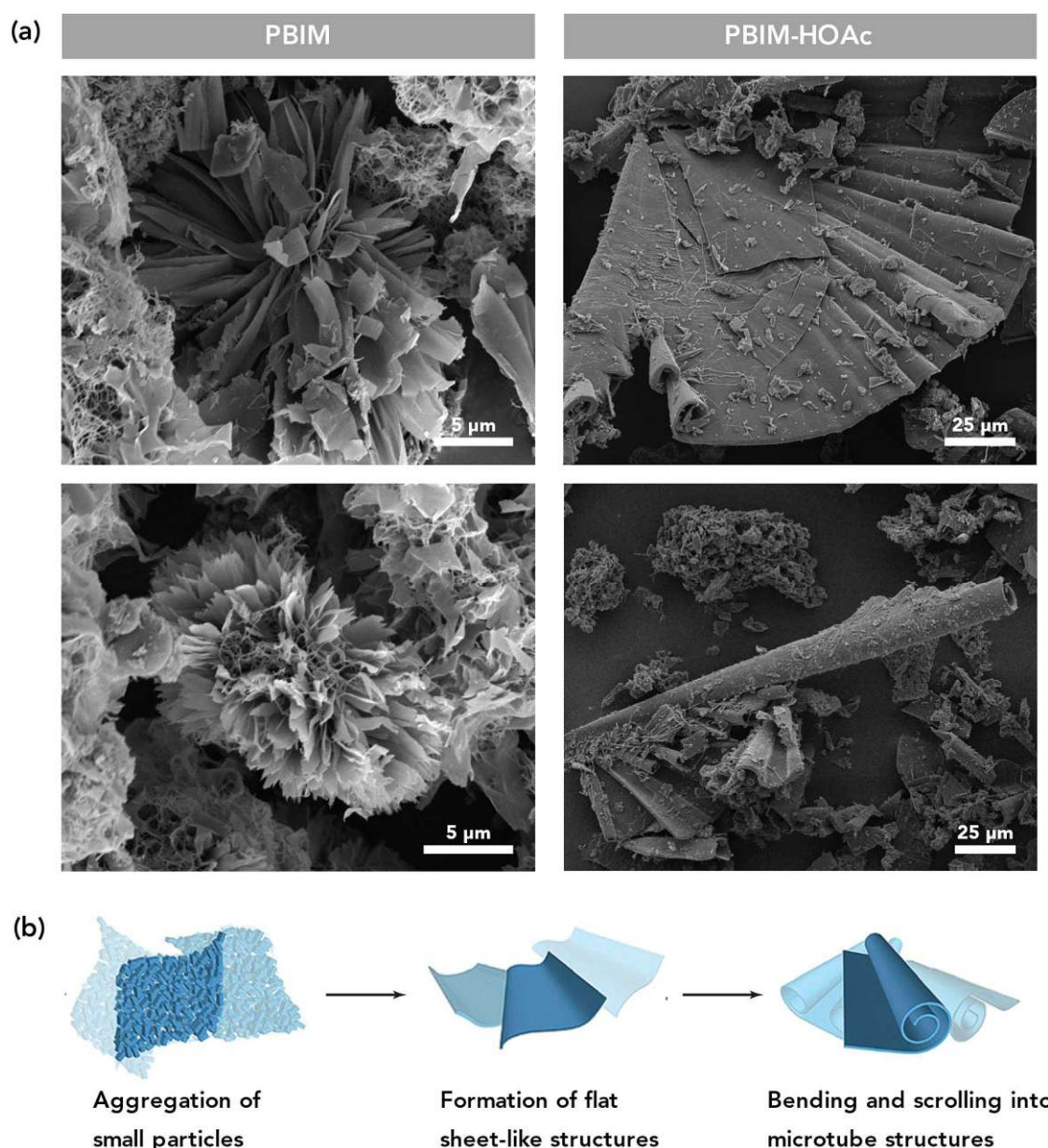
Figure 4.13: a) SEM micrographs of PBIM and PBIM-HOAc. b) Proposed mechanism of self-assembly of PBIM-HOAc into microtubes.[112]

4.2.3 Conclusion

In summary, crystalline PBI materials were successfully produced through hydrothermal methods. Different reaction parameters were screened to identify the optimal conditions for obtaining crystalline PBI material. The formation of benzimidazole linkage was confirmed with help of FT-IR and ^{13}C ssNMR spectra. The crystal structure data indicates that the product did not possess an extended COF structure but rather a fused hexagonal macrocyclic structure. The generated PBI materials exhibited interesting tunable morphologies indicative for crystallinity and layered structure. This work further confirms that HT synthesis is capable of generating crystalline organic materials, with good thermal stability.

4.3 Hydrothermal synthesis of polybenzimidazoles and their conversion into polypyrrolones

4.3.1 Introduction

Ever since the discovery of first representatives of synthetic polymers, such as the phenolic resin bakelite[113], they have been connected to applications as materials for use in machines and devices. Therefore, synthetic polymers, from a materials science point of view, are typically subdivided into 3 performance classes: (i) commodity polymers, (ii) engineering polymers and (iii) High-performance polymers (HPPs)[114]. The pricing and production/usage volume of these classes scale accordingly. Commodity polymers, such as polyethylene, are relatively inexpensive and extensively used, while HPPs can cost up to thousands of USD/Kg and are used in low quantities in high end applications. These classes are typically represented by the price-performance pyramid of synthetic polymers (Figure 4.14).
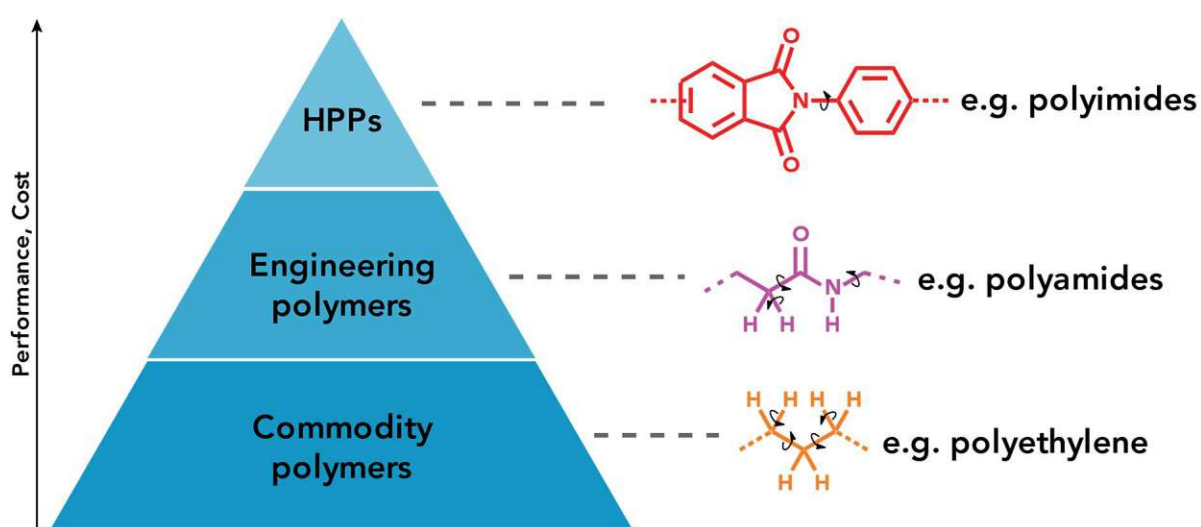
Figure 4.14: Price-performance-pyramid of synthetic polymers and its examples

Performance is measured relatively to the materials property thermal stability, but also scaled accordingly with other properties such as, chemical resistance and mechanical performance. These properties are in turn a direct consequence of the molecular structure, with which the price-performance pyramid also correlates.

Polybenzimidazopyrrolones or simply, Polypyrrolones (PPys) are an example of HPP with superior properties due to their rigid backbones and fused heterocyclic linkages. Conventionally, PPy synthesis comprises of two-step condensation. The two common synthetic procedures for PPys are: (i) controlled and stepwise heating of the neat monomers in polyphosphoric acid yielding PPy particles, which can be processed by high-T molding;[64,115] (ii) stirring the neat monomers at room temperature in polar aprotic solvents such as N-methyl-2-pyrrolidone (NMP), dimethylformamide (DMF), dimethylacetamide (DMAc) to form a poly(amide amino acid) intermediate, which can be subsequently processed into fully condensed PPy films or fibres after a final thermal annealing step at T ≥ 300 °C.[65,116,117] However, these synthetic procedures show two significant drawbacks: (i) harsh and toxic solvents are required; (ii) poor processability.

Harsh and toxic organic solvents could be replaced with green hydrothermal synthesis. From previous reports it has been conclusively shown that it is possible to generate polyimides[88,89] and other aromatic heterocyclic compounds[92,93] using nothing but high-temperature water as the reaction medium. Taking inspiration from that, it was reported that polybenzimidazoles and pyrrolone polymers can also be generated by the same HT synthesis.[90] This current work provide insight into preparing other PPys hydrothermally and expanding its scope and the number of hydrothermally generated polymers.

The application of microwave (MW) energy is considered a promising method for the synthesis of organic compounds and polymers. Remarkable decrease in the reaction time, uniform heating and in some cases, cleaner reactions with easier workup are some of the main

advantages of using MW synthesis. In synthetic polymer chemistry, many examples of the use of MW irradiation can be seen such as in emulsion polymerization of acrylates, radical polymerization of vinyl monomers, annealing of epoxy resins, cross-linking of polyolefins and also the imidization of polyamic acids.[118] But so far, there are only very few reports on the complete synthesis of condensation polymers from respective monomers via the use of MW reactor. However, in our previous report on PPy, it was emphasized that PPys could be synthesized using microwave-assisted methods in water.[90] In this study, the polymers were synthesized via MW-assisted HT method followed by thermal annealing to achieve fully condensed PPys. Subsequently a comparison was drawn between the outcomes obtained from the non-stirred steel autoclave (steel bomb), typically used for high-temperature HT synthesis and MW-assisted HT method.

Second drawback, due to the rigid polymer backbone and relatively high density of PPys, they typically lack solubility in organic solvents, and processing is hence limited to sintering or hot pressing. This has been the major limitation for the application of PPys. However, to additionally fine-tune the properties, flexible single-chain segment in the polymer backbone was introduced by using appropriate monomers, which results in a semi-ladder structure. It has been previously reported that, this is effective in improving their solubility and processability.[119-121] The previous PPys that were prepared, PP5 & PP6 (Figure 4.15a, b), were also insoluble. In this study, monomers with certain rotatable bonds and groups that would impart greater free volume and render them more processable were implemented. Keeping this in mind, 2 kinds of PPys were generated with 3,3'-Diaminobenzidine (DABz) and various dianhydrides: 3,3′,4,4′-Benzophenonetetracarboxylic dianhydride (BTDA) and 4,4-(Hexafluoroisopropylidene) diphthalic anhydride (6FDA) (Figure 4.15c, d).
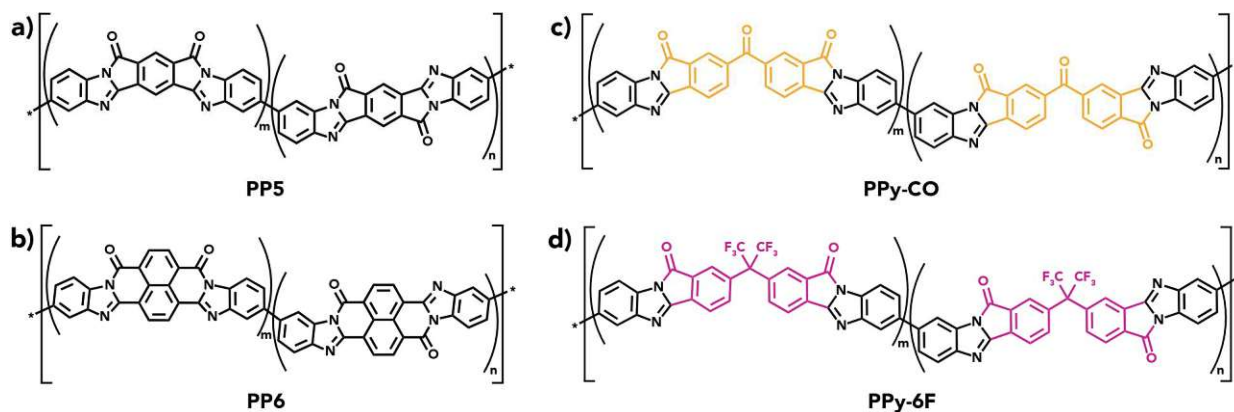
Figure 4.15: Hydrothermally synthesized PPys: a) PP5, b) PP6, c) PPy-CO, d) PPy-6F

4.3.2 Synthesis and characterizations
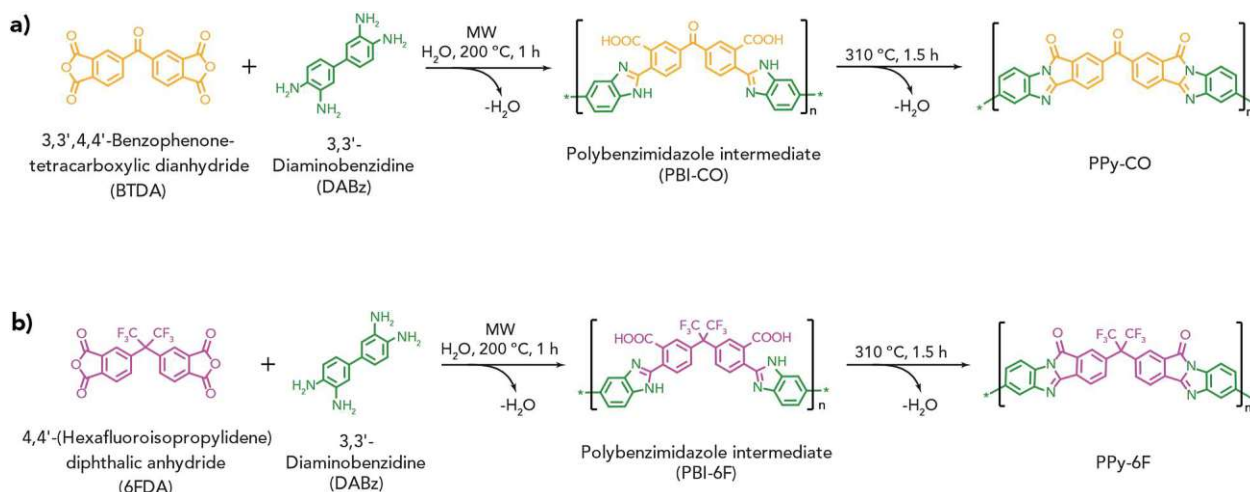
Scheme 4.3: MW-assisted HT synthesis of PBI-intermediate followed by thermal annealing to yield PPy-CO (a) and PPy-6F (b).

In this study to synthesise the pyrrolone polymers, the tetraamine monomer, DABz was reacted with the dianhydride monomers, BTDA and 6FDA to yield the polymers PPy-CO (Scheme 4.3a) and PPy-6F (Scheme 4.3b) respectively. Our initial strategy was to prepare the PPys directly via MW-assisted HT synthesis. So, the required monomers were suspended in distilled water inside a MW glass vial, followed by stirring at room temperature (RT). The reaction mixture was then heated to hydrothermal regime at 200 °C under autogenous pressure

along with stirring in a MW reactor. But from analysing the ATR-FTIR spectrum of the product, the characteristic C=O bands of PPy (~ 1760 cm^{-1}) were absent. In accordance with previous PPy report,[90] three intermediate structures seemed probable (Figure 4.16): (i) An initial condensation might generate of a poly(amide amino acid) (PAAA), which is also seen in conventional solvo-thermal synthesis. By a next condensation step two different species could form: (ii) a poly(imide amine) (PI-NH$_2$) or (iii) a poly(benzimidazole acid) (PBI-COOH). But the product's ATR-FTIR spectrum showed neither amide nor imide modes, yet it showed the presence of imidazole modes. Therefore, the material obtained was concluded to be PBI-COOH.
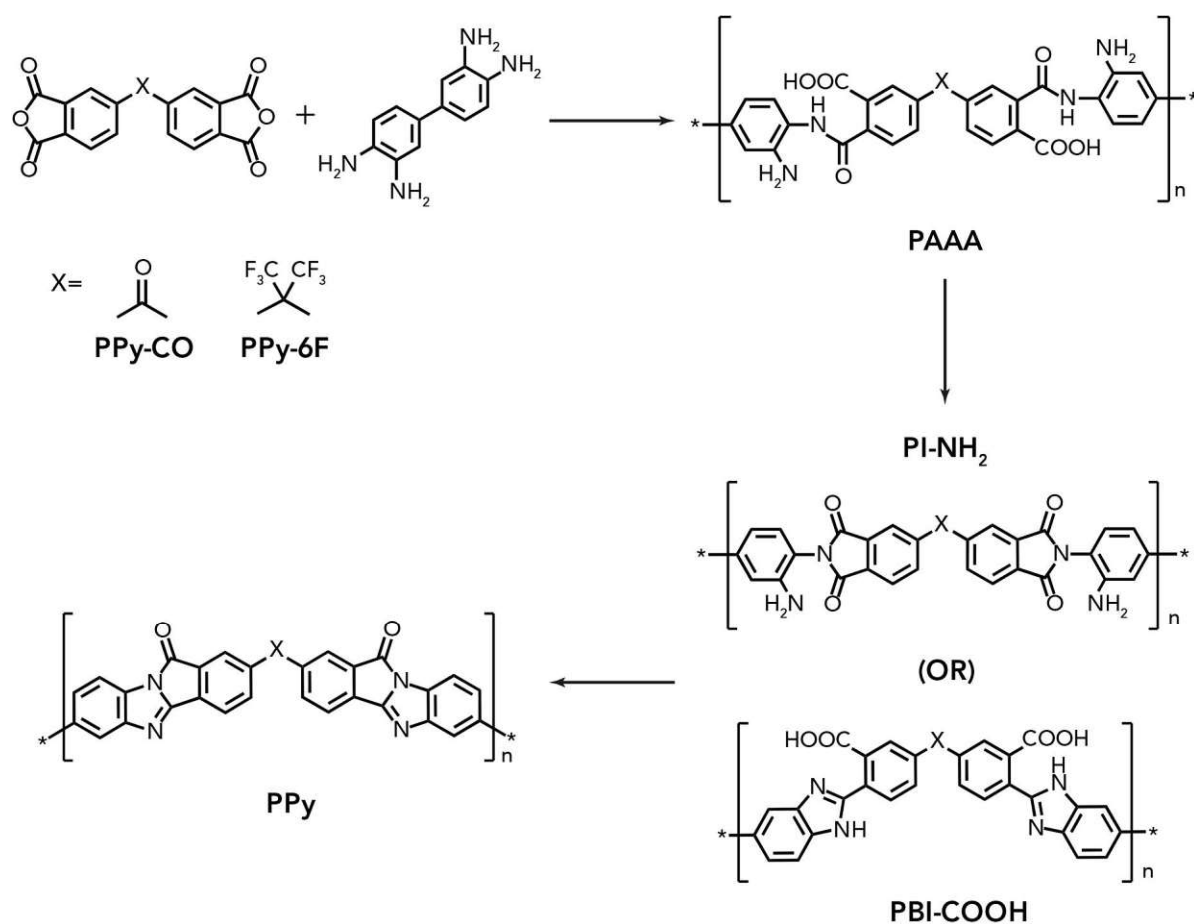
Figure 4.16: An overview of the formation of possible intermediates (PAAA, PI-NH$_2$, PBI-COOH) and PPy.

From the previous literatures, it was found that fully condensed PPy can be obtained through the second ring closure of PBI-COOH, by solvent-free heat treatment under inert atmosphere.

45

Therefore, the PBI-COOH intermediate was thermally cured at 310 °C under N_2 atmosphere. ATR-FTIR analysis of the final product was nicely in accordance with the previous literature. All characteristic modes were present, including C=O(PPy) mode. Also, the modes indicating incomplete ring closure (amide, imide, amino, carbonyl/carboxyl) were absent.

The successful product formation was verified using ATR-FTIR spectroscopy (Figure 4.17). The ATR-FTIR spectra of both PBI-intermediates (PBI-CO and PBI-6F) showed absence of modes due to carboxylic anhydride (BTDA ~1738 cm^{-1}, 1700 cm^{-1}; 6FDA ~1849 cm^{-1}, 1776 cm^{-1}) and amine groups (~3400 cm^{-1}) present in the monomers, as well as by the presence of combined C=C/C=N ring vibration mode (~1620 cm^{-1}), the benzimidazole in-plane vibration mode (~1450 cm^{-1}) and the C-N stretching mode (~1360 cm^{-1}) indicate product formation. After the thermal annealing, a new absorption band at ~1760 cm^{-1} appeared. This was assigned to the characteristic stretching vibration of C=O in pyrrolone groups, along with other modes indicative for the formation of the fully condensed PPy products were visible.
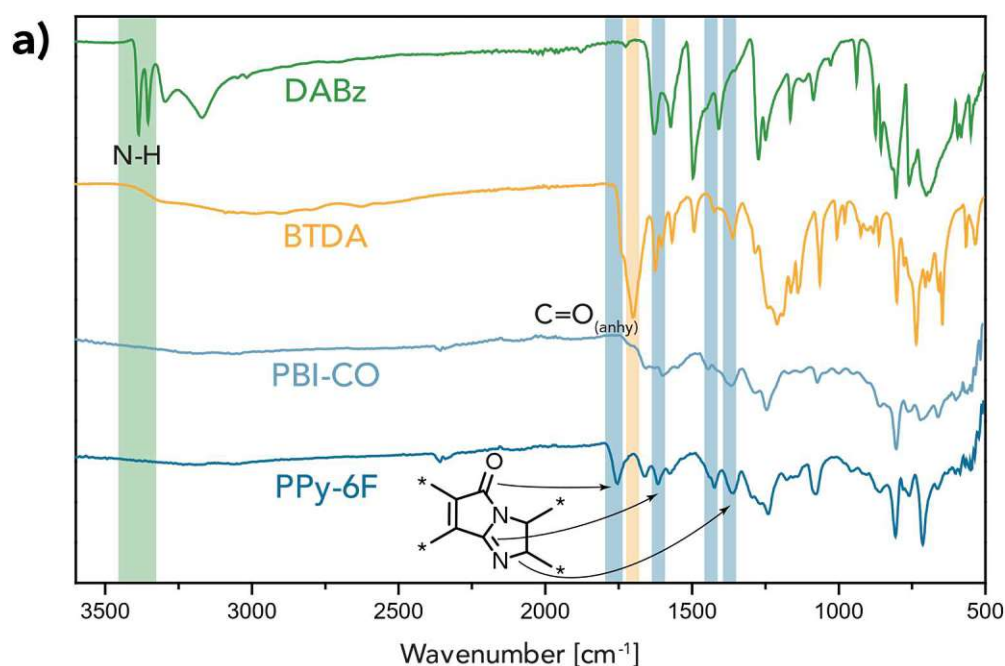
Figure 4.17: a) FT-IR spectra DABz, BTDA, PBI-CO and PPy-CO
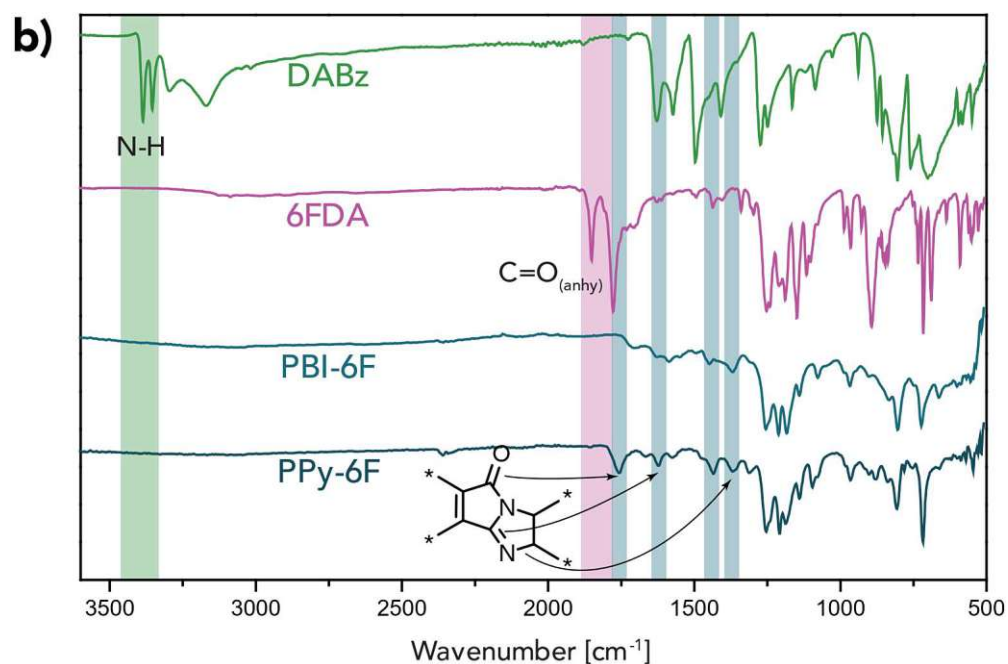
Figure 4.17: b) FT-IR spectra of DABz, 6FDA PBI-6F and PPy-6F

The chemical connectivity of the PPys were further confirmed by ^{13}C cross polarization/magic angle spinning (CP-MAS) NMR (Figure 4.18).
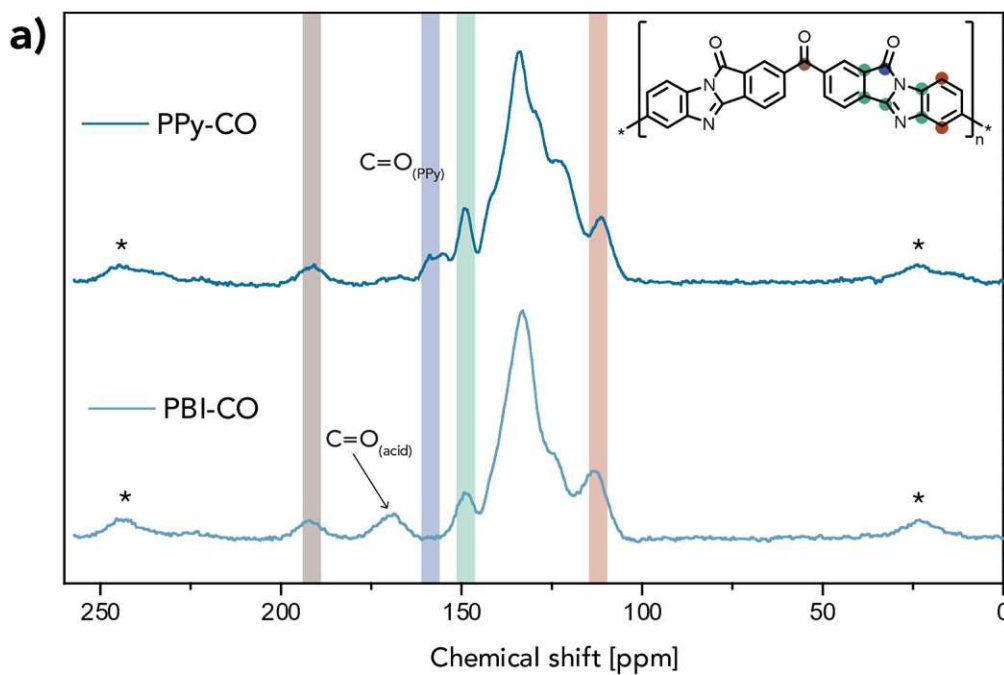
Figure 4.18: a) ^{13}C CP-MAS NMR spectra of PBI-CO and PPy-CO

47
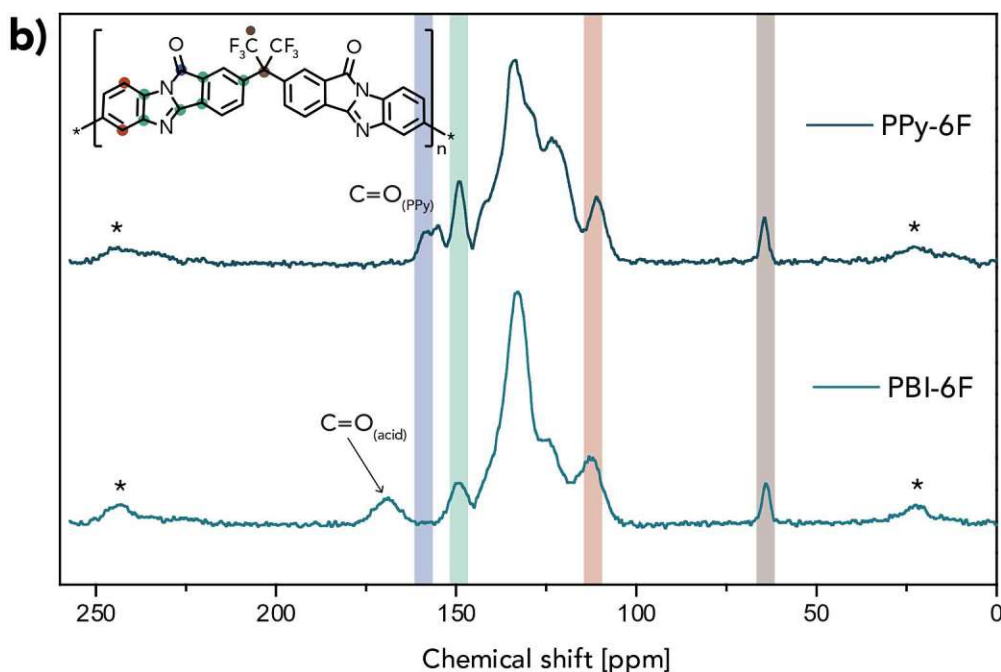
Figure 4.18: b) ^{13}C CP-MAS NMR spectra of PBI-6F and PPy-6F

The chemical shifts in the range 100-140 ppm in the NMR spectrum could be ascribed to phenyl carbon atoms and the peak at ~150 ppm showed the presence imidazole ring carbons of PPy and PBI-intermediates. The signal at ~170 ppm of the PBI-intermediates confirms the presence of unreacted -COOH groups. The observed signal at ~158 ppm showed the presence of the carbonyl carbon in PPys, thereby confirming the double cyclization and formation of perinone-type linkage of PPy.

The PXRD patterns of both PBI-intermediates and PPys indicated that the polymers were amorphous (Figure 4.19). Unfortunately, not much improvements were observed in PXRD patterns after t_R= 15min (refer section A.1.2). The amorphous nature of the polymer can be attributed to the presence of the non-coplanar biphenyl moiety from the amine monomer and the flexible anhydride monomer. Even though the PXRD pattern shows amorphous polymer regions, some information can be gathered even from this. In amorphous polymers no long-range order exists, but a short-range order of most probable distances such as distance between neighbouring chains (intersegmental spacing) and length of the repeating unit (intrasegmental

distance) do exist. The presence of short-range order is the cause of the broad halos observed in the diffraction pattern for non-crystalline polymers.[122] These distances or d-spacing, can be calculated using Bragg's equation (Table 4.1).

The first d-spacing, 3.5–3.6 Å, indicates segments of the polymer matrix with tight packing. In comparison, a tightly packed material such as graphite exhibits a d-spacing of 3.3 Å and has virtually no available "free space". The second d-spacing in the smaller 2θ region of the polymers studied here, indicates segments of greater chain disruption. It is evident that these repeating segments in the polymer backbone are shifted or lost after thermal annealing.
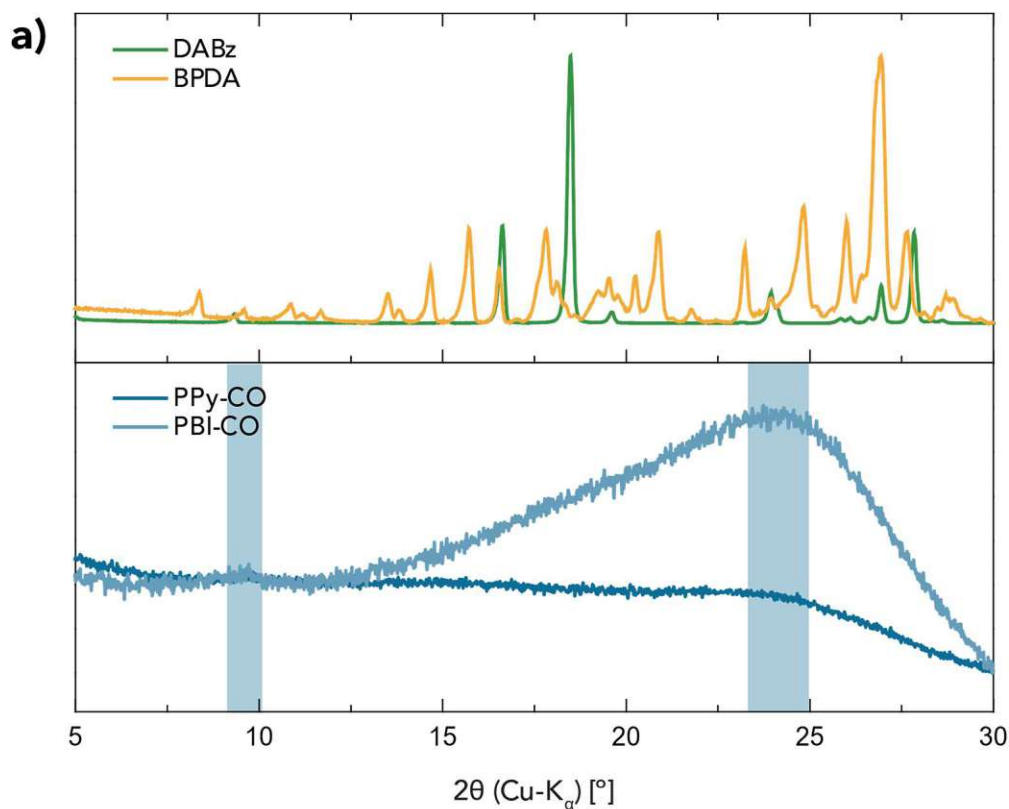
Figure 4.19: a) PXRD pattern of PBI-CO and PPy-CO
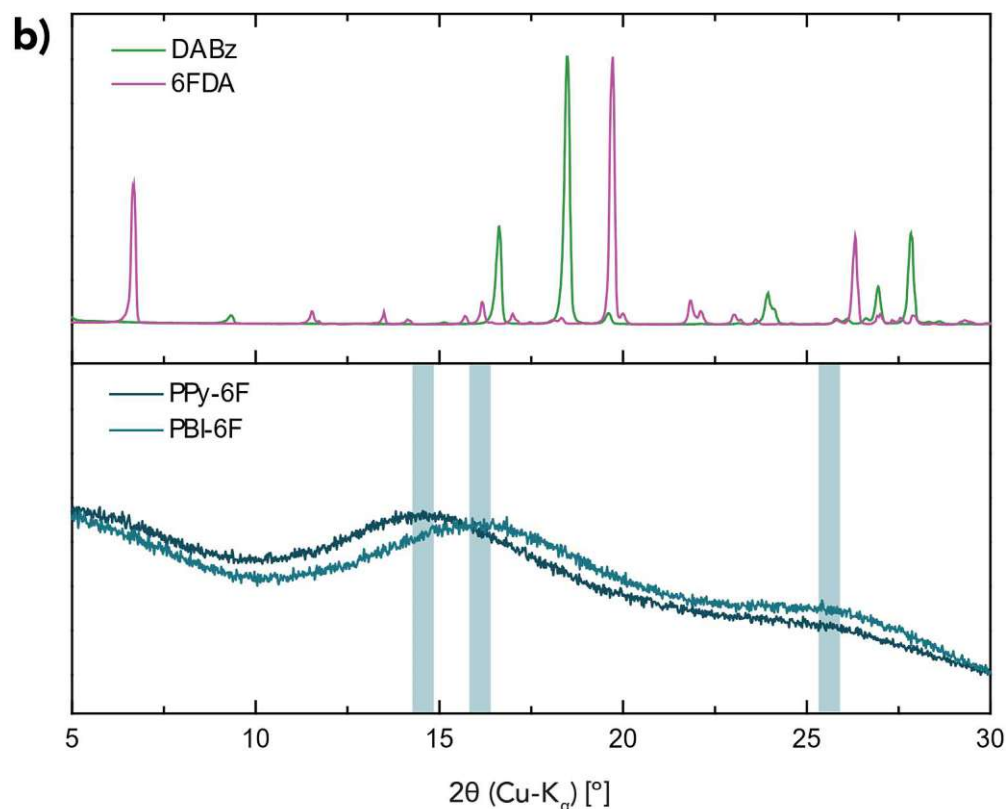
Figure 4.19: b) PXRD pattern of PBI-6F and PPy-6F

Table 4.1: Calculated d-spacing of PBI-intermediates and PPys

	2θ (Cu-Kα)	d-spacing
	º	Å
PBI-CO	9.5; 24.2	9.3; 3.67
PPy-CO	24.2	3.67
PBI-6F	16.1; 25.4	5.5; 3.5
PPy-6F	14.6; 25.4	6.06; 3.5

The thermal properties of both PPys were investigated by TGA (Figure 4.20) and the results are summarised in Table 4.2. An initial weight loss was seen around ~100 °C in both samples, which can be attributed to the removal of moisture and trapped gases. Further, the PBI-intermediates showed a slope around 250 °C, which is due to condensation of pyrrolone ring.

At this temperature the PBI-intermediates undergoes condensation and gets converted to PPy polymers, similar to the process occurring during thermal annealing. The mass loss during the thermal annealing process was calculated by-

$$Mass\ loss = \frac{Mass\ of\ PBI\ intermediate - Mass\ of\ PPy\ polymer}{Mass\ of\ PBI\ intermediate} * 100$$

The observed mass loss due to the ring closure from the TGA curve was matching with the calculated mass loss of the polymers. Thus, the conversion of PBI-intermediates to fully condensed PPys were confirmed. Both polymers showed good thermal stability above 500 °C. Considering the measured degradation temperature, these materials exhibit considerable thermal stability, which most likely results from the linkage and ladder structure.[68]

Also, the residual weight at 900 °C increased after annealing, which further confirms that thermal annealing completes the condensation to form a stable polymer. Polymers with 6FDA fractions exhibit a greater weight loss. This weight loss likely results from the evolution of the heavier fluorine atoms, which are more plentiful in 6FDA fraction polymers- PBI-6F and PPy-6F.

Table 4.2: Thermal properties of PBI-intermediates and PPys

	T_d	R_w	Mass loss (obs)	Mass loss (cal)
	°C	%	%	%
PBI-CO	530	57.1	6.53	6.79
PPy-CO	528.5	63.1	-	-
PBI-6F	524.6	50.7	5.77	5.52
PPy-6F	533.3	56.2	-	-

T_d- thermal decomposition temperature; R_w- residual weight at 900°C.
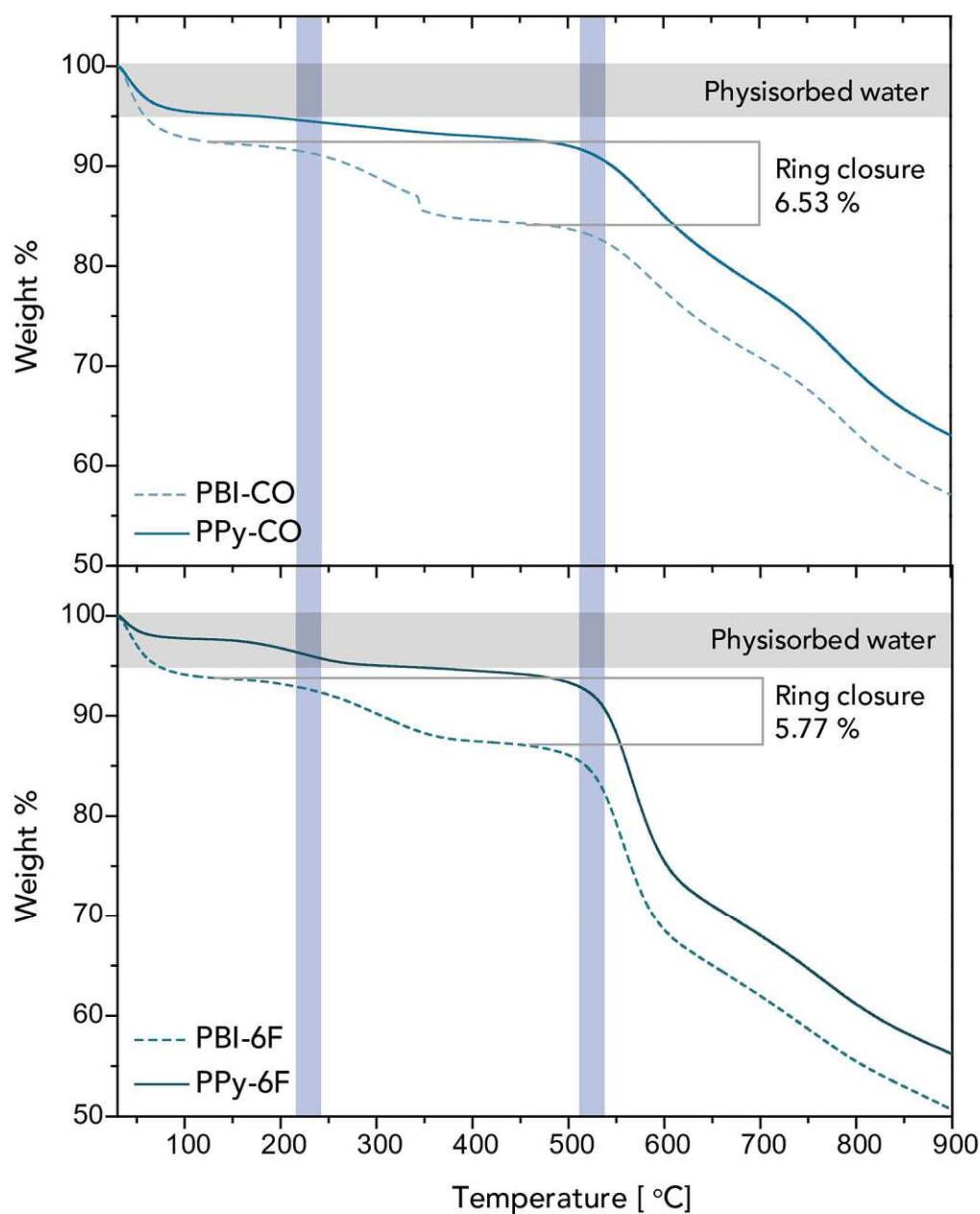
Figure 4.20: TGA curve of a) PBI-CO and PPy-CO; b) PBI -6F and PPy-6F

The morphology of the PPys were studied with scanning electron microscope (SEM). The micrographs of PPys and PBI-intermediates show that they are strikingly similar and are mostly spherical agglomerates (~2-5 µm in diameter) (Figure 4.21). This suggest that the conversion of PBI-intermediates to PPy take place solely in the solid state, without undergoing melting or softening phenomena during the transformation. But the polymers made with BTDA appear different from those made with 6FDA when observed directly (Figure 4.22). A color change

52

was also observed in both polymers after thermal annealing, the materials changed to an intense shade. This can correlate to increased conjugation of the PPy polymers after ring closure due to the condensation of PBI-intermediates.
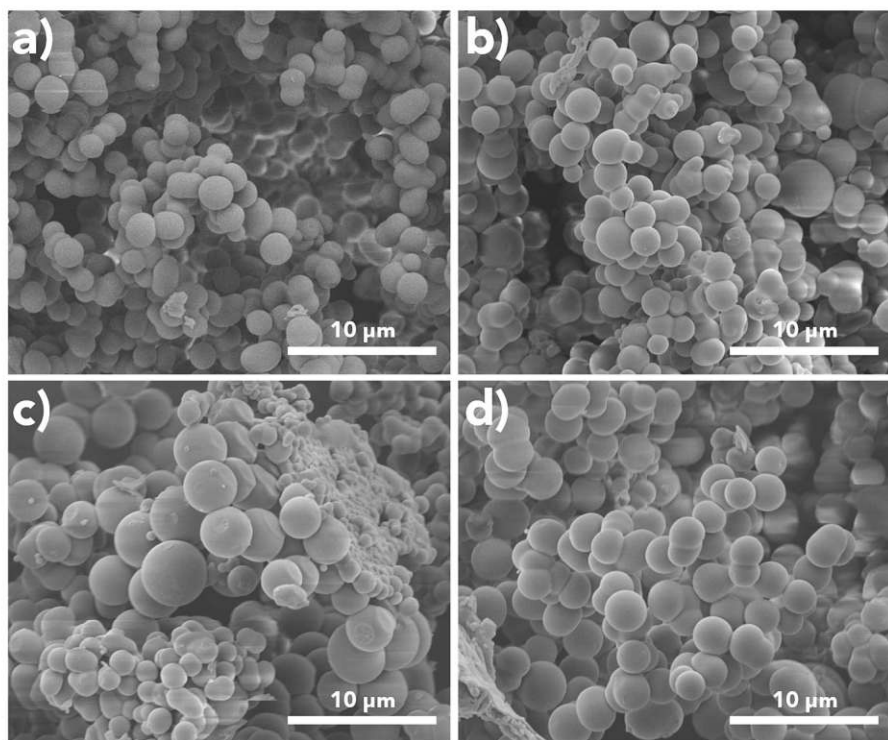
Figure 4.21: SEM images of a) PBI-CO; b) PPy-CO; c) PBI-6F; d) PPy-6F
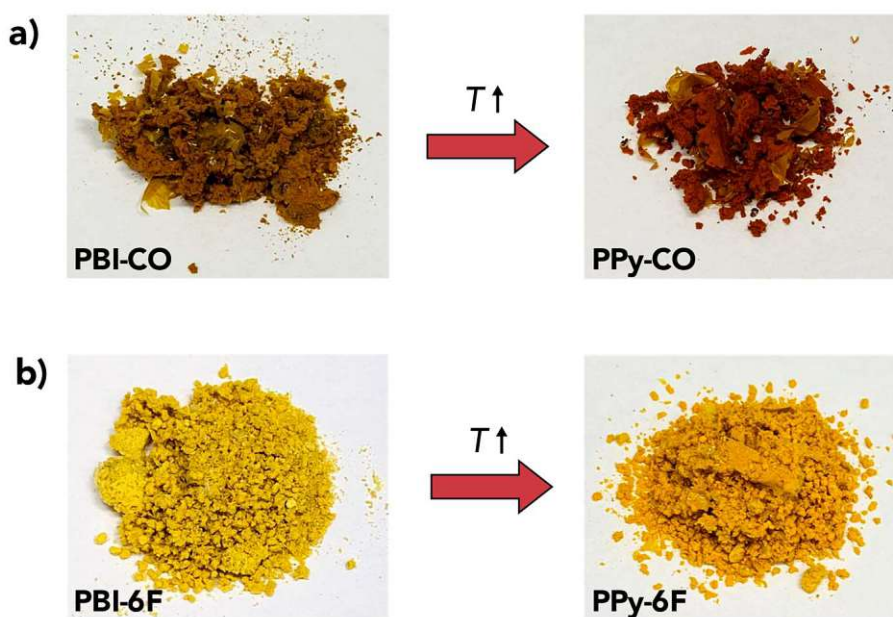
Figure 4.22: Morphology and colour of a) PBI-CO and PPy-CO; b) PBI-6F and PPy-6F

4.3.3 Insight into product formation

The PBI-COOH intermediates and PPy products synthesised in this study were amorphous. Even though, the so far reported HT synthesis typically generates crystalline products. The main reasons, we believe behind the amorphicity and morphology observed in the polymers can be due to:

i. The non-coplanar biphenyl moiety from the amine monomer and the flexible anhydride monomer.

ii. The monomer systems show rapid condensation in the given reaction condition to yield the respective PBI-COOH intermediate, thus forward reaction is favoured leading to faster polymerisation over the reverse reaction and subsequent error-correction.

iii. As a result of the low miscibility of precursors even at HT conditions, it is most likely that the polymerisation follow mechanism similar to suspension polymerisation. In the reaction medium, insoluble monomer droplets undergo polymerization on a microscopic scale, gradually becoming spherical solid polymer particles.[123] This hinder bond reversibility and error-correction, hence the formation of the thermodynamic, crystalline product is prevented.

The MW-assisted HT synthesis reproducibly afforded monodisperse PBI-COOH particles. Since this not the thermodynamic product (lowest energy state), this can be further exploited for processing. The two possibilities of processing in bulk are (i) drop casting of the PBI-COOH intermediate in suitable solvent and subsequent annealing to yield PPy films (ii) simultaneous annealing and processing via moulding or hot pressing.
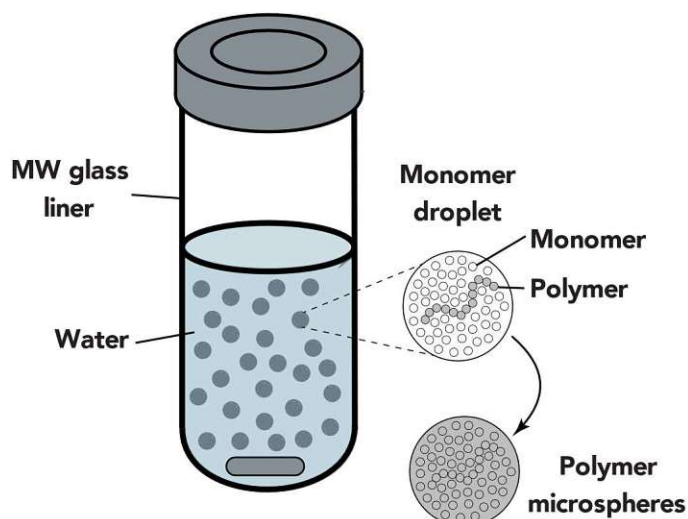
Figure 4.23: Representation of polymerization process in MW-assisted HT synthesis. Monomer droplets act as separate microreactors having the same kinetics as in bulk polymerization.[123]

4.3.4 Conclusions

Through this contribution, it was demonstrated for the first time that a rapid, straightforward, and environmentally friendly MW-assisted HT synthetic method can be applied to generate polybenzimidazoles. These polybenzimidazoles could be subsequently converted to PPys through thermal annealing, eliminating the need for complex procedures. The final PPy product shows high temperature stabilities (>500 °C) and therefore qualifies as HPP. These PPy products show interesting and identical spherical morphologies. With careful tuning of reaction conditions and using appropriate flexible aromatic tetra-amine and dianhydrides, fine dispersions of PPy could be successfully created in appropriate solvents. This could help in the processability of these polymers, while sustaining the intrinsic thermal stability. These good, combined properties make the PPys good potential candidates for high-tech applications, which can be produced in bulk via environmentally benign synthetic route.

5. Experimental Details

5.1 Hydrothermal synthesis of crystalline amide-linked organic materials

5.1.1 Hydrothermal synthesis of PAM and PAM-HOAc

Hydrothermal synthesis of PAM

A glass tube was charged with trimesic acid (42.03 mg, 0.2 mmol), benzidine (55.27 mg, 0.3 mmol) and water (5 mL). The mixture was sonicated for 5 min at room temperature (RT). The tube was placed in a Teflon liner and sealed in a steel autoclave. The autoclave was kept in a oven preheated to 200 °C, where it was held for t_R = 1 to 6 days. Afterwards, the autoclave was allowed to cool down to RT under ambient conditions. The autoclave was opened and the solid was isolated via filtration and washed with water (3 x 10 mL), ethanol (3 x 10 mL) and acetone (3 x 10 mL), then dried at 80 °C under vacuum yielding PAM as a very pale-yellow needle shaped solid.

Hydrothermal synthesis of PAM-HOAc

PAM-HOAc was synthesised according to the similar experimental polymerisation procedure to that explained above, except that to the reaction mixture 6M HOAc (0.3 mL) was added after sonication. The product was dried at 80°C under vacuum yielding PAM-HOAc as light grey spherical shaped globules.

Both batches, PAM and PAM-HOAc, were screened at various t_R ranging from 1 day to 6 days, to identify the optimum reaction conditions (summarized in Table 5.1). The products

were analysed with ATR-FTIR spectroscopy and PXRD to confirm chemical connectivity and crystallinity.

Table 5.1: Screening for optimum t_R and T_R

Precursors (ratio in mmol)	AcOH (mL)	H$_2$O (mL)	Reactor	T_R (°C)	t_R
TmA:Bz (0.2:0.3)	-	5	Autoclave	200	1d
TmA:Bz (0.2:0.3)	0.3	5	Autoclave	200	1d
TmA:Bz (0.2:0.3)	-	5	Autoclave	200	4d
TmA:Bz (0.2:0.3)	0.3	5	Autoclave	200	4d
TmA:Bz (0.2:0.3)	-	5	Autoclave	200	6d
TmA:Bz (0.2:0.3)	0.3	5	Autoclave	200	6d
TmA:Bz (0.2:0.3)	-	10	Ampoule	200	4d
TmA:Bz (0.2:0.3)	-	10	Ampoule	200	5d

5.1.2 ATR-FTIR spectra

The progress of the reaction was monitored with ATR-FTIR spectroscopy (Figure 5.1). The complete conversion to product was confirmed by the absence of FT-IR modes of TmA and Bz, as well as by the presence of new bands caused by amide-linkage. It is evident that the C=O (acid) band is getting gradually reduced and C=O (amide) band is gradually increasing. There is an initial reduction of C=O (acid) band, but not much difference after t_R= 4 days. It is also evident from the FT-IR spectra that presence of modulator has not altered the chemical conversion, as both spectra are almost identical.
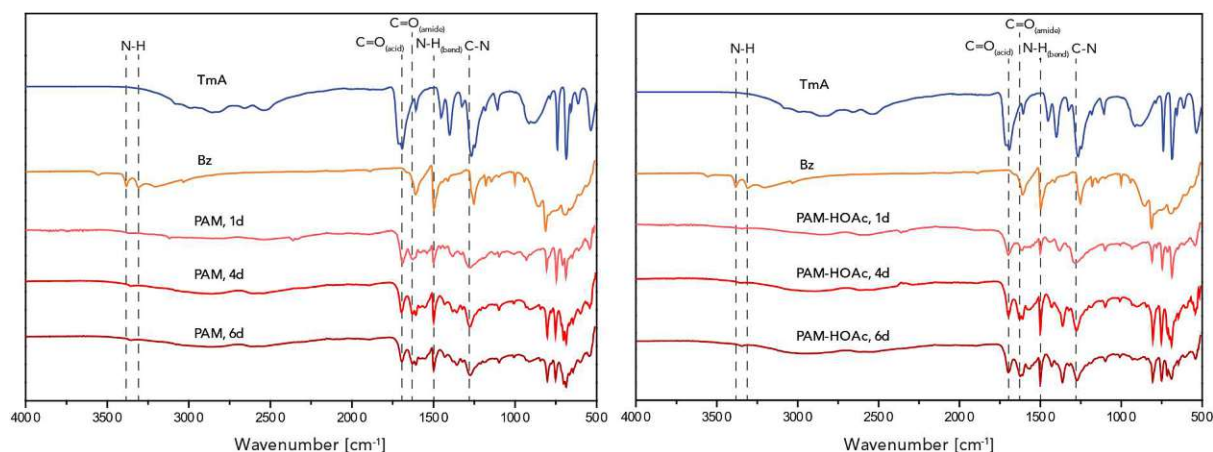
Figure 5.1: FT-IR spectra of TmA, Bz, PAM (T_R= 200 °C, t_R= 1d, 4d, 6d) and PAM-HOAc (T_R= 200 °C, t_R= 1d, 4d, 6d)

5.1.3 PXRD analysis

Based on experimental PXRD results, the obtained solids exhibited high crystallinity and long-range order as a result of HT synthesis. Moreover, the observed Bragg peaks of the products were found to be different from the ones of the respective monomers. From t_R= 4 day onwards, crystalline framework-like pattern was achieved. It also became evident that the addition of acetic acid as a modulator did not play a major role to promote the formation of an extended framework.
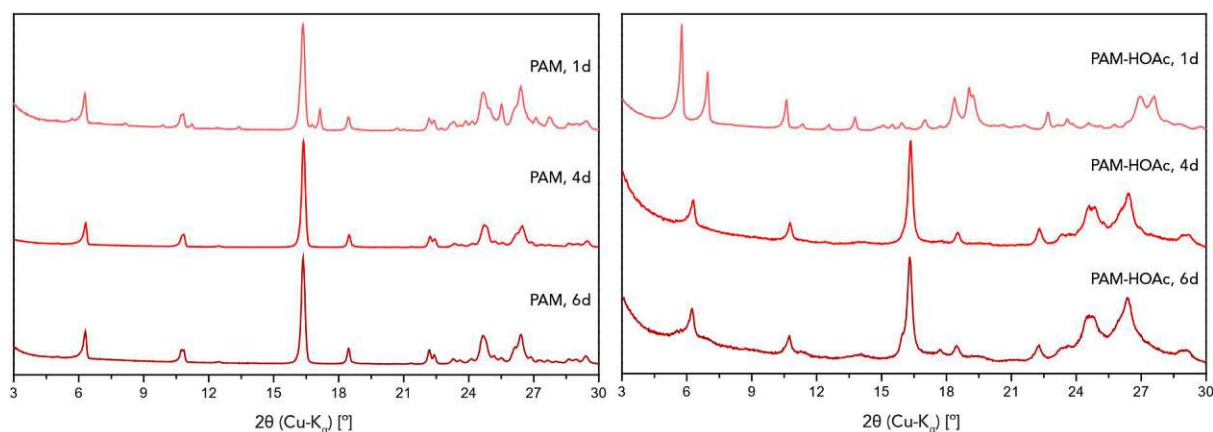
Figure 5.2: PXRD pattern of PAM (T_R= 200 °C, t_R= 1d, 4d, 6d) and PAM-HOAc (T_R= 200 °C, t_R= 1d, 4d, 6d)

5.1.4 Structural modelling and PXRD simulations

To better understand the structure and to confirm whether a framework is formed, hypothetical frameworks were constructed using Materials Studio software. Following geometric energy minimization, PXRD patterns were simulated from these frameworks, and a comparison was made with the experimental PXRD pattern (Figure 5.3). But none of the simulations were exactly matching the experimental PXRD results.
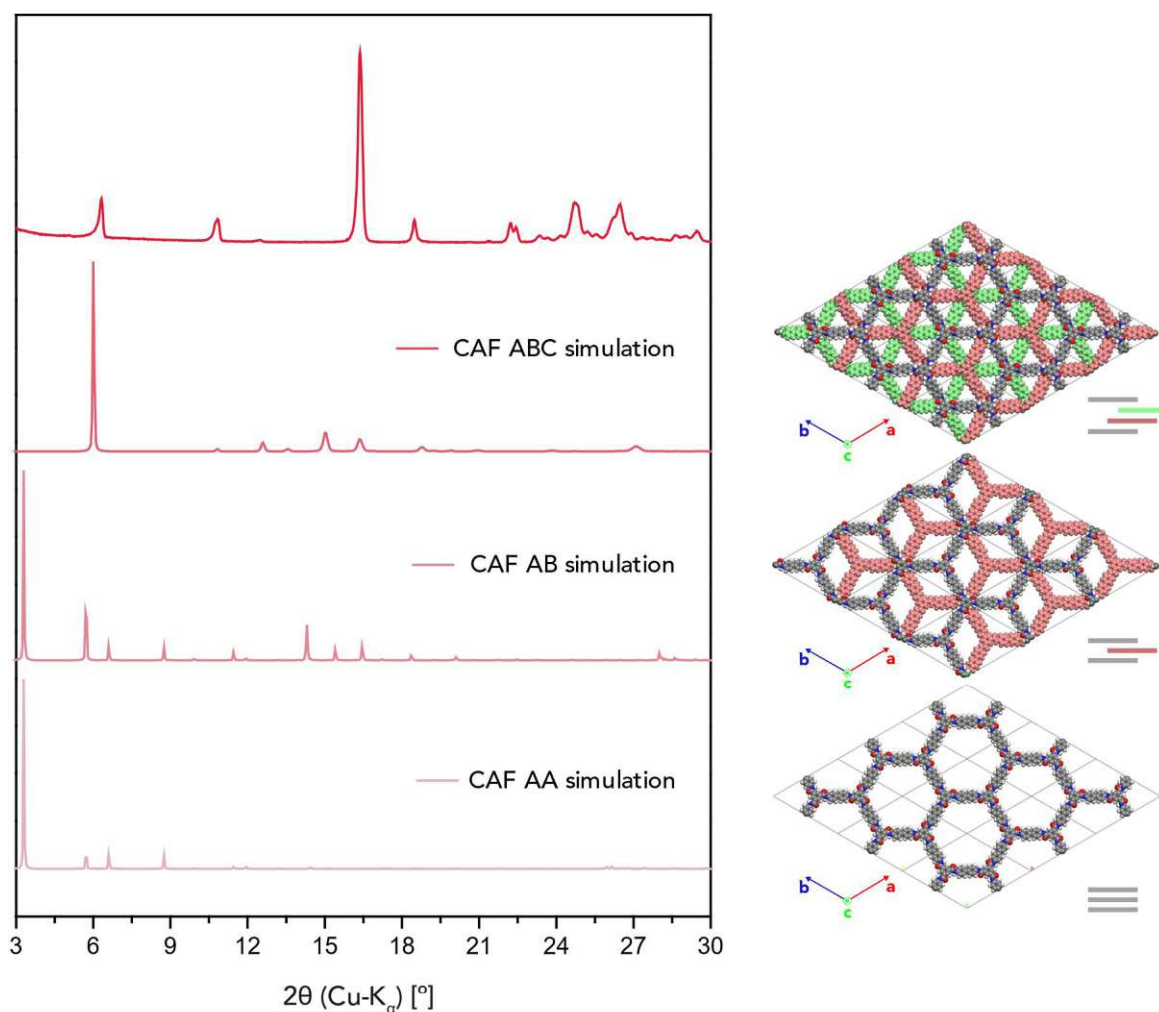
Figure 5.3: Comparison of PAM (T_R= 200 °C, t_R= 4d) with simulated PXRD patterns of various stacking arrangements in CAF.

Since there were unreacted -COOH groups present in the material, there was a possibility of forming amide-linked macrocycles with peripheral -COOH groups. Optimized structures of potential macrocycles were also generated, and their simulated PXRD patterns were compared

with the experimental PXRD pattern (Figure 5.4). Nonetheless, a match between the two patterns could not be established.
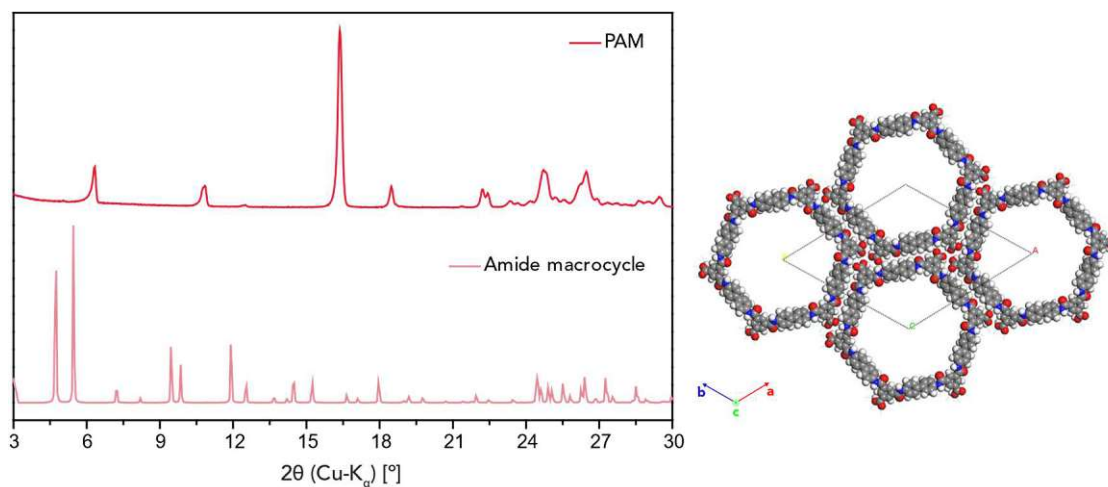
Figure 5.4: Simulated PXRD patterns of amide-linked macrocycle

The ABC stacked 2D framework (Figure 5.5) displayed the closest resemblance to the PAM diffraction pattern. Subsequently, attempts were made to refine the simulated structure. Although the refined structure exhibited remarkable similarity, it did not exactly match the experimental pattern. The unit cell parameters were obtained after geometrical energy minimization and pawley refinement for ABC stacked framework (Space group = R-3, a = b = 26.99 Å, c = 6.52 Å, α = β = 90°, γ = 120°)
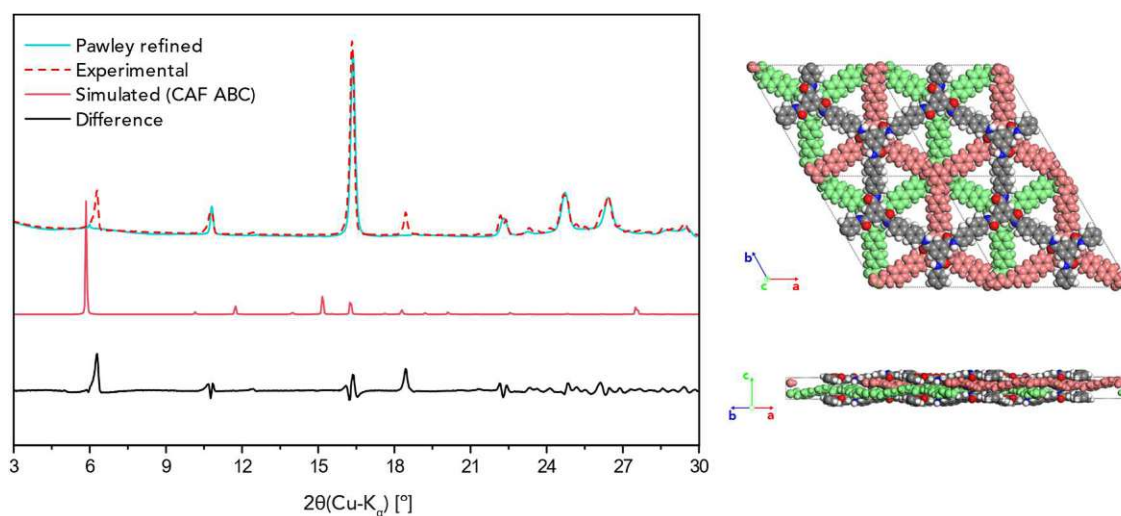
Figure 5.5: Pawley refined PXRD pattern and framework structure of ABC stacked CAF.

5.1.5 Sealed ampoule synthesis of PAM

Classically COF reactions are carried out in glass tubes which are then flame sealed after freeze-pump-thaw cycles (Figure 5.6). This is to maintain the pressure and ensure ideal stoichiometry, such that no other unwanted reactions like oxidation can occur during the long reaction time. Due to the inability to generate extended COF structures in autoclaves, an alternative approach was pursued by attempting the synthesis within sealed glass ampoules.

To an oven-dried 25 mL borosilicate glass tube, trimesic acid (42.03 mg, 0.2 mmol), benzidine (55.27 mg, 0.3 mmol) were added, followed by water (10 mL) along the walls of the tube (to push down any remaining solids remaining atop of the tube). The tube was sonicated at room temperature for 10min. The reaction mixture was then degassed through three freeze-pump-thaw cycles (vacuum <50 mTorr), after which the tube was flame sealed under vaccum. The ampoules were placed in a 1 L steel batch autoclave filled with 300 mL deionized water to maintain positive vapour pressure. The batch autoclave was heated to 200 °C, where it was held for t_R = 4 and 5 days. Afterwards, the ampoule was allowed to cool down to RT under ambient conditions. The ampoule was cracked open and the solids were isolated via filtration and washed with water (3 x 10 mL), ethanol (3 x 10 mL) and acetone (3 x 10 mL), then dried at 80 °C under vacuum yielding the product.

During the screening process, it was observed that the product obtained from the ampoule with t_R = 4 days was identical to that obtained from the autoclave. This similarity was evident from the lack of any alteration in the FT-IR spectra and PXRD results (Figure 5.7).

Figure 5.6: Flame sealing of glass tubes after freeze-pump-thaw cycles.
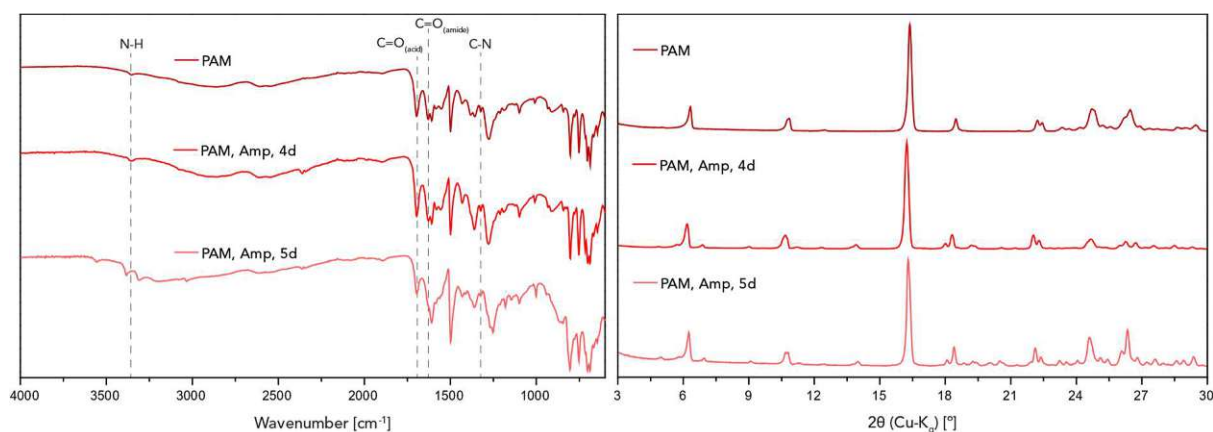
Figure 5.7: FT-IR spectra and PXRD pattern of PAM (AC, T_R= 200 °C, t_R= 4d); PAM (Ampoule, T_R= 200 °C, t_R= 4d; 5d)

5.1.6 Stability test for water synthesized PAMs

The chemical stability of each of the PAMs were checked by suspending it in 2 N HCl and 3 N NaOH at RT for 3 days. The PAMs were filtered and dried, later analysed by FT-IR spectroscopy and PXRD (Figure 5.8 & 5.9).
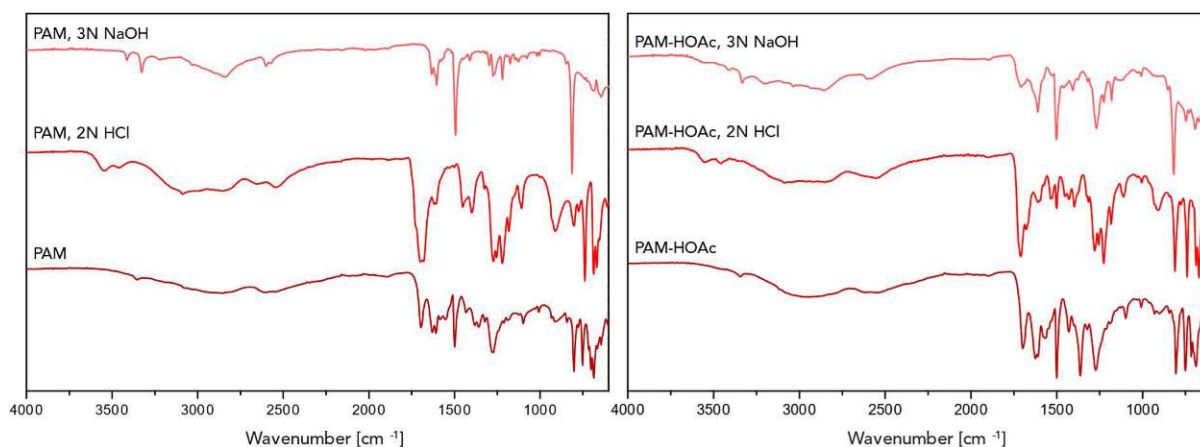
Figure 5.8: FT-IR spectra of PAM and PAM-HOAc (Pristine; in 2N HCl; in 3N NaOH)
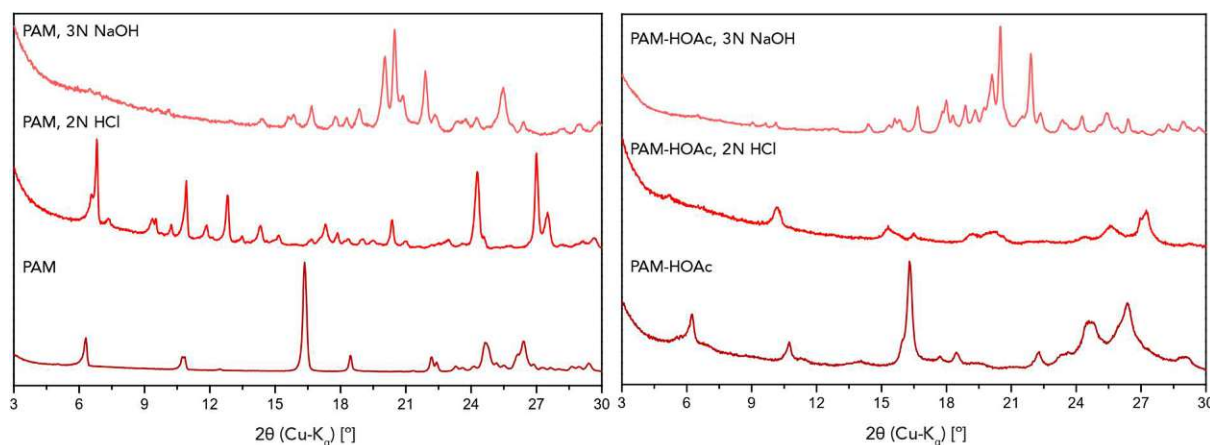
Figure 5.9: PXRD pattern of PAM and PAM-HOAc (Pristine; in 2N HCl; in 3N NaOH)

Both the FT-IR spectra and the PXRD pattern indicate that the suspended product appeared different when compared to the previous pristine PAMs (Figure 5.8 and 5.9). This means that the PAMs are not stable in acidic and basic conditions for longer periods.

The solubility of the synthesized PAMs in different mediums was investigated, and the findings are compiled in Table 5.2. It was noted that the prepared PAMs exhibited solubility in polar aprotic solvents. Our suspicion is that these aprotic solvents could potentially interfere with the interlayer interactions and disrupt the stacking, particularly considering our anticipation of ABC stacking, which inherently possesses a weaker structure. Additionally,

63

since it is suspected that the size of framework might be small enough to facilitate the formation of a solvate shell more easily.

Table 5.2: Solubility chart of PAMs

	H_2O	EtOH	Acetone	THF	DMF	DMSO	aq. NaOH	aq. HCl
PAM	X	X	X	Y	Y	Y	X	X
PAM-HOAc	X	X	X	Y	Y	Y	X	X

X = not soluble; Y =soluble

5.1.7 Supercritical carbon dioxide (scCO₂) activation of PAM

COFs are usually activated by washing with solvents followed by vacuum drying (90% of reported methods). It is anticipated that certain COFs could be prone to distortions, particularly during the vacuum and heat activation process. Drying with scCO₂ minimizes capillary strain and is the most effective method for activating porous materials,[124] though it requires specialized equipment. In this study, a scCO₂ extraction setup was employed to activate the products.

The final products were analysed via ATR-FTIR spectroscopy and PXRD. The results were compared with pristine PAMs to ascertain whether this process yielded a crystalline framework. In both the FT-IR spectra and the PXRD pattern, the activated product exhibited identical characteristics to the previous state. This implies that there were almost no changes, both in terms of chemical composition and structural features.
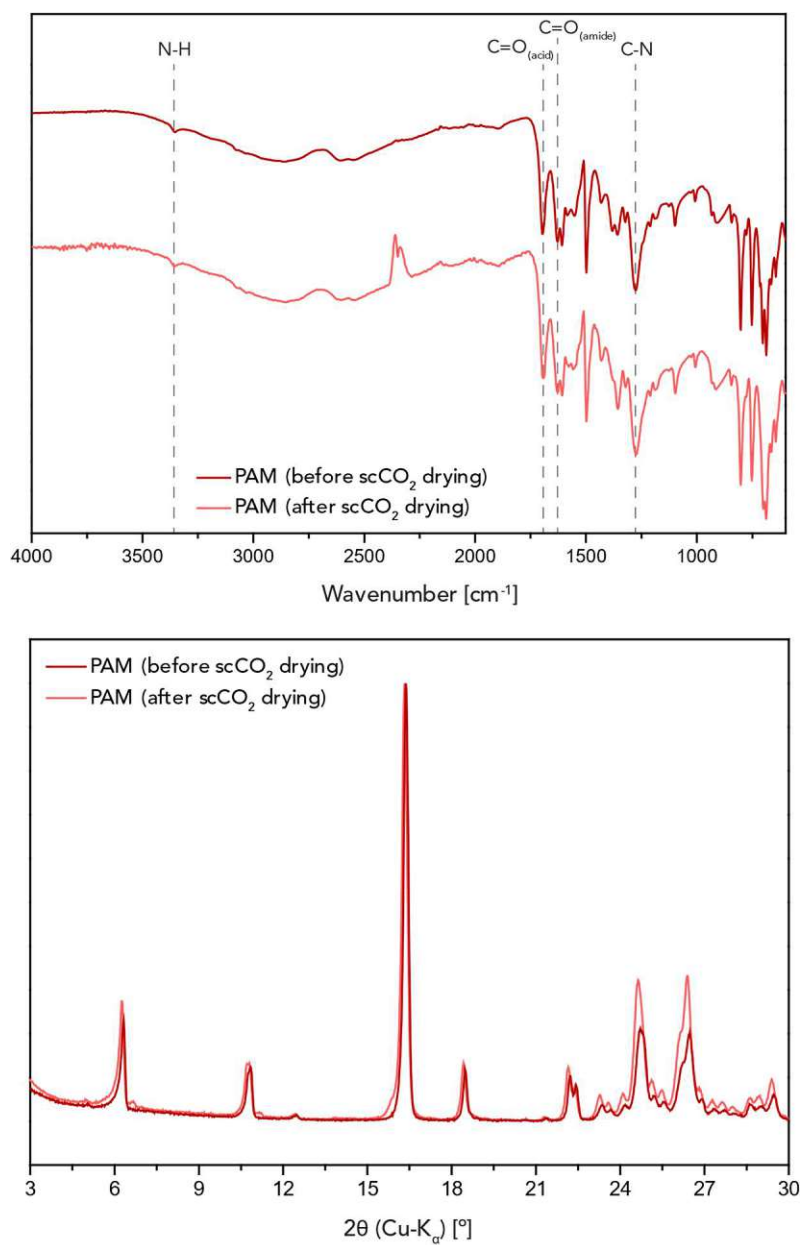
Figure 5.10: FT-IR spectra and PXRD pattern of PAM (Pristine and after scCO$_2$ drying)

5.2 Hydrothermal synthesis of crystalline benzimidazole-linked organic materials

5.2.1 Hydrothermal synthesis of PBIM and PBIM-HOAc

Hydrothermal synthesis of PBIM

A glass liner was charged with trimesic acid (42.03 mg, 0.2 mmol), 3,3'-Diaminobenzidine (64.28 mg, 0.3 mmol) and water (5 mL). The mixture was sonicated for 5 min at room temperature (RT). The tube was placed in a Teflon liner and sealed in a steel autoclave. The autoclave was kept in a oven preheated to 200 °C, where it was held for t_R = 18 h to 6 days. Afterwards, the autoclave was allowed to cool down to RT under ambient conditions. The autoclave was opened and the solid was isolated via filtration and washed with water (3 x 10 mL), ethanol (3 x 10 mL) and acetone (3 x 10 mL), then dried at 80 °C under vacuum yielding PBIM.

Hydrothermal synthesis of PBIM-HOAc

PBIM-HOAc was synthesised according to the similar experimental polymerisation procedure to that explained above, except that to the reaction mixture 6M HOAc (0.3 mL) was added after sonication. The product was washed and dried at 80°C under vacuum yielding PBIM-HOAc.

Both batches, PBIM and PBIM-HOAc, were screened at various t_R ranging from 18 h to 6 days, to identify the optimum reaction conditions (summarized in Table 5.3). The products were analysed with ATR-FTIR spectroscopy and PXRD to confirm chemical connectivity and crystallinity.

Table 5.3: Screening for optimum t_R and T_R

Precursors (ratio in mmol)	AcOH (mL)	H₂O (mL)	Reactor	T_R (°C)	t_R
TmA:DABz (0.2:0.3)	-	5	Autoclave	200	18h
TmA:DABz (0.2:0.3)	0.3	5	Autoclave	200	18h
TmA:DABz (0.2:0.3)	-	5	Autoclave	200	1d
TmA:DABz (0.2:0.3)	0.3	5	Autoclave	200	1d
TmA:DABz (0.2:0.3)	-	5	Autoclave	200	2d
TmA:DABz (0.2:0.3)	0.3	5	Autoclave	200	2d
TmA:DABz (0.2:0.3)	-	5	Autoclave	200	3d
TmA:DABz (0.2:0.3)	0.3	5	Autoclave	200	3d
TmA:DABz (0.2:0.3)	-	5	Autoclave	200	4d
TmA:DABz (0.2:0.3)	0.3	5	Autoclave	200	4d
TmA:DABz (0.2:0.3)	-	5	Autoclave	200	6d
TmA:DABz (0.2:0.3)	0.3	5	Autoclave	200	6d

5.2.2 ATR-FTIR spectra

The progress of the reaction was monitored with ATR-FTIR spectroscopy (Figure 5.11) and the effect of modulators on the formation of the benzimidazole-linkage was also studied (Figure 5.12). It is evident that in PBIM-HOAc with time, the C=O band is getting gradually reduced and C=N band is gradually increasing. In PBIM there is an initial reduction of C=O band, but not much difference after t_R= 2 days. Even after prolonged reaction times (t_R= 6 days), there were still C=O stretching bands (~1700 cm^{-1}) in FT-IR spectra, confirming the presence of

peripheral -COOH groups in both batches. Moreover, several modes in the H-bonding region ($\sim$3400 cm^{-1} - 2800 cm^{-1}) further point at -COOH endgroups.
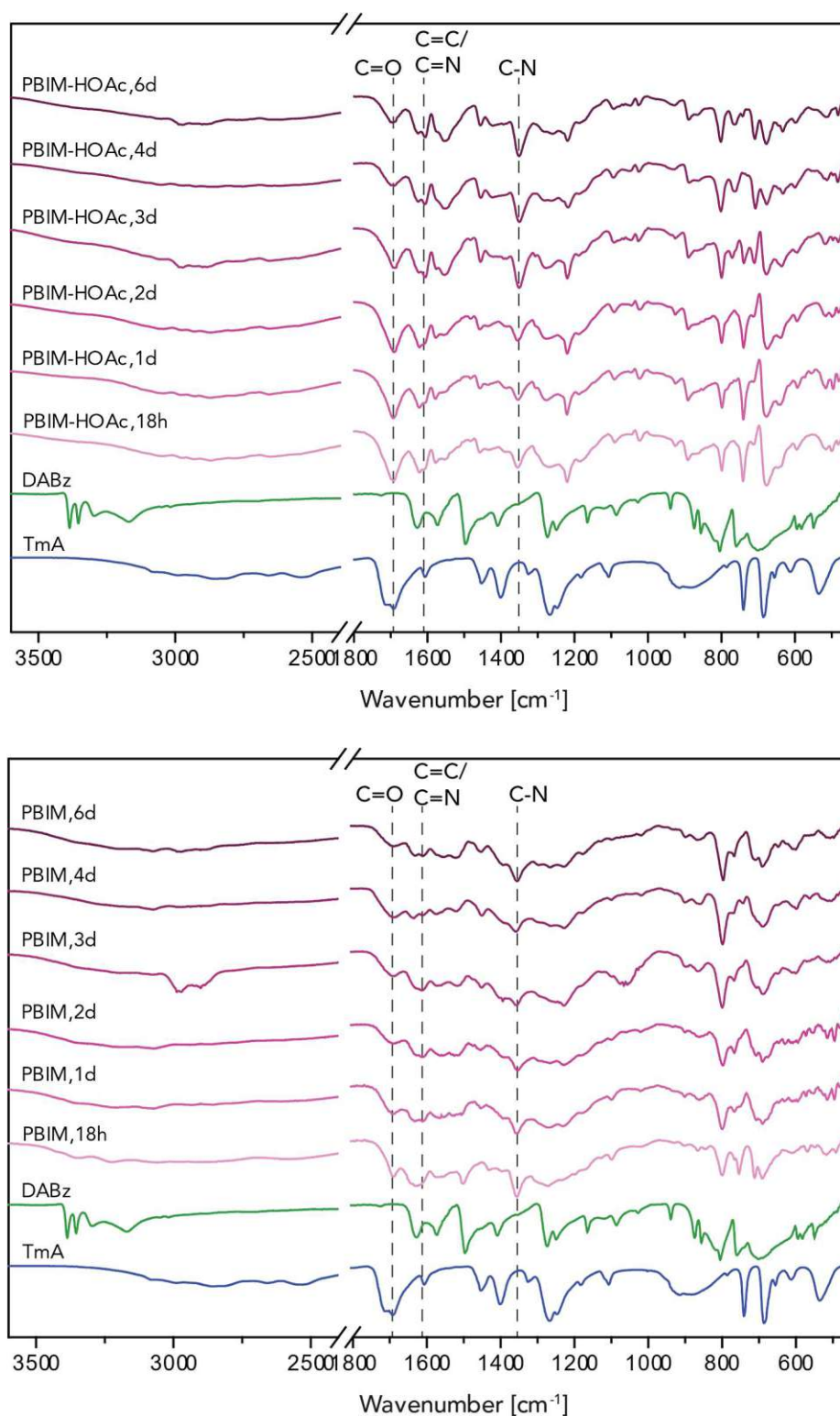
Figure 5.11: FT-IR spectra of TmA, DABz, PBIM-HOAc (AC, T_R= 200 °C, t_R= 18h, 1d, 2d, 3d, 4d, 6d) and PBIM (AC, T_R= 200 °C, t_R= 18h, 1d, 2d, 3d, 4d, 6d)
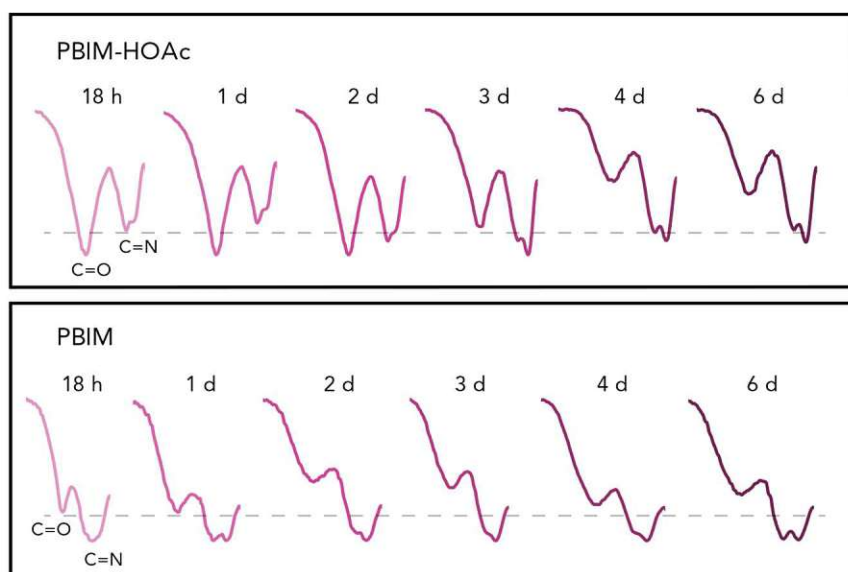
Figure 5.12: FT-IR spectra of PBIM-HOAc and PBIM showing the effect of modulator with respect to t_R.

5.2.3 PXRD analysis

The experimental PXRD patterns of the obtained solids from both batches were distinct (Figure 5.13). For PBIM-HOAC products, PXRD patterns did not yield any sharp peaks till t_R= 3 days. The sample at t_R= 3 days onwards exhibited extremely weak peaks, whereas the PXRD patterns of sample with t_R= 6 days showed notable crystallinity confirming the presence of framework-like structures. In addition, these observations implied that the formation of crystalline PBI is slow. Moreover, employing modulators is improving the crystallinity of the framework.

For PBIM products, sharp peaks hinting crystallinity was seen from t_R= 18 h to 3 days, but these were due to low molecular weight crystalline PBI products, none of the PXRD patterns were indicative of an extended framework structure.
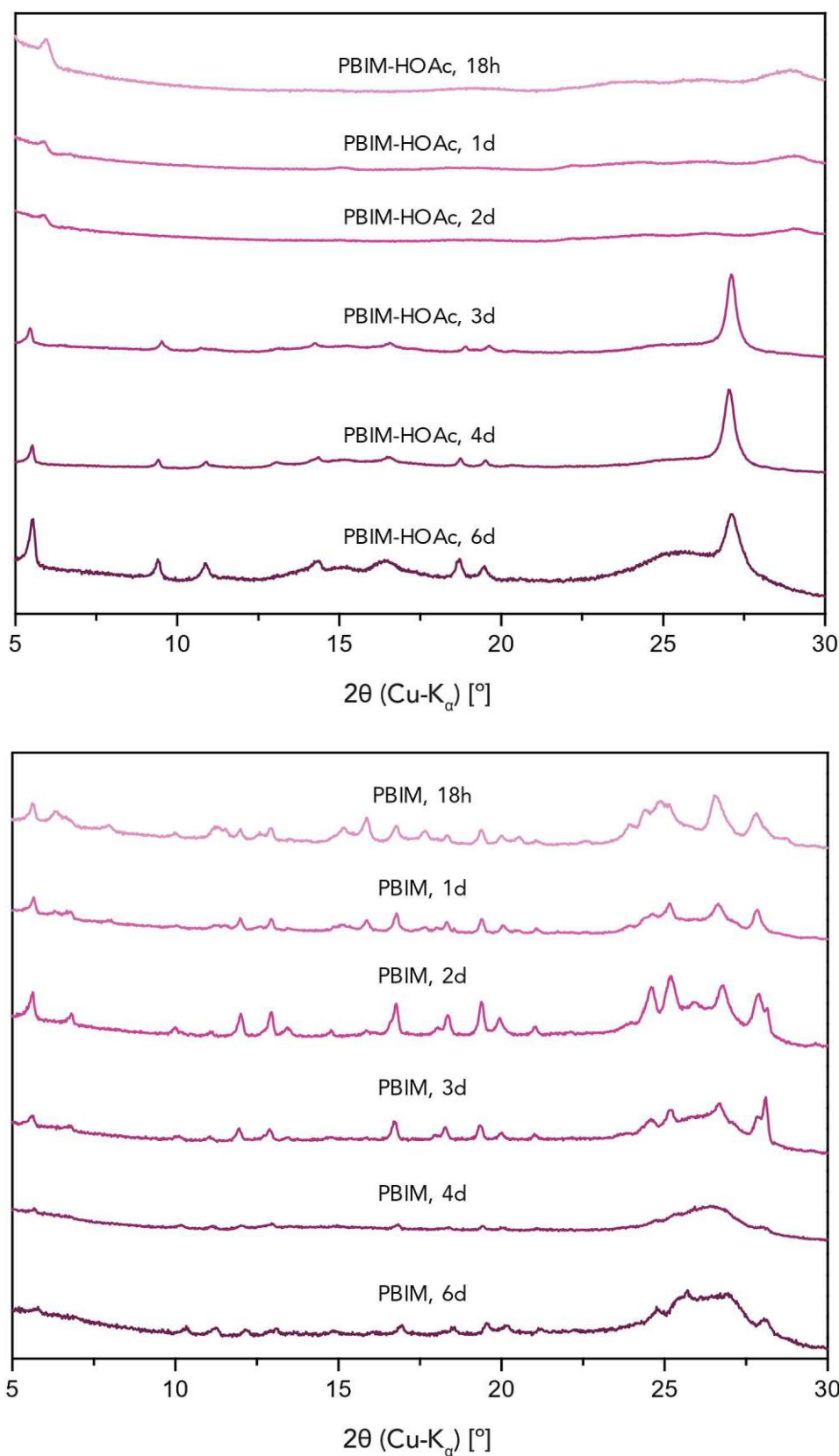
Figure 5.13: PXRD patterns of PBIM-HOAc (AC, T_R= 200 °C, t_R= 18h, 1d, 2d, 3d, 4d, 6d) and PBIM (AC, T_R= 200 °C, t_R= 18h, 1d, 2d, 3d, 4d, 6d)

70

5.2.4 Structural modelling and PXRD simulations

To better understand the structure and to confirm whether a framework is formed, hypothetical frameworks were generated computationally using Materials Studio. Following geometric energy minimization, the simulated PXRD pattern was generated from these frameworks and subsequently compared with the experimental PXRD pattern (Figure 5.14). But none of the simulations were exactly matching the experimental PXRD results.
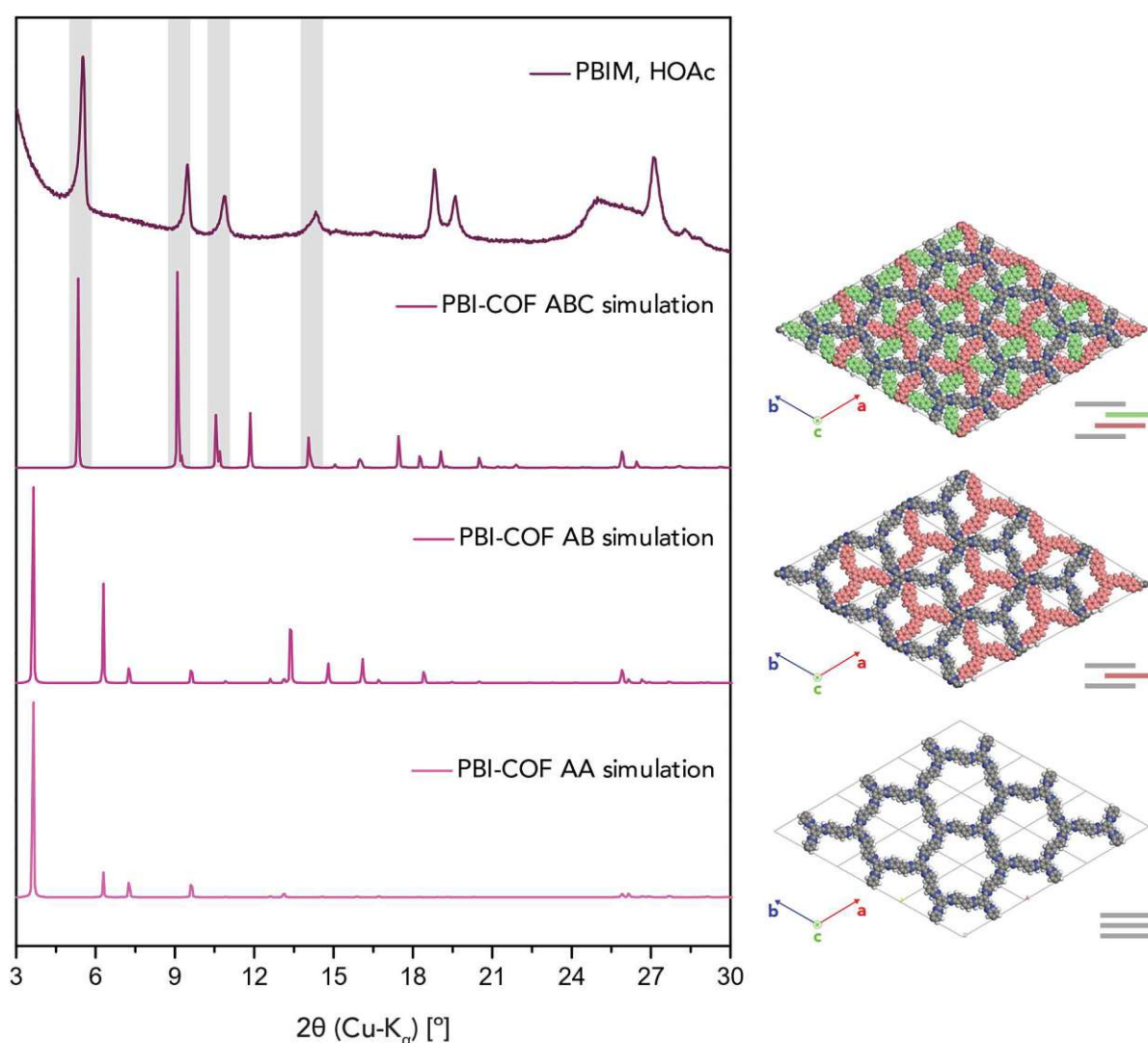
Figure 5.14: Comparison of PBIM-HOAc (AC, T_R= 200 °C, t_R= 6d) with simulated PXRD patterns of various stacking arrangements in PBI-COF

Since there were unreacted -COOH groups present in the material. There was a possibility of forming macrocycles similar to the previous PAMs. Optimized structures of potential macrocycles were also generated, and their simulated PXRD patterns were compared with the experimental PXRD pattern. However, the comparison did not result in a match.

5.2.5 Gas sorption isotherm

To investigate the permanent porosities of the PBIM-HOAc, nitrogen gas (N_2) sorption isotherm data was collected at 77 K (Figure 5.15). It exhibited classic type-IV isotherms characterized by a hysterisis loop, which is seen in mesoporous materials.[125] Based on the obtained N_2 uptake isotherm data, the surface area of PBIM-HOAc was calculated from Brunauer-Emmett-Teller (BET) model was estimated to be 34 m^2/g and the total pore volume was also determined to be 0.081 cm^3/g at P/P_0=0.99, which shows a very low porosity. The results suggest that either the pores of the material are blocked or it is having a collapsed framework. Due to the inadequate quality of the data, pore size distributions (PSDs) could not be obtained.

When the measured isotherm data is compared to the range anticipated for a typical mesoporous material, it becomes evident that the material exhibits a low N_2 uptake. Although an adsorption process is observable at high relative pressure, but this could not really due to framework pores. A typical type IV isotherm would probably have a delayed desorption, with a characteristic plateau at high relative pressures. The adsorption process seen here could be due to N_2 getting adsorbed in between particulates. Probably the sample is composed of very small particles whose packing leaves some mesoporous voids. From what we evaluated from the sample, those voids should be bigger than 100 Å. This confirms that there are no structural pores and that N_2 is not the best probe to evaluate such a pore population.
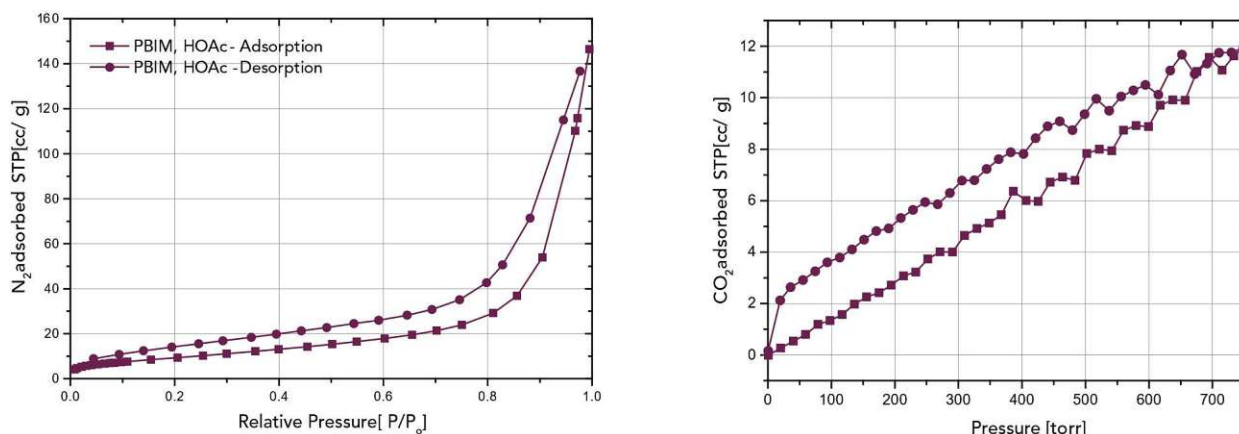
Figure 5.15: Low pressure N_2 sorption isotherm collected at 77 K and CO_2 sorption isotherm collected at 195 K

A CO_2 adsorption study was conducted to further validate earlier observations. Similarly, in this analysis, it was observed that the gaseous uptake by the material is very low, pointing towards lack of structural pores that would be present in a framework.

Therefore, it can be concluded that the material exhibits low porosity, suggesting an absence of extended frameworks in its structure. Instead, it seems to be composed of only a few macrocycle-long products. The presence of numerous reflections in the high two-theta regions in PXRD pattern would tend to support this notion.

5.2.6 High-resolution XPS spectra

The chemical environment of the products was further checked by XPS spectrum. The high-resolution scan for C1s (Figure 5.16a) was deconvoluted into three sub-peaks at C=C/C-C at 284.8 eV, C-N at 286.0-286.5 eV and O-C=O at 288.5-289.5 eV. While changes in the relative content of C-C and the C-N signal are small after heat treatment, but the O-C=O signal is reduced after the heat treatment for both batches, indicating the selective removal of peripheral carboxyl groups. The high resolution N1s spectrum (Figure 5.16b) was deconvoluted into two sub-peaks, C=N-C at 398.8 eV and C-NH-C at 400.7 eV, accompanying with the formation of

the imidazole linkage. The O1s signal can be deconvoluted into two components C=O at lower and C-O at higher BE (Figure 5.16c). Changes in the O1s signal after annealing are difficult to evidence due to the two peaks being close in BE.
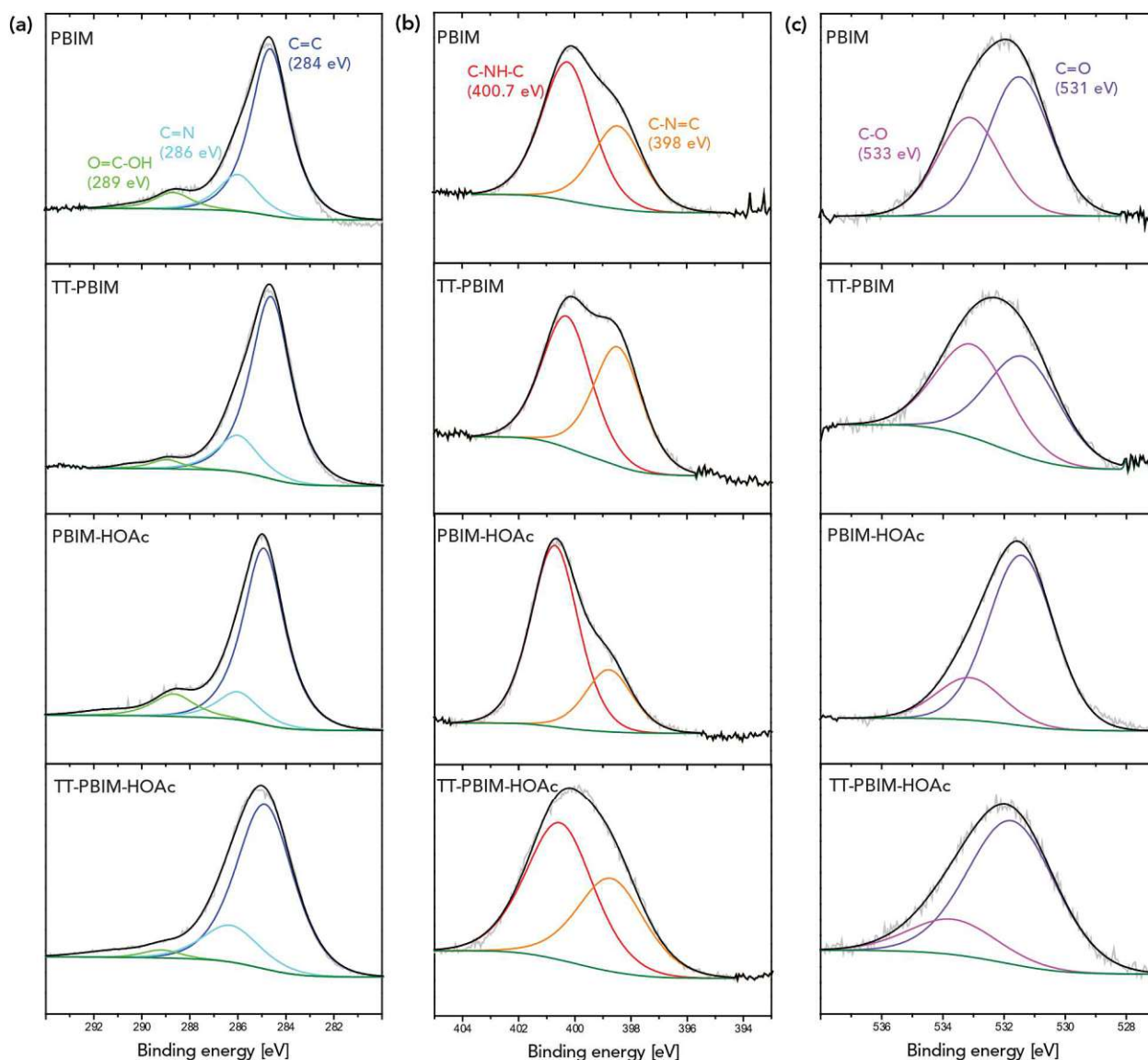
Figure 5.16: High-resolution XPS spectra of a) C1s; b) N1s; c) O1s

As indicated by the relative elemental composition summarized in Table 5.4 obtained from XPS, the oxygen content of thermally treated PBIMs were significantly lower than that of pristine PBIMs, due to elimination of carboxyl groups. However, the oxygen content in

thermally treated PBIMs did not reach zero, due to oxygen and moisture physically adsorbed to the pores of hygroscopic PBIMs, as observed in TGA results.

Table 5.4: Relative elemental composition

	Element/at%		
	C	N	O
PBIM	76.0	9.5	14.5
TT-PBIM	80.6	12.3	7.2
PBIM-HOAc	73.7	11.0	15.0
TT-PBIM-HOAc	80.7	11.9	7.3

5.2.7 Imine-exchange strategy with o-phenylene diamine

The critical step in the crystallization of COF is the establishment of conditions which allow the covalent linkage (imidazole in this case) between the building blocks to be reversible, yet slow enough for efficient self-correction of defects. In a typical COF synthesis, the formation of amorphous solid is initially observed, and over time this material transforms into a crystalline phase through a self-error-correction mechanism. Thus, immediate precipitation causes the COF solid to be invariably amorphous rather than crystalline. The aim was to enhance the reversibility of the reaction through the utilization of the imine-exchange strategy. The idea was to add excess of o-phenylene diamine (OPDA) to the reaction mixture, where OPDA functions as an inhibitor (Figure 5.17). In the presence of OPDA, the initial imidazole formation could be comparably fast; followed by a slow imine-exchange thus inhibiting rapid crystallisation/precipitation. This enables the slow growth of crystalline COFs, giving it enough time for self-error-correction and resulting in a long ranged ordered COF.
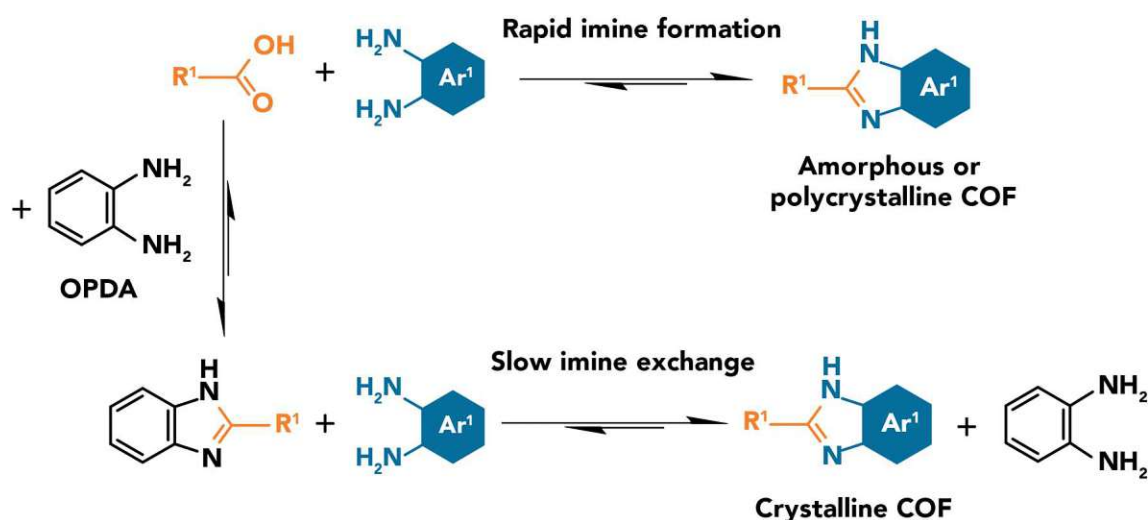
Figure 5.17: Rapid imine formation without OPDA and slow imine exchange in presence of OPDA.

Some HTP were carried out in presence of OPDA (0.2mmol/1eq, 0.6mmol/3eq), the products were characterised and analysed with FT-IR and PXRD (Figure 5.18). FT-IR spectra of all the products look identical, suggesting no changes in linkage chemistry. Based on PXRD analysis, it seems like there was not much improvement with the inhibitor as compared to the reaction conducted without it, especially in the small angle region. When adding excess of OPDA (>10eq), no polymer/ framework was formed and the product seems to be decomposed.
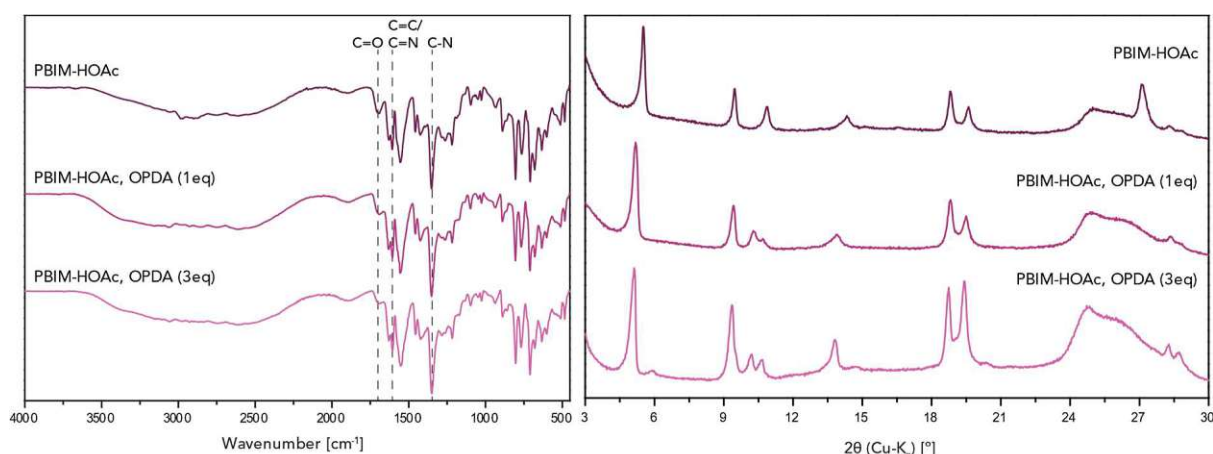
Figure 5.18: FT-IR spectra and PXRD patterns of PBIM-HOAc (AC, T_R= 200 °C, t_R= 6d) and PBIM-HOAc synthesized with OPDA (AC, T_R= 200 °C, t_R= 6d)

5.2.8 Sealed ampoules synthesis of PBIM

Typical HTP are carried out in non-stirred steel autoclaves or "Steel bombs". These are closed steel vessels, capable of withstanding high temperature and pressures which are generated in the hydrothermal regime (180-300 °C). But it cannot be evacuated completely and sometimes the presence of O_2 inside could lead to unwanted reactions. To circumvent this issue, some reactions were conducted in sealed glass ampoules that had been evacuated through freeze-pump-thaw cycles. The ampoules, charged with reagents, were placed in a 1 L steel batch autoclave filled with 300 mL deionized water to maintain positive vapour pressure. The batch autoclave was heated to 200 °C, where it was held for t_R = 3 days.

During the screening process, it was observed that the PBIM-HOAc obtained from the ampoule with t_R = 3 days was identical to that obtained from the autoclave (t_R = 6 days). This similarity was evident from the FT-IR spectra and XRD results (Figure 5.19). Therefore, reaction time of PBIM-HOAc can be reduced with sealed ampoule reactor.
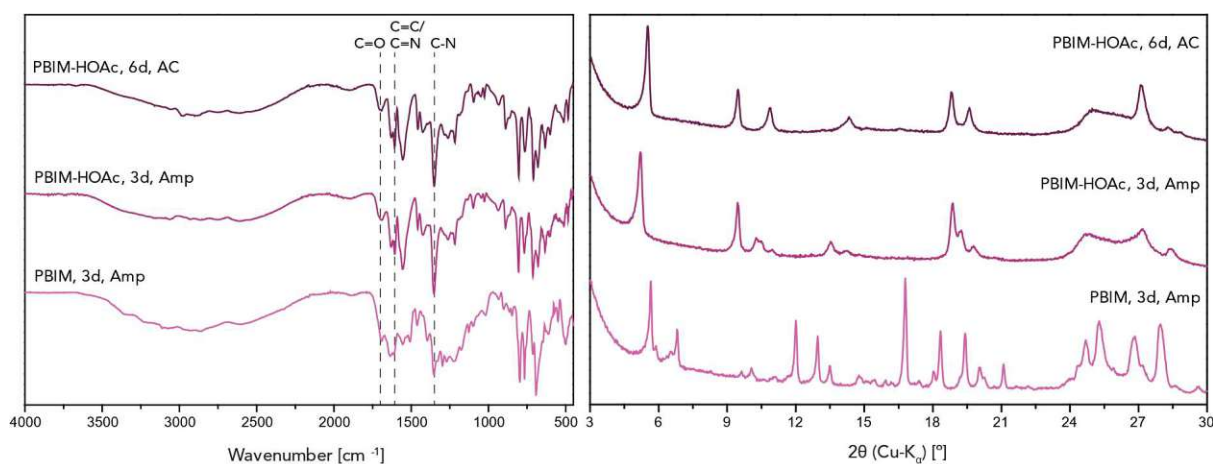
Figure 5.19: FT-IR spectra and PXRD patterns of PBIM-HOAc (AC, T_R= 200 °C, t_R= 6d); PBIM-HOAc synthesized in ampoule (Amp, T_R= 200 °C, t_R= 3d); PBIM synthesized in ampoule (Amp, T_R= 200 °C, t_R= 3d)

5.2.9 Super critical carbon dioxide (scCO₂) activation of PBIMs

Two methods were employed for scCO$_2$ activation of the products -

1. Pure scCO$_2$, 2mL/min, 100bar, 60°C, 2hours

2. scCO$_2$+10% EtOH, 2mL/min, 100bar, 60°C, 1hours followed by Pure scCO$_2$, 2mL/min, 100bar, 60°C, 1hours

The final products were analyzed via ATR-FTIR spectroscopy and PXRD (Figure 5.20). The results were compared with pristine PBIM-HOAc. From the FT-IR spectra the product looks identical as previous suggesting no changes in linkage chemistry. The final PXRD pattern looks completely different to the pristine product suggesting change in crystal structure, but not showing a framework pattern.
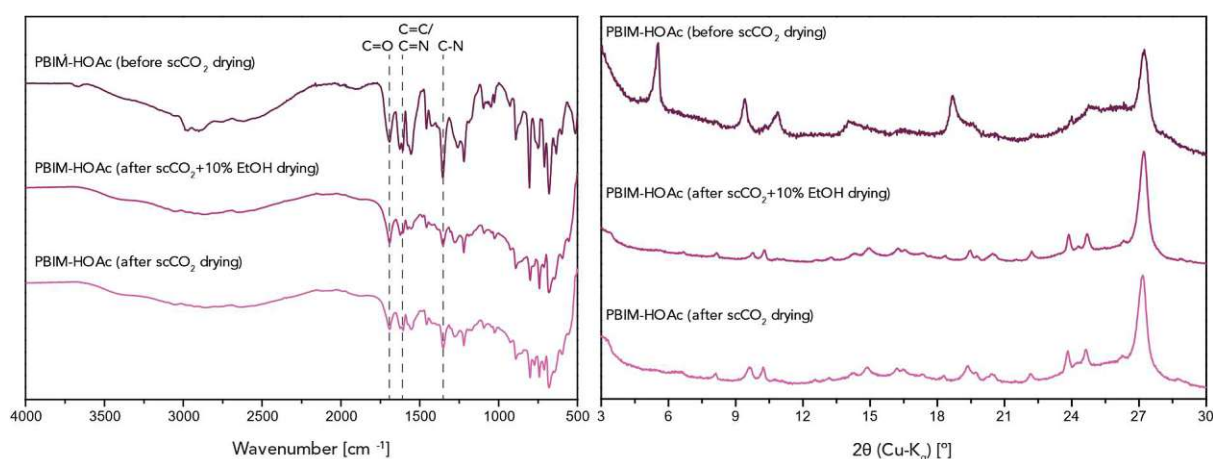
Figure 5.20: FT-IR spectra and PXRD pattern of PBIM (Pristine; scCO$_2$+10% EtOH drying; scCO$_2$ drying)

5.3 Hydrothermal synthesis of polybenzimidazoles and their conversion into polypyrrolones

5.3.1 Synthesis

MW-assisted hydrothermal synthesis of PBI-CO
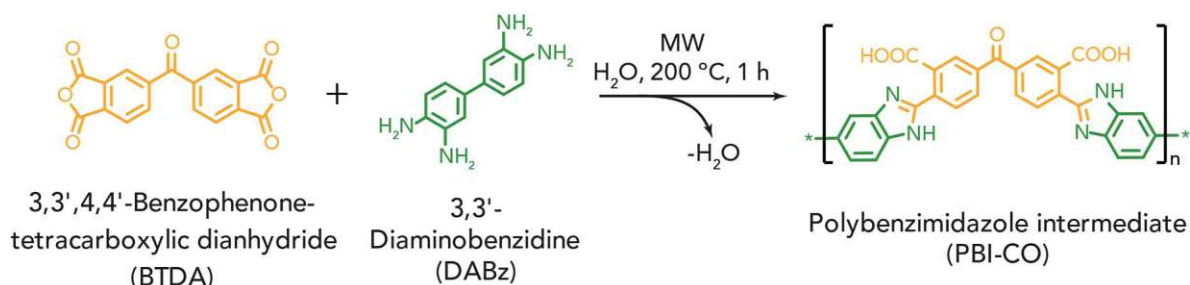
Scheme 5.1: MW-assisted HT synthesis of PBI-CO from BTDA and DABz

A MW glass liner was charged with 3,3′,4,4′-Benzophenonetetracarboxylic dianhydride (BTDA) (40.28 mg, 0.125 mmol), 3,3'-Diaminobenzidine (DABz) (26.78 mg, 0.125 mmol) and water (4 mL). The reactants were stirred properly at RT, followed by heating via MW irradiation to the desired reaction temperature (T_R) of 200 °C as fast as possible within a heating time (t_H) of 1-2 min. T_R was kept constant for a reaction time (t_R) of 1 h with constant stirring. After cooling back to RT, the resultant product contained two different distinct layers: a solid, coloured (~brown) sediment at the bottom and a translucent, liquid supernatant. The products were isolated via filtration, washed with water (3 x 10 mL), ethanol (3 x 10 mL) and acetone (3 x 10 mL), then dried at 80°C under vacuum.

Thermal annealing of PBI-CO

Scheme 5.2: Thermal annealing of PBI-CO to yield PPy-CO

Thermal curing programme (under N_2): Heat from RT to 150 °C (10 K/min) → hold for 30 min → heat to 230 °C (10 K/min) → hold for 30 min → heat to 310 °C (10 K/min) → hold for 90 min

MW-assisted hydrothermal synthesis of PBI-6F
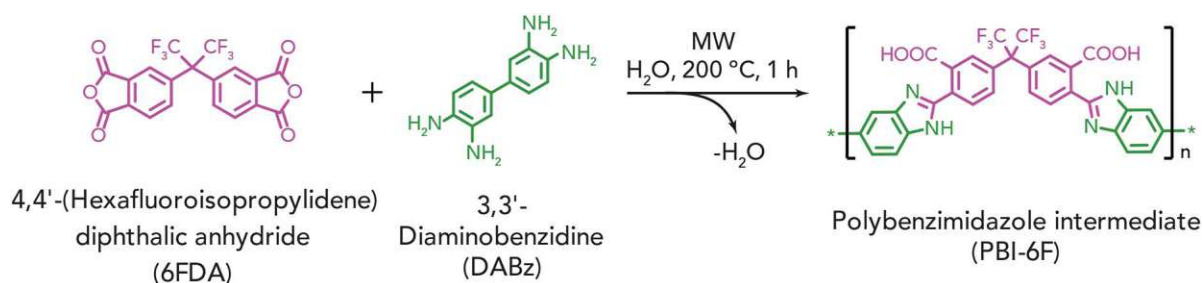
Scheme 5.3: MW-assisted HT synthesis of PBI-6F from 6FDA and DABz

A MW glass liner was charged with 4,4-(Hexafluoroisopropylidene) diphthalic anhydride (6FDA) (55.53 mg, 0.125 mmol), 3,3'-Diaminobenzidine (DABz) (26.78 mg, 0.125 mmol) and water (4 mL). The reactants were stirred properly at RT, followed by heating via MW irradiation to the desired reaction temperature (T_R) of 200 °C as fast as possible within a heating time (t_H) of 1-2 min. T_R was kept constant for a reaction time (t_R) of 1 h with constant stirring.

After cooling back to RT, the resultant product contained two different distinct layers: a solid, coloured (~brown) sediment at the bottom and a translucent, liquid supernatant. The products were isolated via filtration, washed with water (3 x 10 mL), ethanol (3 x 10 mL) and acetone (3 x 10 mL), then dried at 80°C under vacuum.

Thermal annealing of PBI-6F

Scheme 5.4: Thermal annealing of PBI-6F to yield PPy-6F

Thermal curing programme (under N_2): Heat from RT to 150 °C (10 K/min) → hold for 30 min → heat to 230 °C (10 K/min) → hold for 30 min → heat to 310 °C (10 K/min) → hold for 90 min

5.3.2 Structural modelling

Space-filling models of the polymeric segments provide an accurate depiction of individual chains whereby the relative degree of segmental mobility can be seen (Figure 5.21). Molecular modeling simulations were completed using Gaussian09 software. Multiple iterations of geometry minimization were used to calculate the relative lowest energy conformations of single-chain PPy-CO and PPy-6F using B3LYP theory of calculation and 6-31G* basis set. As expected, semi-segmental mobility exists within the polymeric backbone due to the specific

monomers used. The PPy6F model in Figure 5.22 is more kinked than the PPy-CO model due to 6FDA fraction, which possesses the sp3 carbon atom.
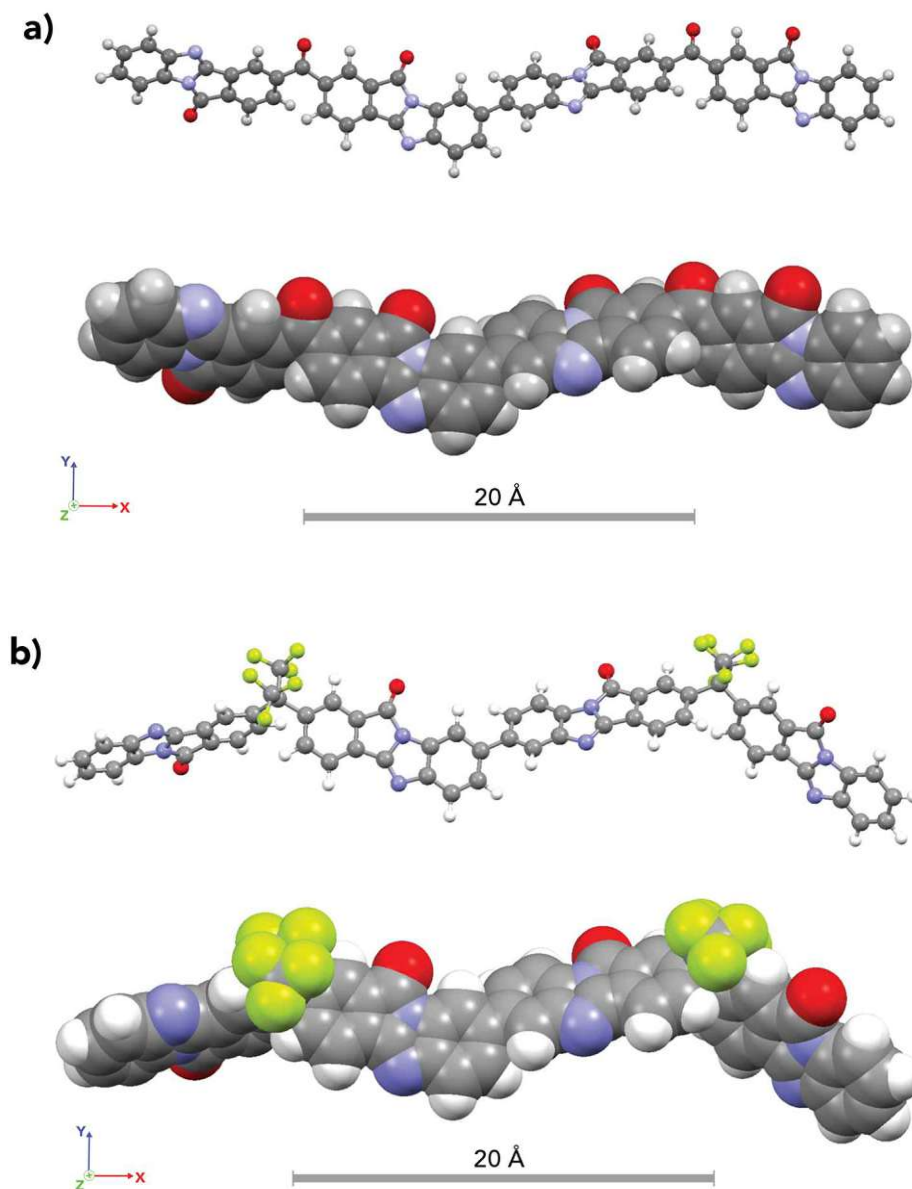
Figure 5.21: Ball-stick representation and space-filling representation of a) PPy-CO and b) PPy-6F polymeric segments

5.3.3 Morphology and solubility

The morphology of all the prepared PBI-intermediates and PPys were similar and were mostly spherical agglomerates (~2-5 μm in diameter) under scanning electron microscope

(SEM) (Figure 5.23). Thus, during thermal annealing, PBI-intermediates undergo no melting or softening, suggesting a solely solid-state conversion to PPy. Also, the images of the PBI-intermediate indicate that the MW-assisted HT synthesis follows a mechanism of polymerisation that is similar to that of suspensions. It seems that the insoluble monomers aggregate into small droplets in water due to the stirring, and the polymerisation is carried out in these droplets. During the polymerisation, these immiscible droplets slowly convert into rigid, solid particles when reaching sufficient high molecular weight. It can be considered as a form of bulk polymerization but on a much smaller scale.

The solubility of the prepared polymers in various solvents was investigated (summarised in Table 5.5). It was observed that, upon mixing the PPy polymer in polar aprotic solvents, the spherical particles that make up the PPys formed a fine dispersion. This could be exploited to improve the processability of the polymers.

Table 5.5: Solubility chart of PBI-intermediates and PPys

	H_2O	EtOH	Acetone	THF	DMF	DMSO
PBI-CO	X	X	X	X	~	~
PPy-CO	X	X	X	X	X	X
PBI-6F	X	X	X	~	~	~
PPy-6F	X	X	X	~	~	~

X = not soluble; Y =soluble; ~ =dispersion
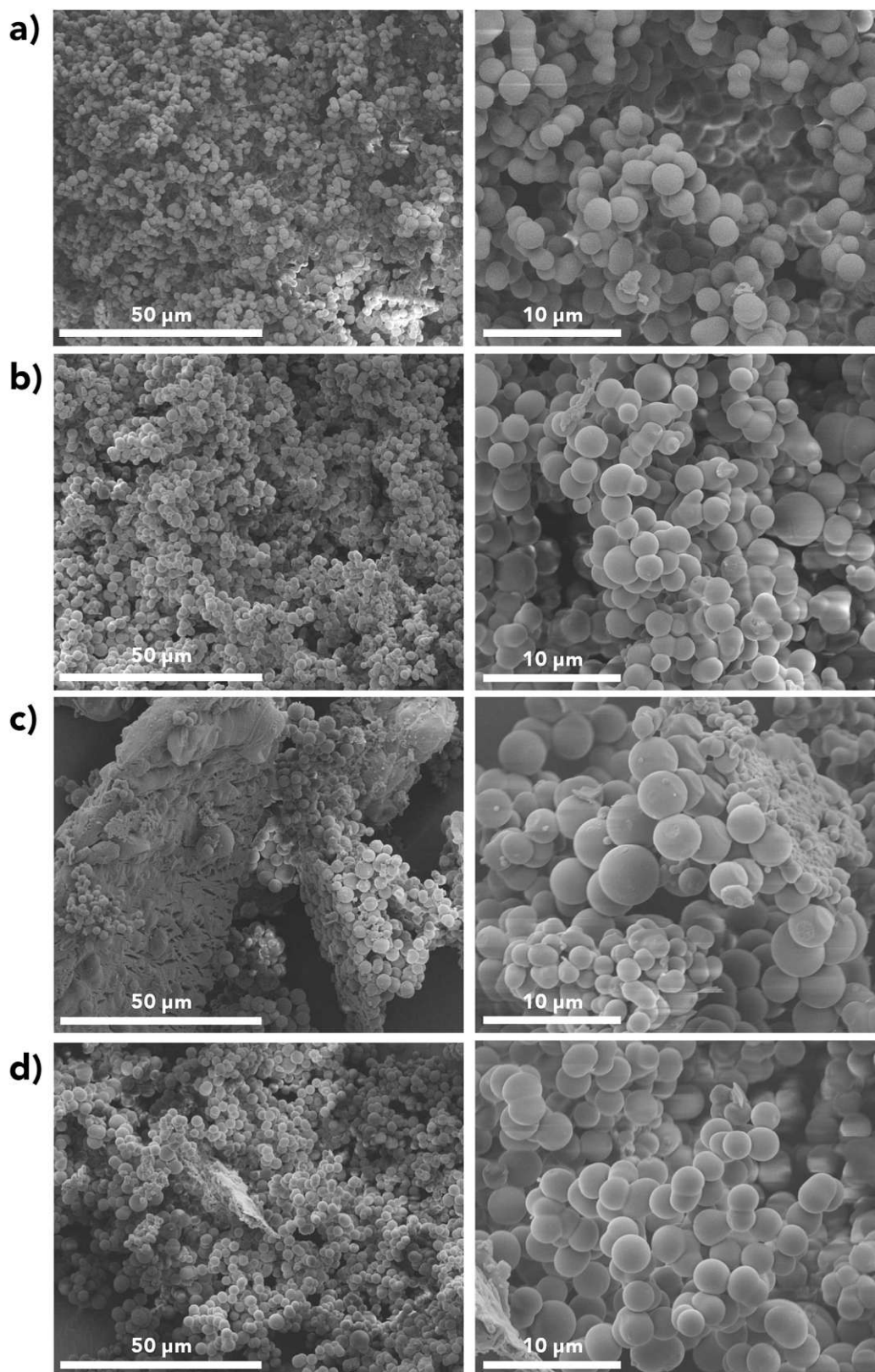
Figure 5.22: SEM pictures of a) PBI-CO b) PPy-CO c) PBI-6F d) PPy-6F

5.3.4 Alternate synthesis route via non-stirred autoclave

A glass liner was charged with respective carboxylic anhydride monomer (0.25mmol) (BTDA= 80.55 mg; 6FDA= 111.06 mg), 3,3'-Diaminobenzidine (DABz) (53.57 mg, 0.25 mmol) and water (10 mL). The mixture was sonicated for 2 min at RT, the glass liner was placed inside a Teflon liner and sealed in a steel autoclave. The autoclave was kept in an oven preheated to temperature (T_R) of 200 °C. After cooling back to RT, the products were isolated via filtration, washed with water (3 x 10 mL), ethanol (3 x 10 mL) and acetone (3 x 10 mL), then dried at 80°C under vacuum.

The final products were analyzed via ATR-FTIR spectroscopy (Figure 5.23 & 5.24) and PXRD (Figure 5.25 & 5.26).

Table 5.6: Screening for optimum t_R and T_R

Sample	Precursors (ratio in mmol)	H_2O (mL)	Reactor	T_R (°C)	t_R
	BTDA:DABz (0.25:0.25)	10	-	RT	-
	BTDA:DABz (0.25:0.25)	10	Autoclave	200	1d
PBI-CO, AC	BTDA:DABz (0.25:0.25)	10	Autoclave	200	3d
	BTDA:DABz (0.25:0.25)	10	Autoclave	200	5d
	6FDA:DABz (0.25:0.25)	10	-	RT	-
	6FDA:DABz (0.25:0.25)	10	Autoclave	200	1d
PBI-6F, AC	6FDA:DABz (0.25:0.25)	10	Autoclave	200	3d
	6FDA:DABz (0.25:0.25)	10	Autoclave	200	5d
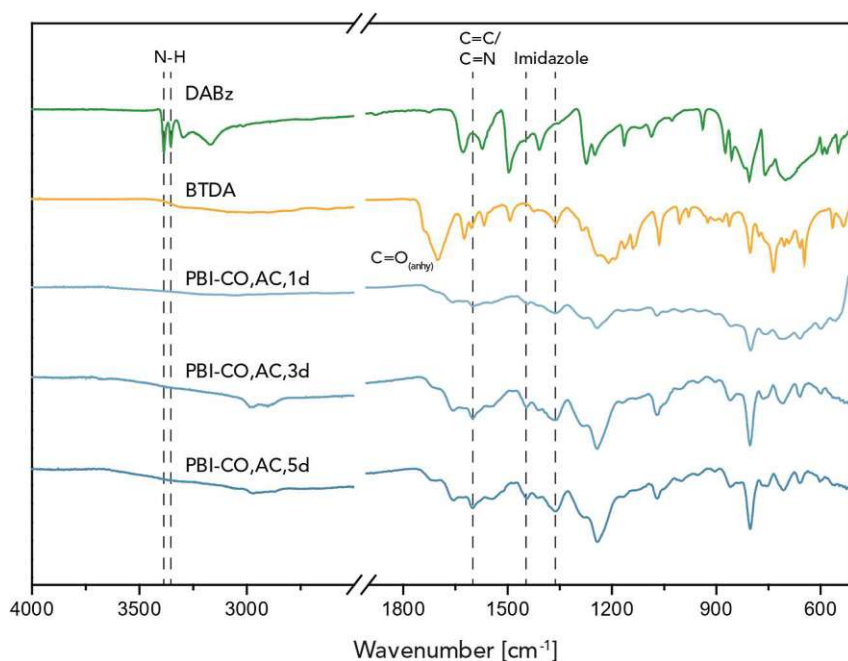
Figure 5.23: FT-IR spectra of DABz, BTDA, PBI-CO (AC, T_R= 200 °C, t_R= 1d; 3d; 6d)
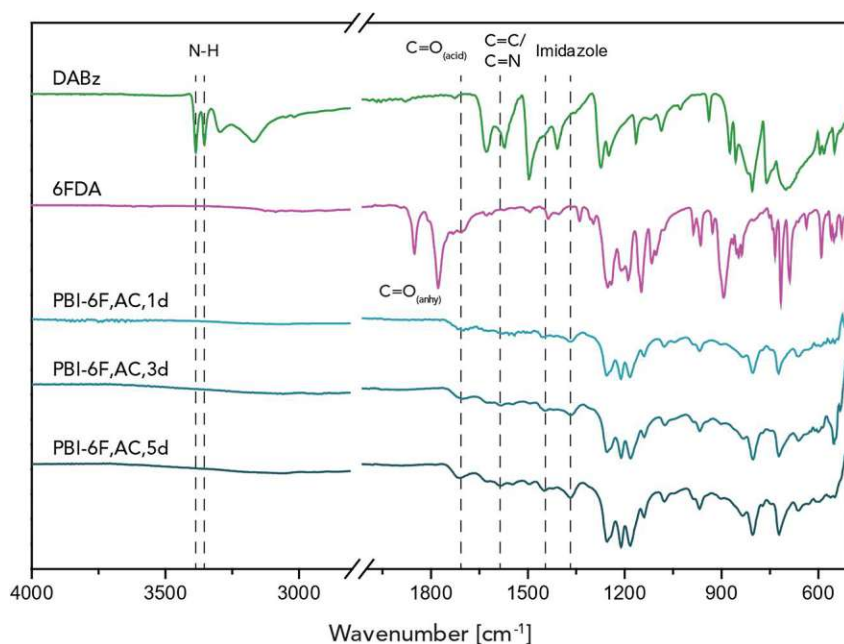
Figure 5.24: FT-IR spectra of DABz, 6FDA, PBI-6F (AC, T_R= 200 °C, t_R= 1d; 3d; 6d)

From screening the reaction conditions (summarized in Table 5.7), the optimal t_R was found to be of 3 days via analyzing the FT-IR (Figure 5.24 & 5.25) and PXRD (Figure 5.26 & 5.27) results. ATR-FTIR spectra and PXRD pattern of the products were identical to the batch prepared in MW reactor, thus confirming a successful formation of PBI-intermediate polymers.
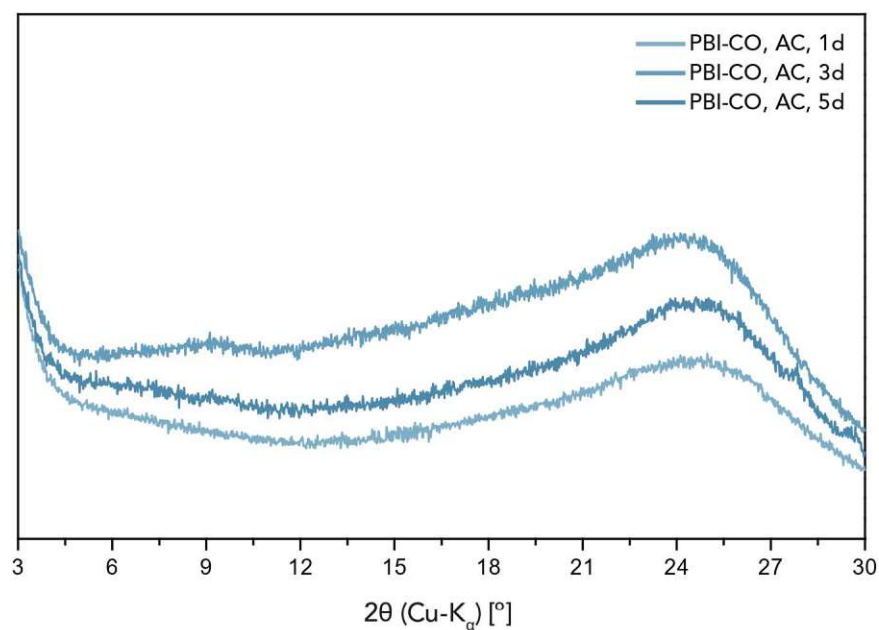
Figure 5.25: PXRD pattern of PBI-CO (AC, T_R= 200 °C, t_R= 1d; 3d; 6d)
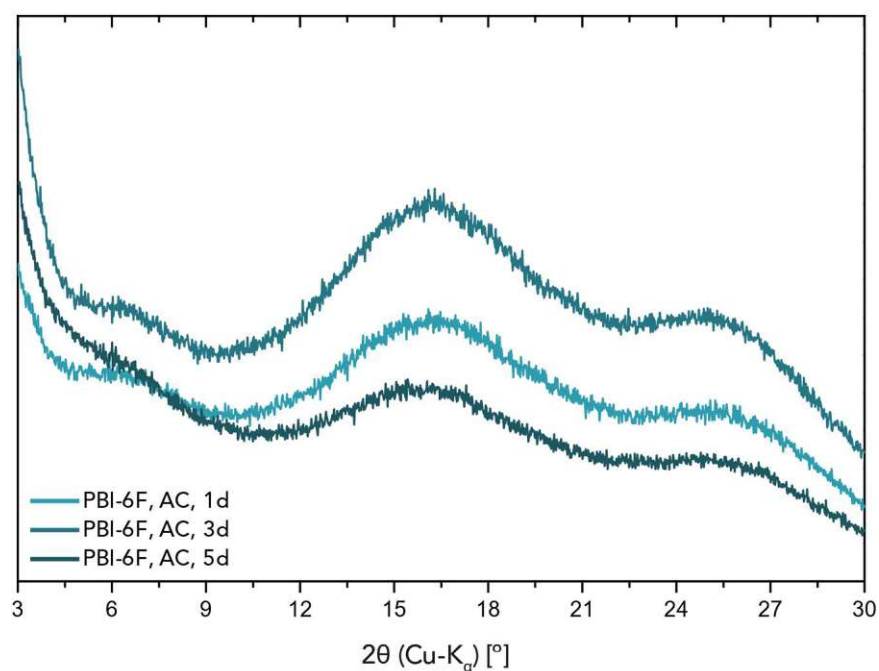
Figure 5.26: PXRD pattern of PBI-6F (AC, T_R= 200 °C, t_R= 1d; 3d; 6d)

The PXRD patterns revealed that the PBI-intermediates generated in autoclaves remained amorphous, despite the anticipation of increased crystallinity through bond reversibility or

87

devitrification at higher t_R. The PBI intermediate products were subjected to thermal annealing at 310 °C under N_2 to yield respective PPy products. It was observed that the PPy products obtained was identical to that obtained from the MW batch. This similarity was evident from the lack of any alteration in the FT-IR spectra and PXRD results (Figure 5.27 & 5.28).
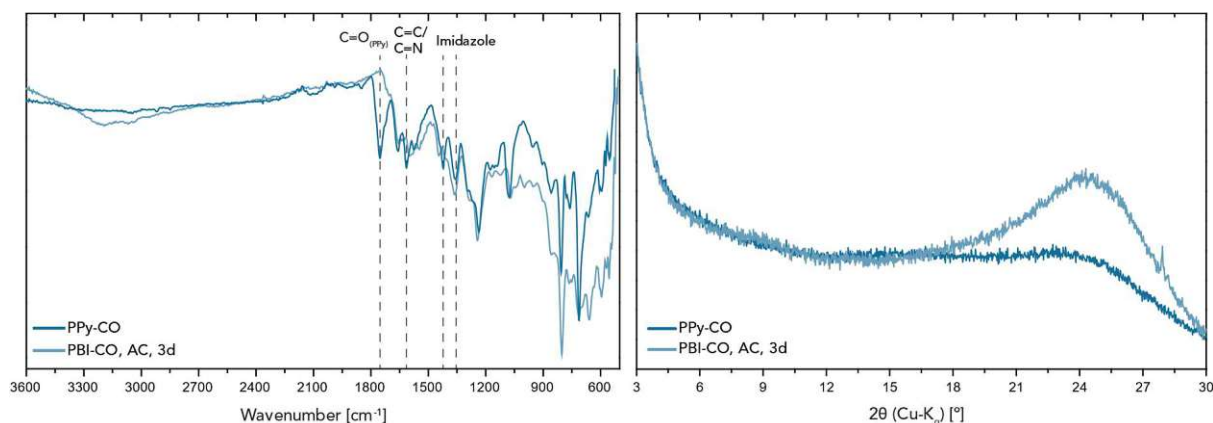
Figure 5.27: FT-IR spectra and PXRD pattern of PBI-CO (AC, T_R= 200 °C, t_R= 3d); thermal annealed PPy-CO
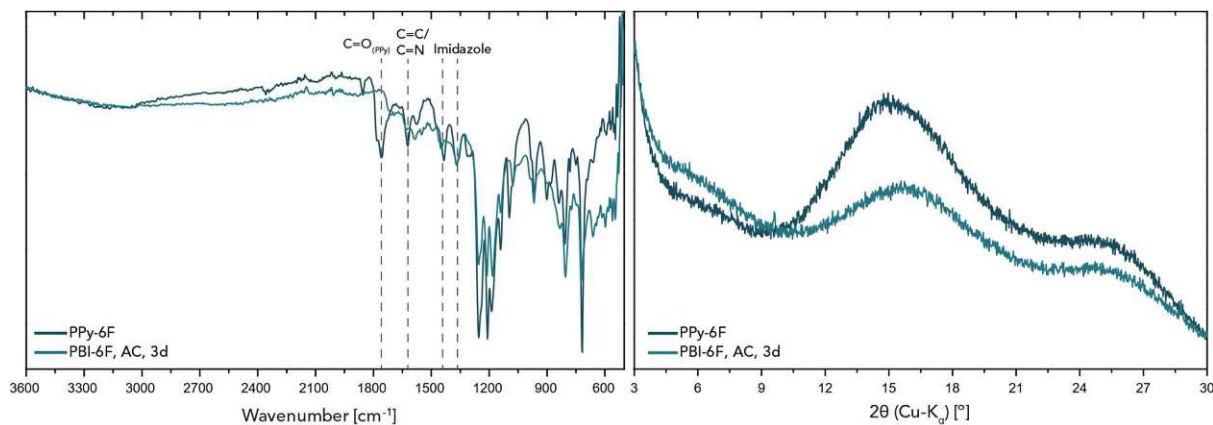
Figure 5.28: FT-IR spectra and PXRD pattern of PBI-6F (AC, T_R= 200 °C, t_R= 3d) and thermal annealed PPy-6F
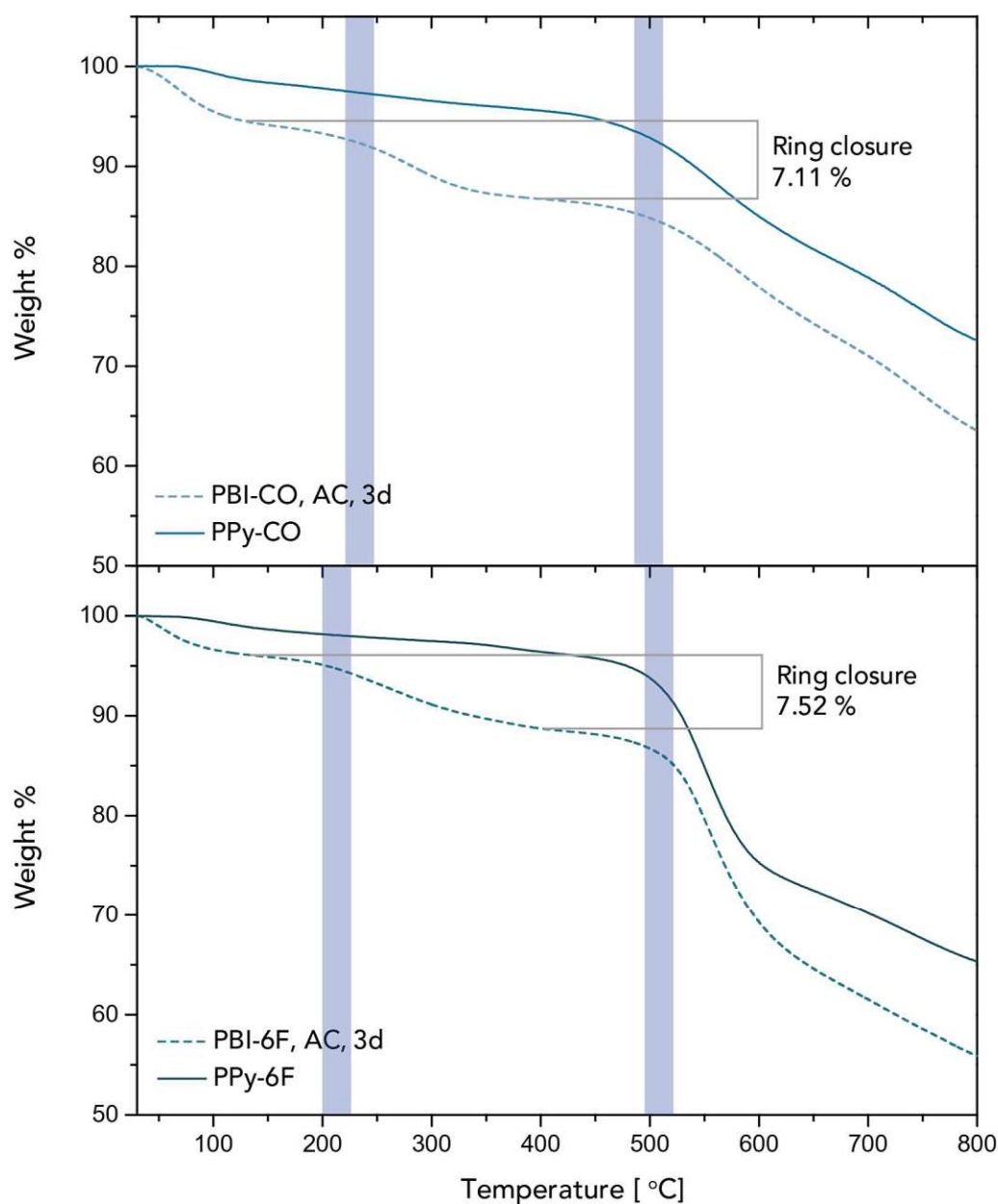
Figure 5.29: TGA curve of a) PBI-CO (AC, T_R= 200 °C, t_R= 3d) and thermal annealed PPy-CO b) PBI-6F (AC, T_R= 200 °C, t_R= 3d) and thermal annealed PPy-6F

The thermal properties of both PPy were investigated by TGA (Figure 5.29) and the results are summarised in Table 5.7. Both polymers showed good thermal stability similar to that prepared via MW. An initial weight loss was seen around ~100 °C in all samples, which can be attributed to the removal of moisture and trapped gases. Further, the PBI-intermediate samples showed a slope around 250 °C, which is due to incomplete condensation. The curing

improved the thermal stability of the polymers (see $T_{10\%}$). The residual weight at 800 °C also increased after curing.

Table 5.7: Comparison of thermal properties of the PBI-intermediates and PPys

	T_d	$T_{5\%}$	$T_{10\%}$	R_w
	°C	°C	°C	%
PBI-CO, AC, 3d	484.7	111.9	282.5	63.5
PBI-CO, AC, 5d	482.5	233.2	303.7	62.2
PPy-CO (AC, 3d)	485.2	440.8	540.8	72.6
PBI-CO, MW, 1h	532	58.3	275.8	63.4
PPy-CO (MW, 1h)	530	175.8	546.6	69.6
PBI-6F, AC, 3d	513	203.6	337.4	55.9
PBI-6F, AC, 5d	510.4	271.8	427.2	58.7
PPy-6F (AC, 3d)	509.1	478.7	528.8	65.3
PBI-6F, MW, 1h	524.6	72	305.4	55.5
PPy-6F (MW, 1h)	530	310.5	541.9	61.1

T_d- thermal decomposition temperature; $T_{5\%}$, $T_{10\%}$- temperature at 5% and 10% weight loss; R_w- residual weight at 800 °C.

The morphology of the PBI-intermediates prepared in autoclaves and respective thermally cured PPys were studied by SEM (Figure 5.30). The micrographs of show that the products are mostly spherical agglomerates or fused spherical particles.
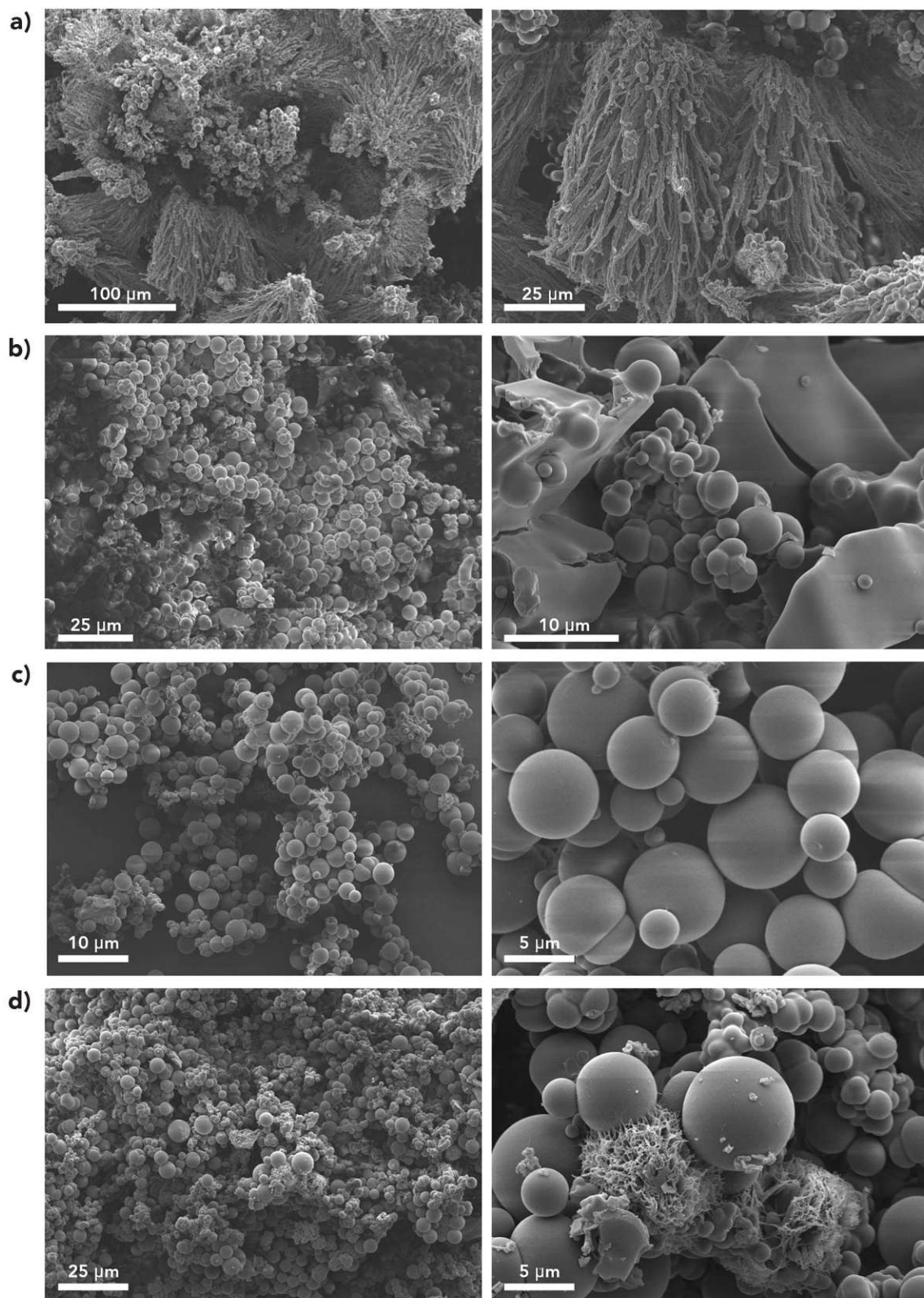
Figure 5.30: SEM pictures of a) PBI-CO (AC, T_R= 200 °C, t_R= 3d); b) PBI-6F (AC, T_R= 200 °C, t_R= 3d); c) PPy-CO; d) PPy-6F

6. Conclusion and Outlook

In this thesis, two different aspects of organic polymers have been discussed: i) Synthesis strategies to generate crystalline frameworks and conjugated ladder polymers hydrothermally ii) Exploring various linking chemistries achieved through HT method: amide, benzimidazole and imidazopyrrolone linkages.

In the first part of the thesis, the general feasibility of generating a crystalline polyamide material via HTP was demonstrated. A one-pot HTP setup, utilizing nothing but water and the monomers (trigonal carboxylic acid TmA and linear aromatic diamine Bz) was employed to generate PAM. It is believed to be constituted by numerous fused polyamide macrocycles, similar to those present in a framework. The PXRD data indicates that the product did not possess an extended COF structure but rather a fused hexagonal macrocyclic structure. After screening it was found that HOAc, which is typically employed as a modulator to facilitate the formation of crystalline framework, had no effect in synthesis, except for the morphology of the material.

In the second part, retracing similar steps, we were able to successfully generate crystalline PBI materials through hydrothermal methods from the monomers TmA and DABz. These materials also exhibited fused hexagonal macrocyclic structure and not an extended framework. Here, the addition of HOAc as modulator yielded product with notable crystallinity, confirming the presence of framework-like structures. The generated PBIMs exhibited significant thermal structural stability up to 350 °C and displayed interesting tunable morphologies indicative for crystallinity and layered structure. It was also found that the reaction time of PBIM-HOAc can be reduced with modified HTP setup using a sealed ampoule reactor.

In the final part, a rapid, straightforward, and environmentally friendly MW-assisted HT synthetic method for generating polybenzimidazoles using appropriate flexible aromatic tetra-amines and dianhydrides was demonstrated. These polybenzimidazoles could be subsequently converted to fully aromatic rigid-chain imidazopyrrolone polymers through solvent-free thermal annealing process, eliminating the need for complex procedures. Even though the final PPy products were amorphous, they exhibited high-temperature stability (>500 °C). The MW-assisted HT synthesis consistently yielded monodisperse PBI-COOH particles, and the morphology was conserved during the thermal annealing process. Additionally, fine dispersions of PPy in appropriate solvents were made successfully. All these features could contribute to the processability of these polymers while maintaining their intrinsic thermal stability.

In summary, this thesis emphasizes that HTP is a powerful synthetic method, and its potential has only just begun to be explored in the field of HPPs. In the past, HTP has been proven to be a potent method for obtaining linear polyimide materials. In this work, the scope of HTP was expanded to include amide, benzimidazole, and imidazopyrrolone linkages. Modulator-assisted as well as MW-assisted HT methods were developed and optimized to generate both crystalline materials and amorphous conjugated ladder polymers. This environmentally benign method has been advanced to a new level for generating highly functional and green materials. Considering this, it is fair to believe that HT methods might contribute to a more sustainable and technologically advanced future.

94

A. Appendix

A.1 Plots and Microscopy Images

A.1.1 ATR-FT-IR Spectra
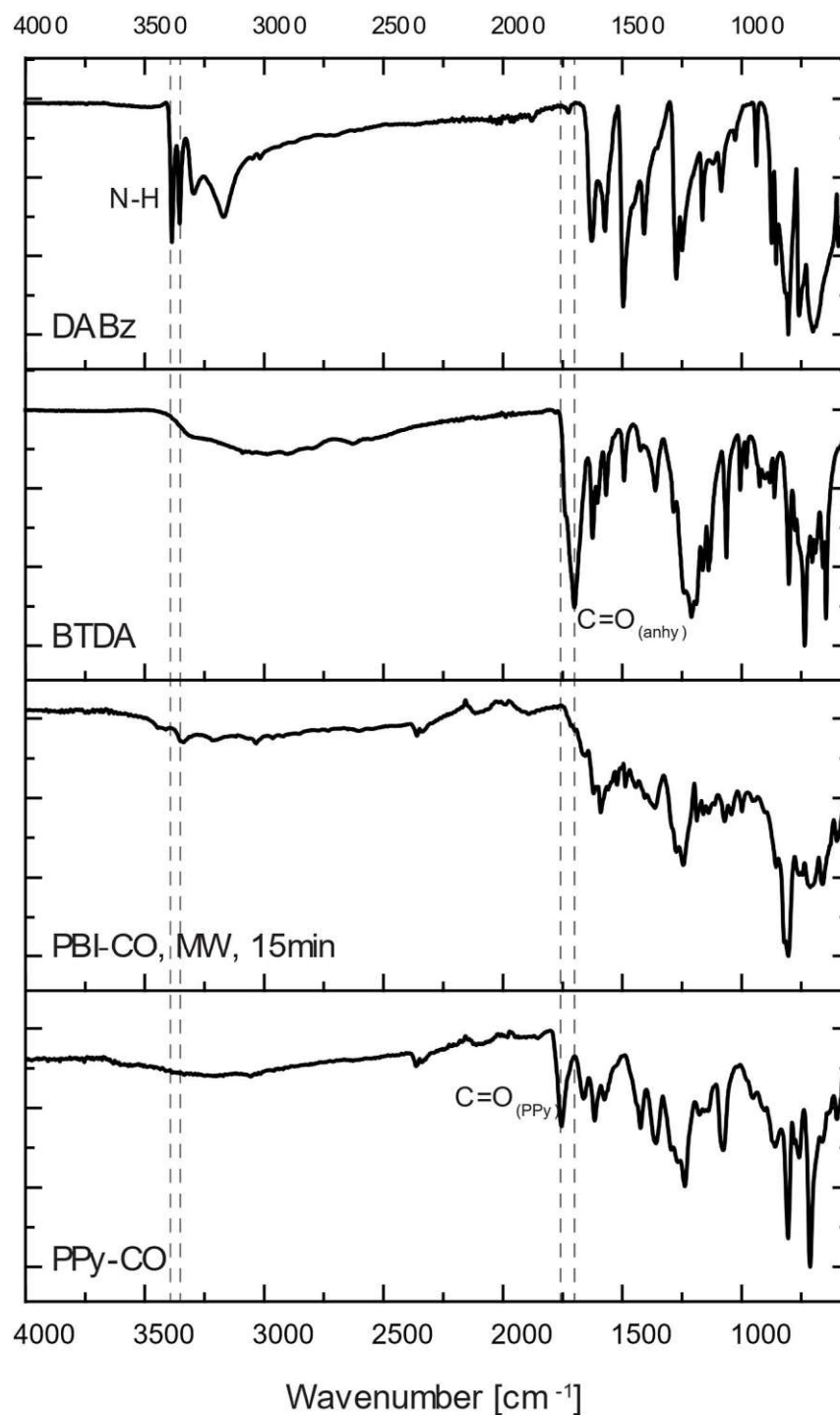
Figure A.1: ATR-FT-IR spectra of DABz; BTDA; PBI-CO (MW, T_R= 200 °C, t_R= 15min); thermal annealed PPy-CO
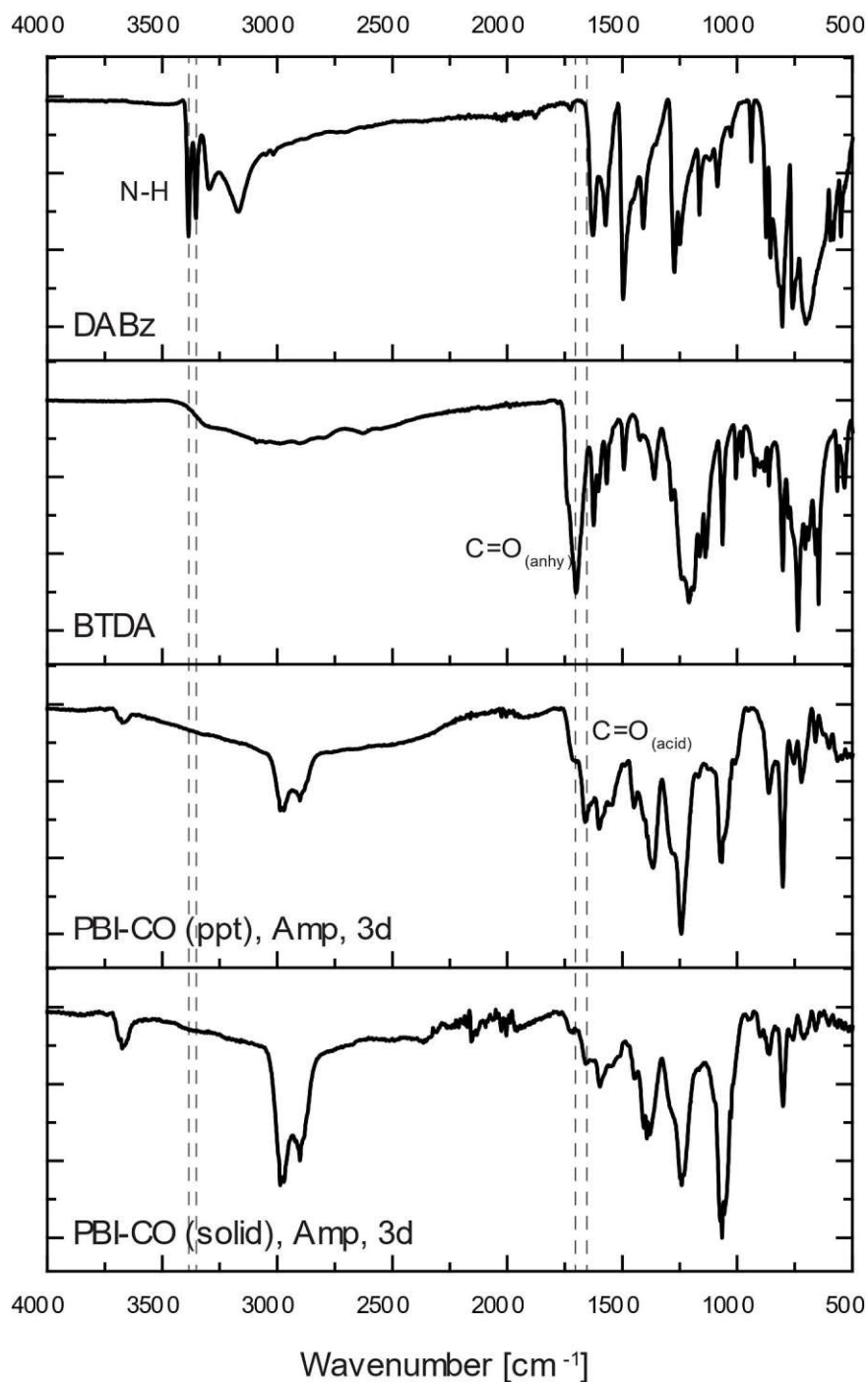
Figure A.2: ATR-FT-IR spectra of DABz; BTDA; PBI-CO precipitate/top phase (Ampule, T_R= 200 °C, t_R= 3d); PBI-CO solid/bottom phase (Ampule, T_R= 200 °C, t_R= 3d)
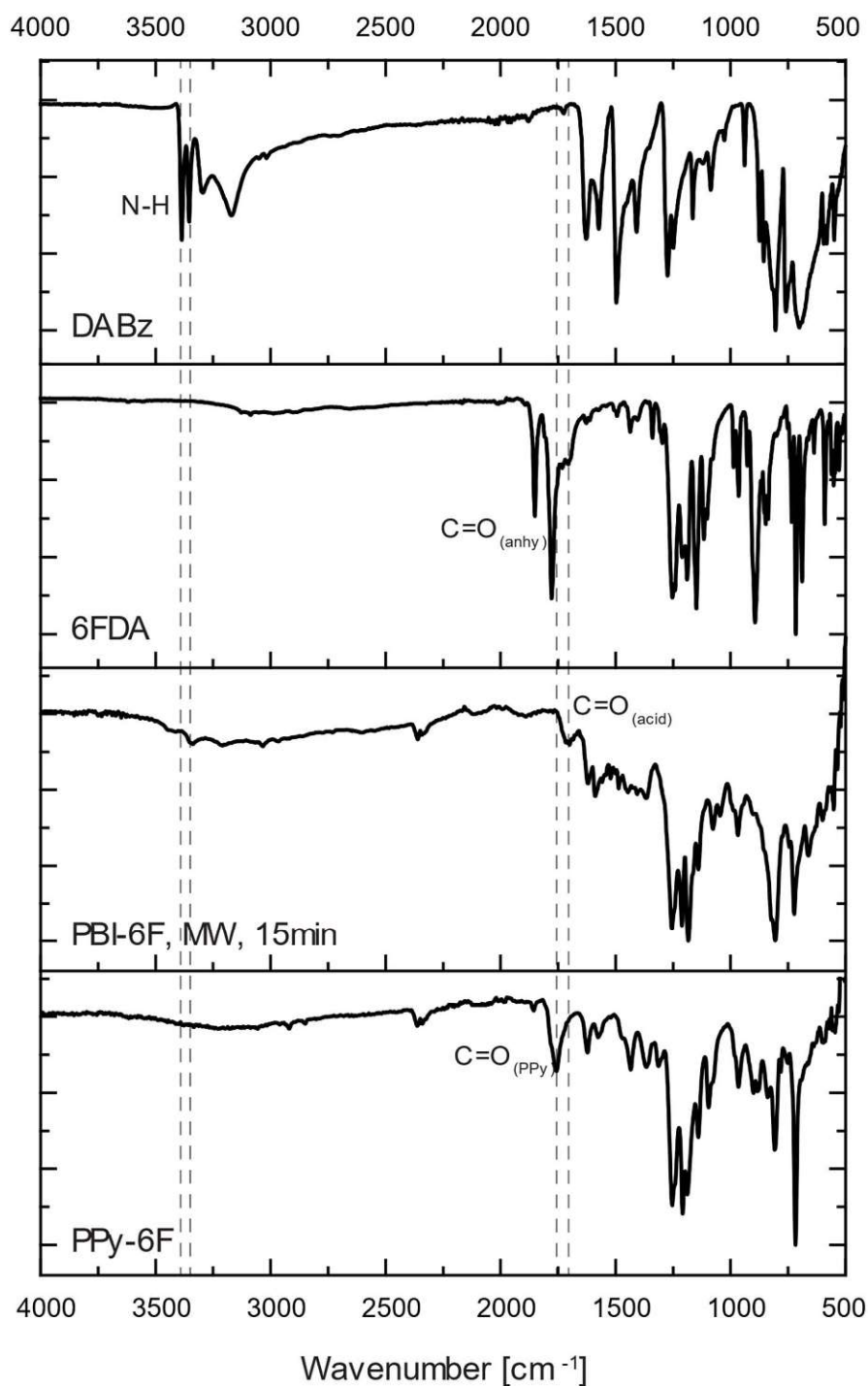
Figure A.3: ATR-FT-IR spectra of DABz; 6FDA; PBI-6F (MW, T_R= 200 °C, t_R= 15min); thermal annealed PPy-6F
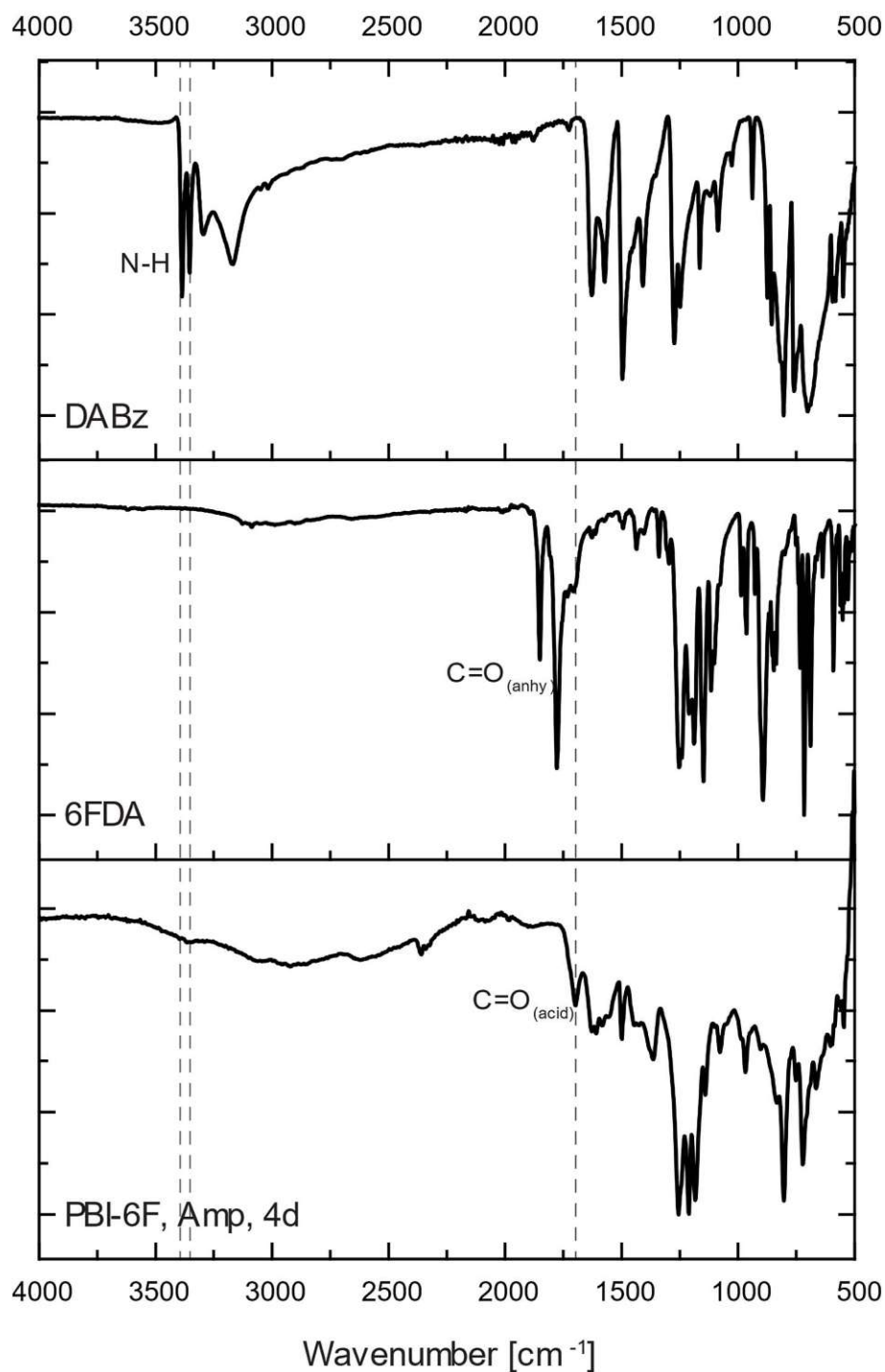
Figure A.4: ATR-FT-IR spectra of DABz; 6FDA; PBI-6F (Ampule, T_R= 200 °C, t_R= 4d)

A.1.2 PXRD patterns
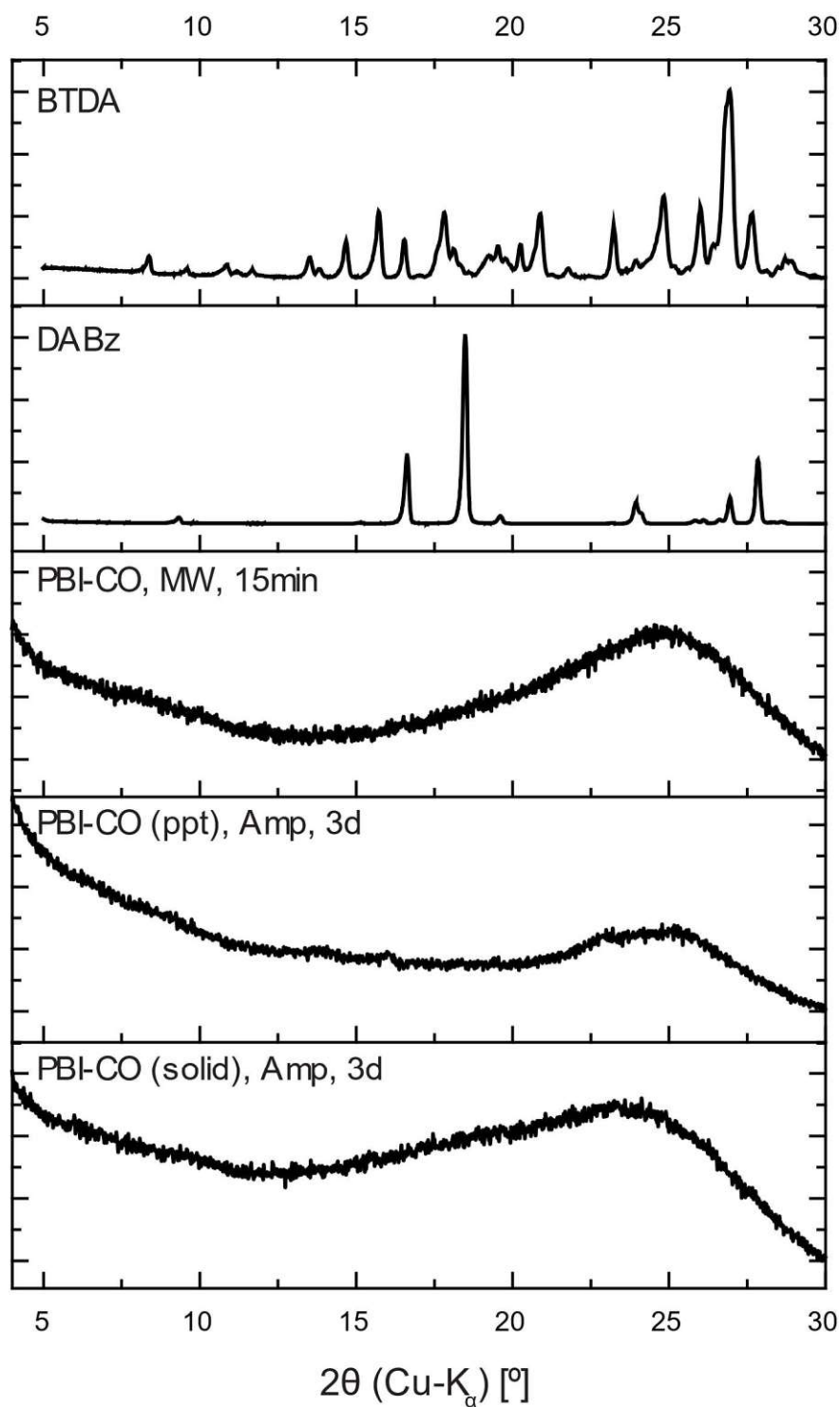
Figure A.5: PXRD pattern of BTDA; DABz; PBI-CO (MW, T_R= 200 °C, t_R= 15min); PBI-CO precipitate/top phase (Ampule, T_R= 200 °C, t_R= 3d); PBI-CO solid/bottom phase (Ampule, T_R= 200 °C, t_R= 3d)
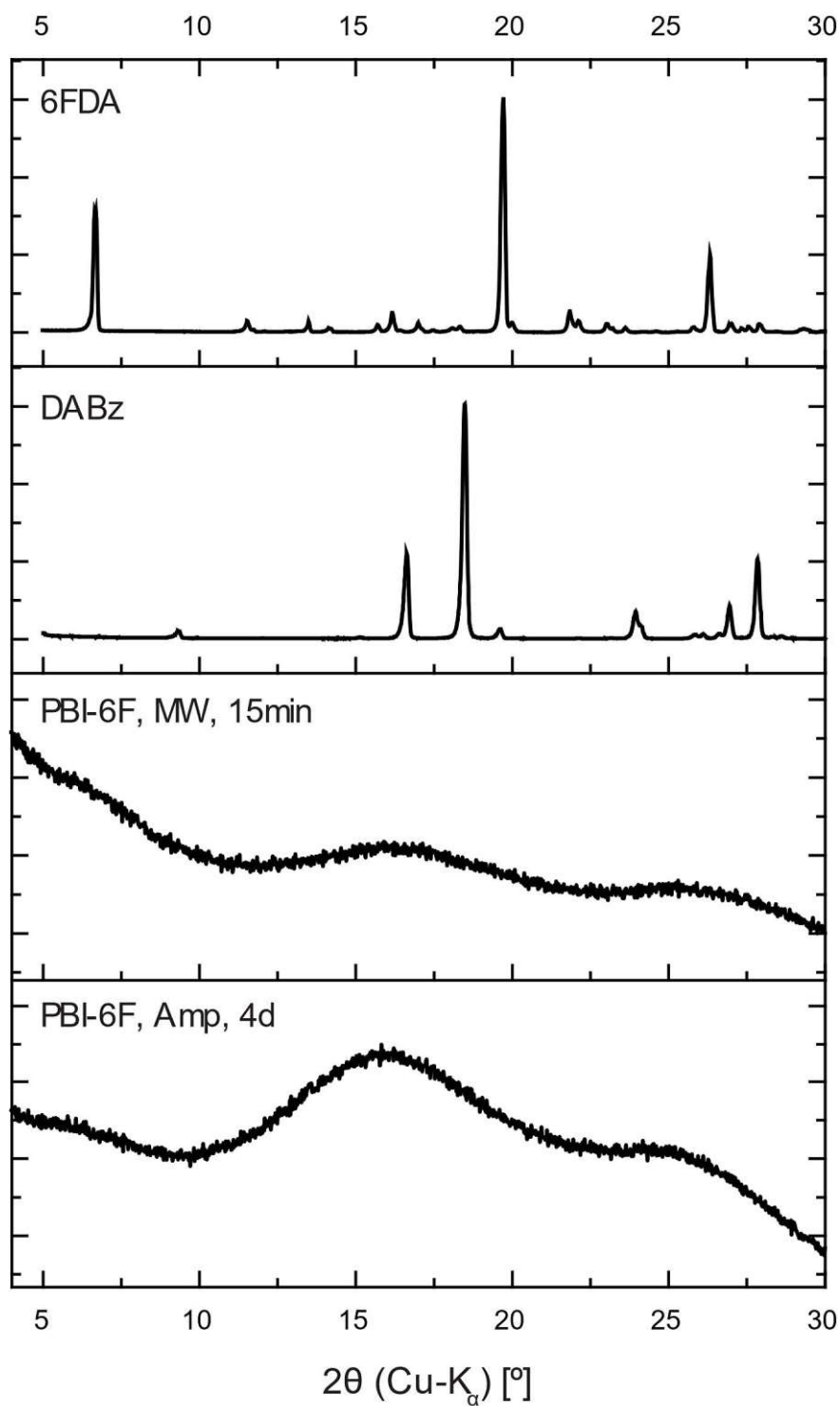
Figure A.6: PXRD pattern of 6FDA; DABz; PBI-6F (MW, T_R= 200 °C, t_R= 15min); PBI-6F (Ampule, T_R= 200 °C, t_R= 3d)

A.1.3 Thermogravimetric Analysis Plots
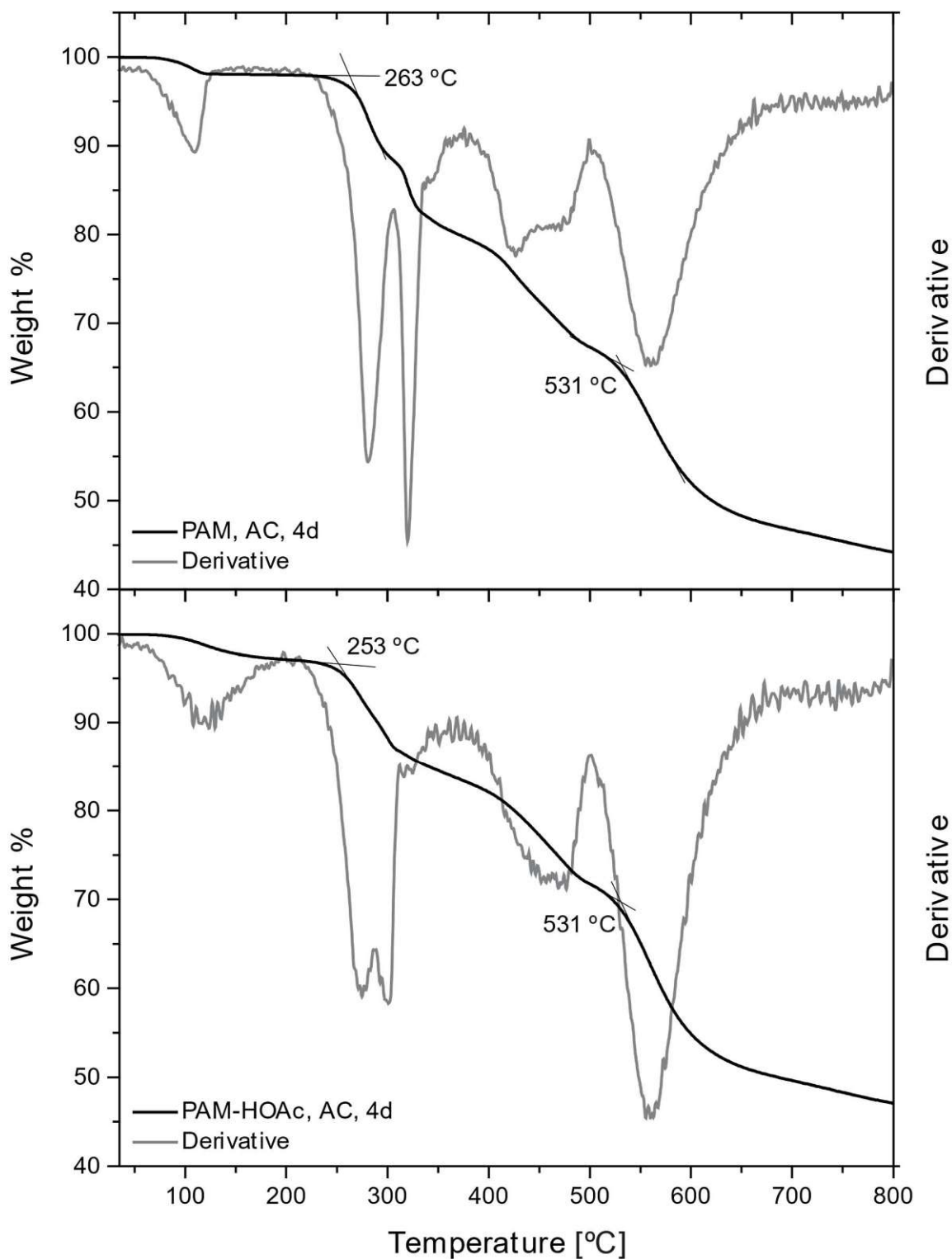
Figure A.7: TGA curve of PAM and PAM-HOAc (AC, T_R= 200 °C, t_R= 4d)
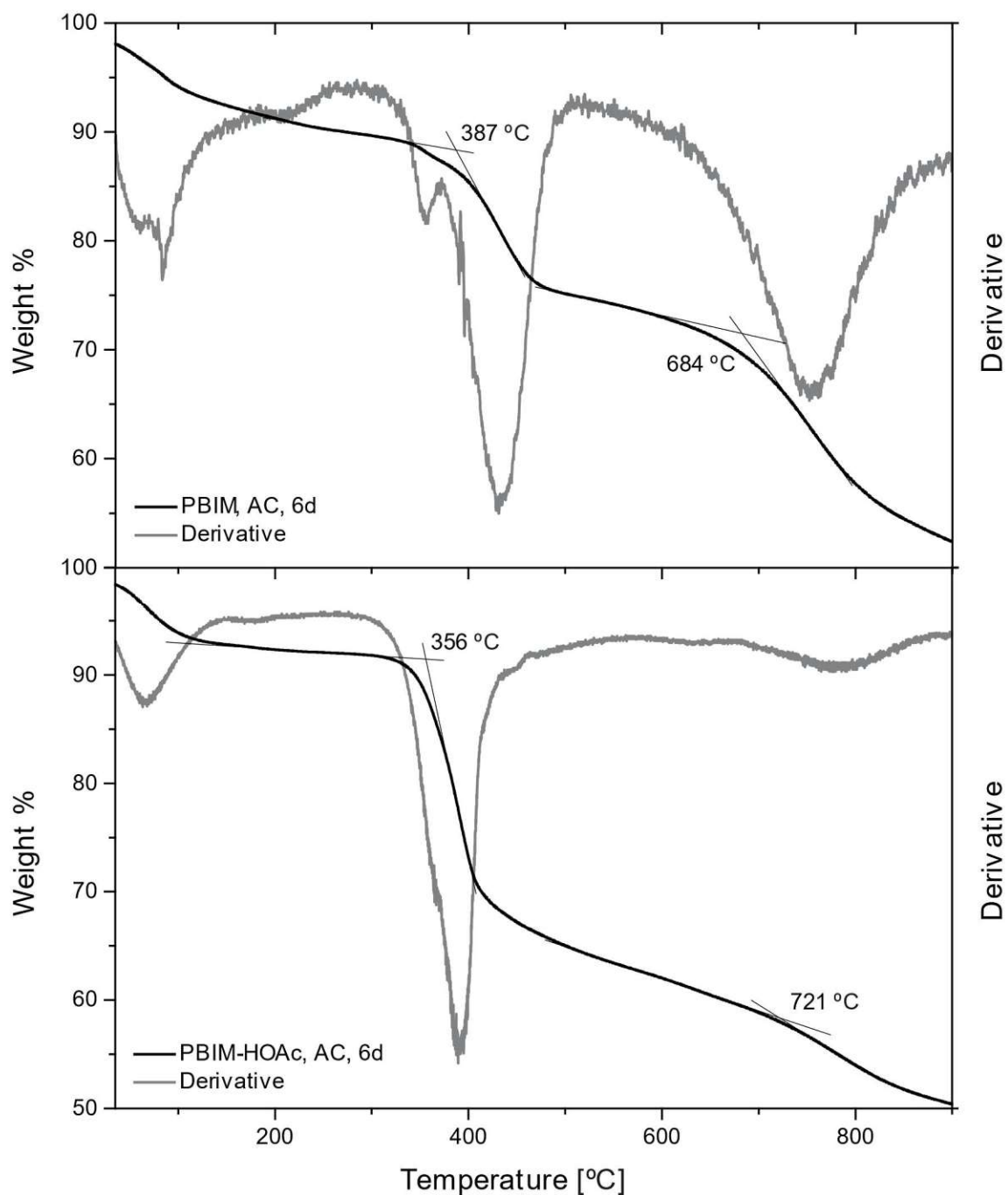
Figure A.8: TGA curve of PBIM and PBIM-HOAc (AC, T_R= 200 °C, t_R= 6d)
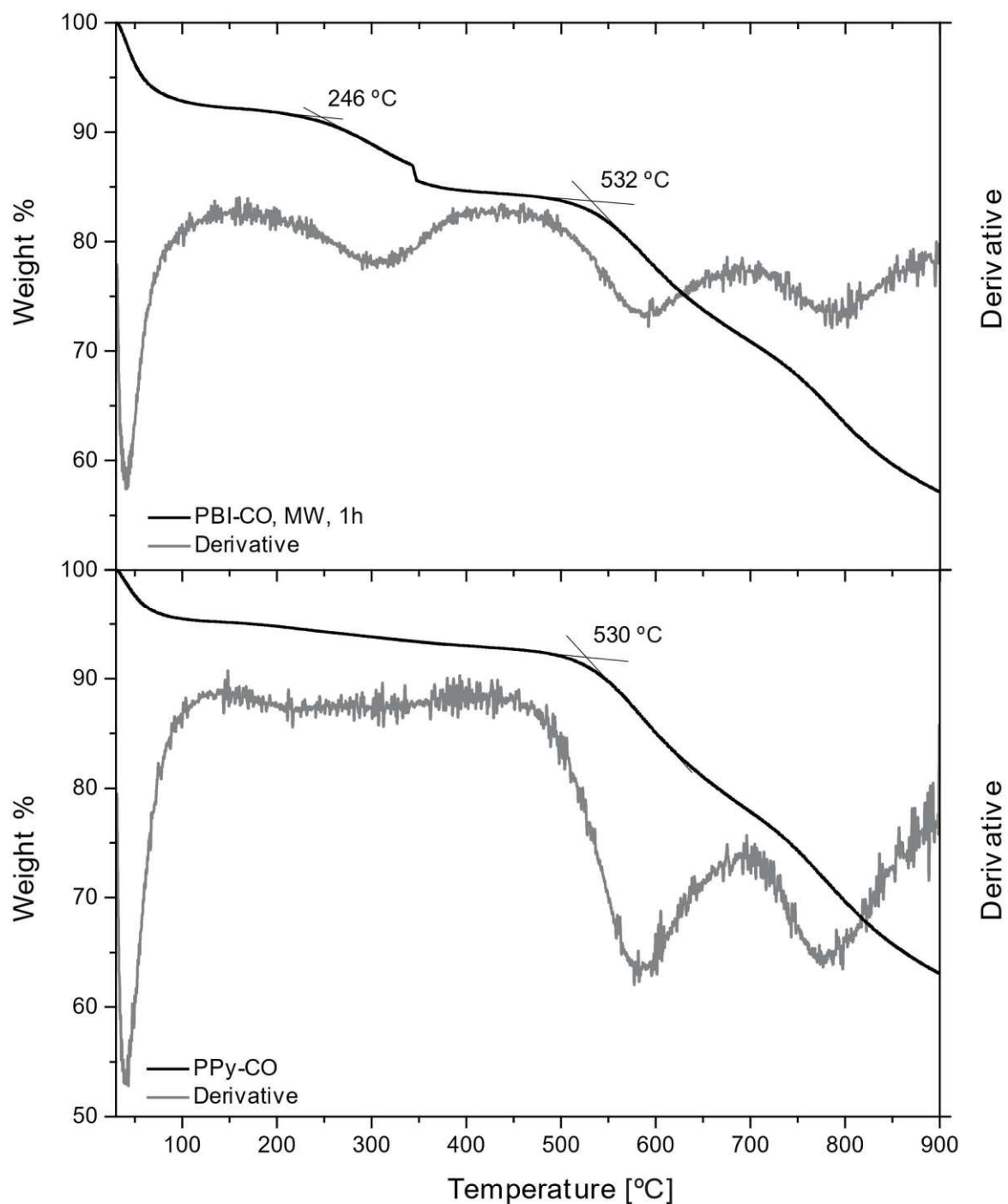
Figure A.9: TGA curve of PBI-CO (MW, $T_R = 200\,°C$, $t_R = 1h$) and thermal annealed PPy-CO
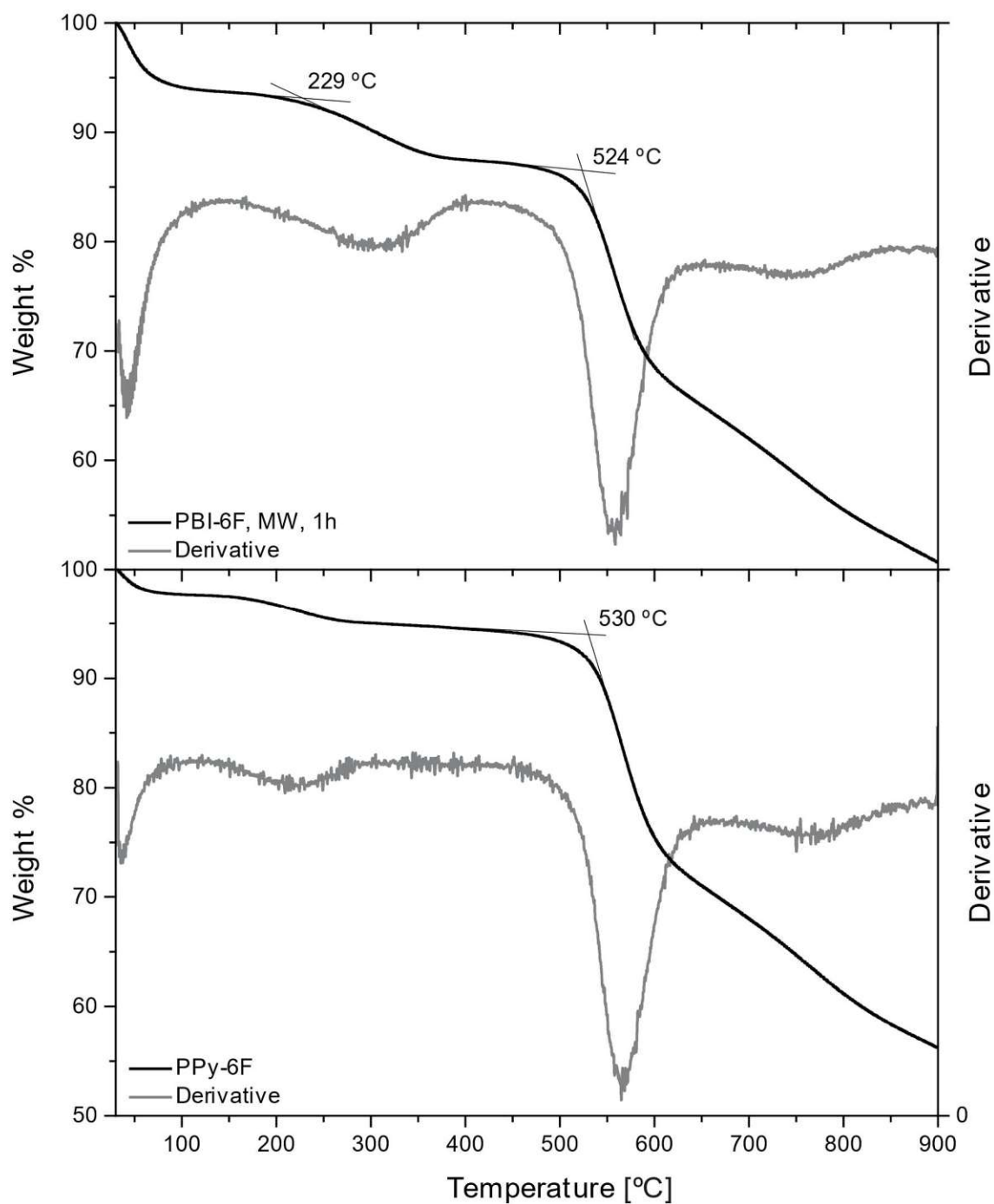
Figure A.10: TGA curve of PBI-6F (MW, T_R= 200 °C, t_R= 1h) and thermal annealed PPy-6F

A.1.4 Transmission Electron Microscopy Images
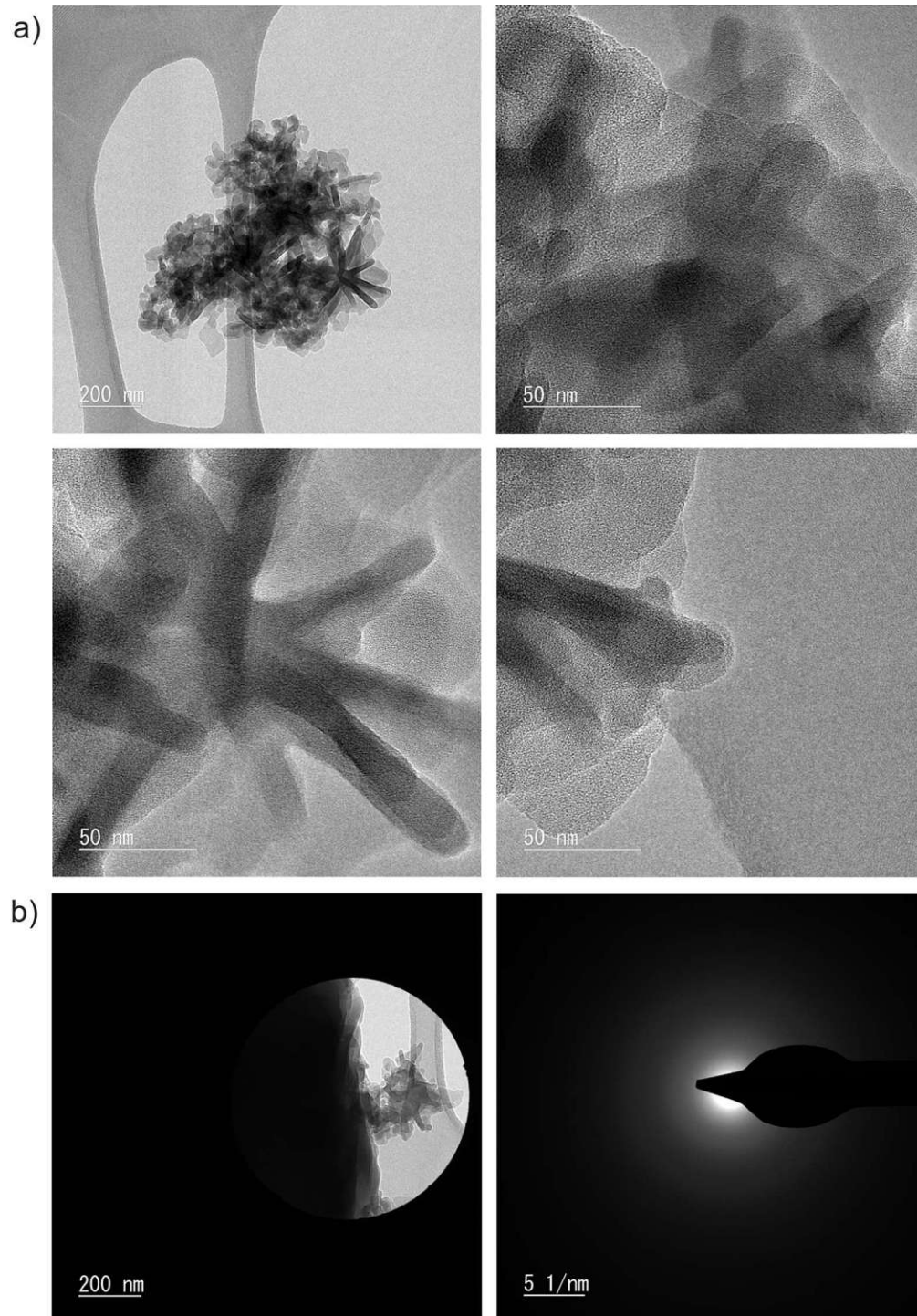
Figure A.11: a) TEM images and b) Selected area electron diffraction (SAED) images of PAM
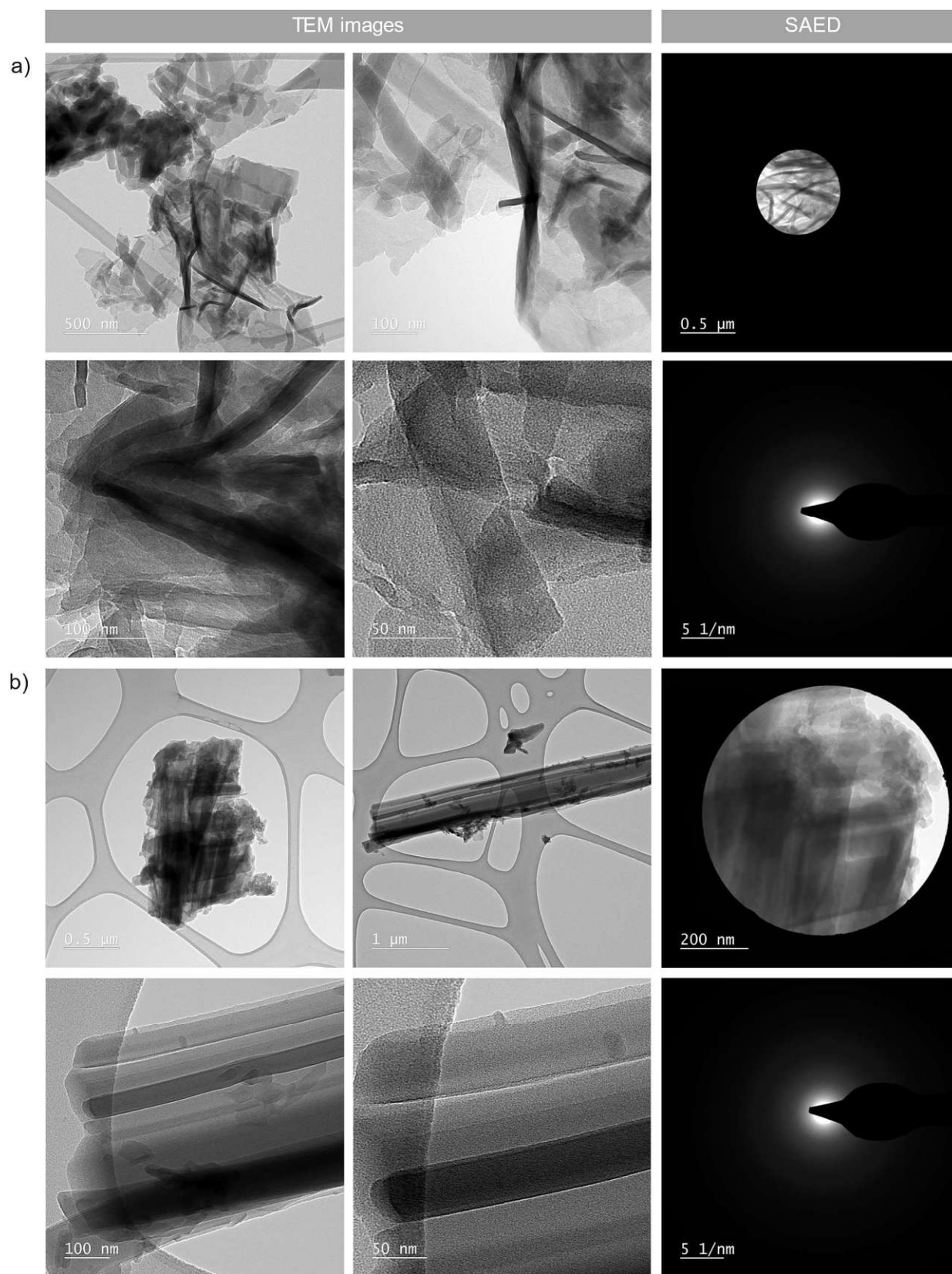
Figure A.12: TEM and SAED images of a) PBIM and b) PBIM-HOAc

A.2 Calculations

A.2.1 Indexing of PBIM-HOAc SAXS reflections

Interplanar spacing (d) of miller indices (hkl) can be deduced from hexagonal lattice equation

$$\frac{1}{d_{hkl}{}^2} = \frac{4}{3}\left(\frac{h^2 + hk + k^2}{a^2}\right) + \frac{l^2}{c^2}$$

d-spacing of miller indices (100) (110) (200) were

$$\frac{1}{d_{100}{}^2} = \frac{4}{3}\left(\frac{1}{a^2}\right)$$

$$\frac{1}{d_{110}{}^2} = \frac{4}{3}\left(\frac{3}{a^2}\right)$$

$$\frac{1}{d_{200}{}^2} = \frac{4}{3}\left(\frac{4}{a^2}\right)$$

Scattering vector (q) is related to d in real-space units as

$$q = \frac{2\pi}{d}$$

The ratio between q-values of miller indices (100) (110) (200) were deduced from equations above

$$q_{100} : q_{110} : q_{200} = 1 : \sqrt{3} : 2$$

The q-values from PBIM-HOAc SAXS reflections were indexed to the respective miller indices since it satisfies the ratio. The respective d-spacing were calculated from q-values using the equation above (Table A.1).

Table A.1: Miller indices and *d*-spacing of the corresponding experimental *q*-values.

q	Ratio	(hkl)	d-spacing
nm^{-1}			nm
3.78	1	(100)	1.66
6.57	$\sqrt{3}$	(110)	0.958
7.56	2	(200)	0.831

The final results for the lattice constant were $a = 19.16$ Å, $c = 3.28$ Å

A.2.2 Framework simulations and unit cell parameters

a)

Hexagonal lattice

Simulated- a=28.07 Å, c=3.44 Å

b)

Hexagonal lattice

Simulated- a=28.07 Å, c=6.88 Å

c)

Hexagonal lattice

Simulated- a=28.07 Å, c=10.32 Å

d)

Hexagonal lattice

Simulated- a=25.59 Å, c=3.51 Å

e)

Hexagonal lattice

Simulated- a=25.27 Å, c=6.78 Å
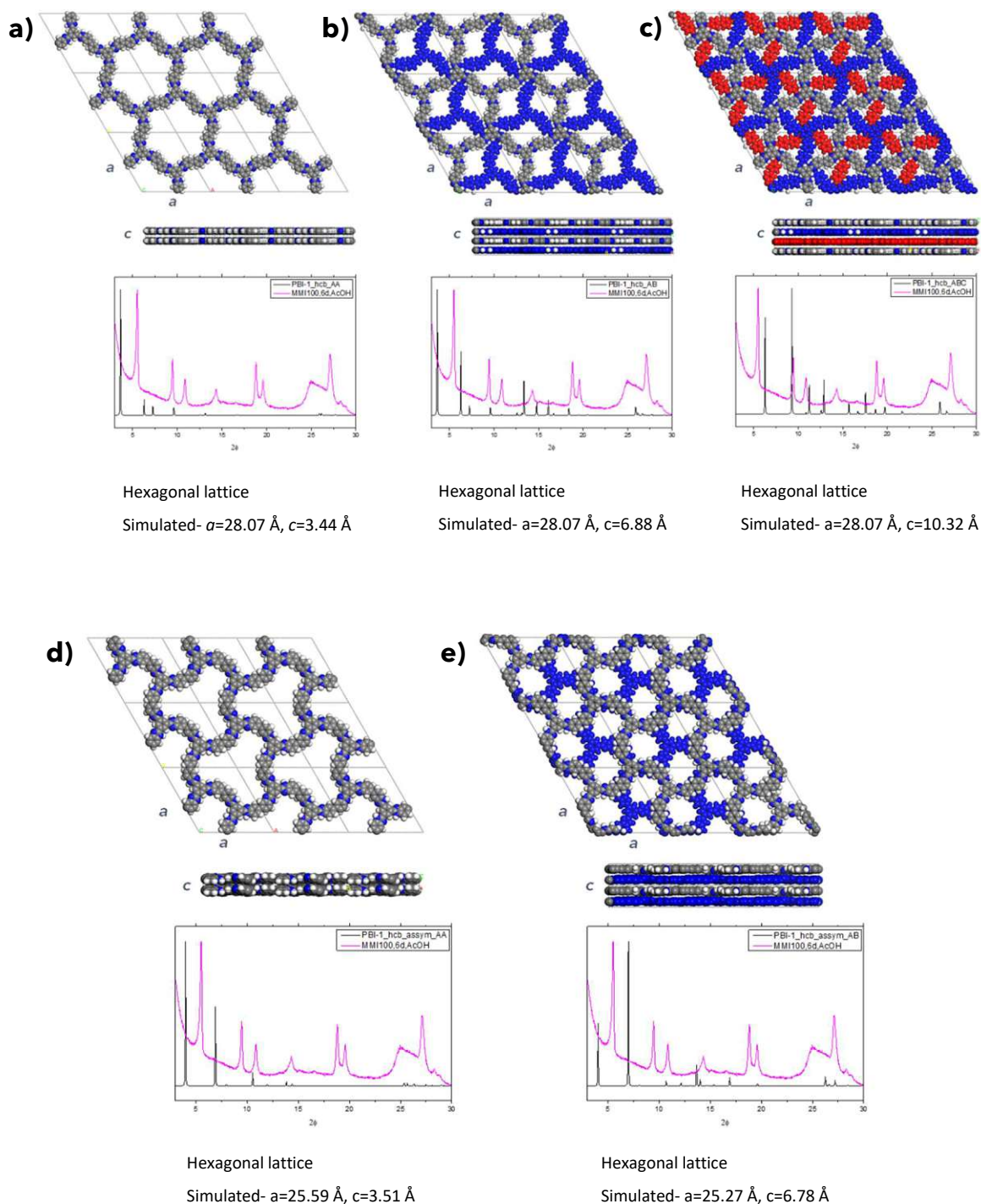
Figure A.13: Computational energy minimized frameworks in honeycomb net (hcb) and simulated PXRD patterns (black curve): a) PBI-COF in hcb with AA stacking; b) PBI-COF in hcb with AB stacking; c) PBI-COF in hcb with ABC stacking; d) "cis" PBI-COF in hcb with AA stacking; e) "cis" PBI-COF in hcb with AB stacking

Cubic lattice

Simulated- a=44.28 Å

Cubic lattice

Simulated- a=45.22 Å

Cubic lattice

Simulated- a=21.46 Å
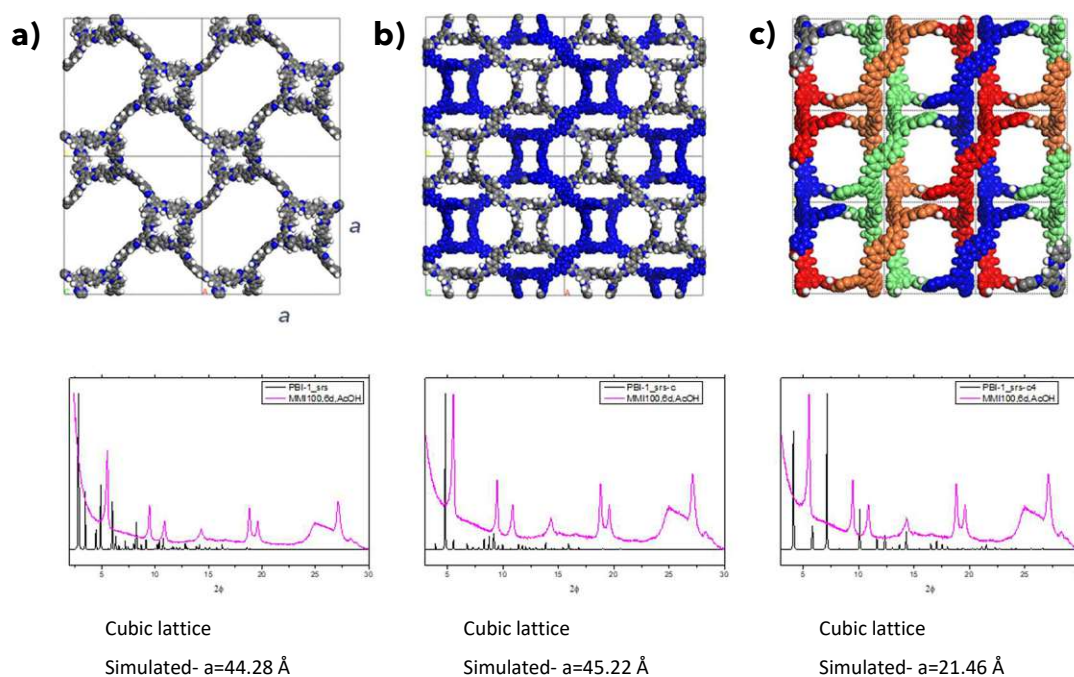
Figure A.14: Computational energy minimized frameworks in cubic lattice (srs) and simulated PXRD patterns (black curve): a) PBI-COF in srs net; b) PBI-COF in srs-c net; c) PBI-COF in srs-c4 net

Hexagonal lattice

Simulated- a=30.87 Å, c=3.43 Å

Hexagonal lattice

Simulated- a=30.88 Å, c=6.37 Å

Hexagonal lattice

Simulated- a=30.17 Å, c=6.53 Å
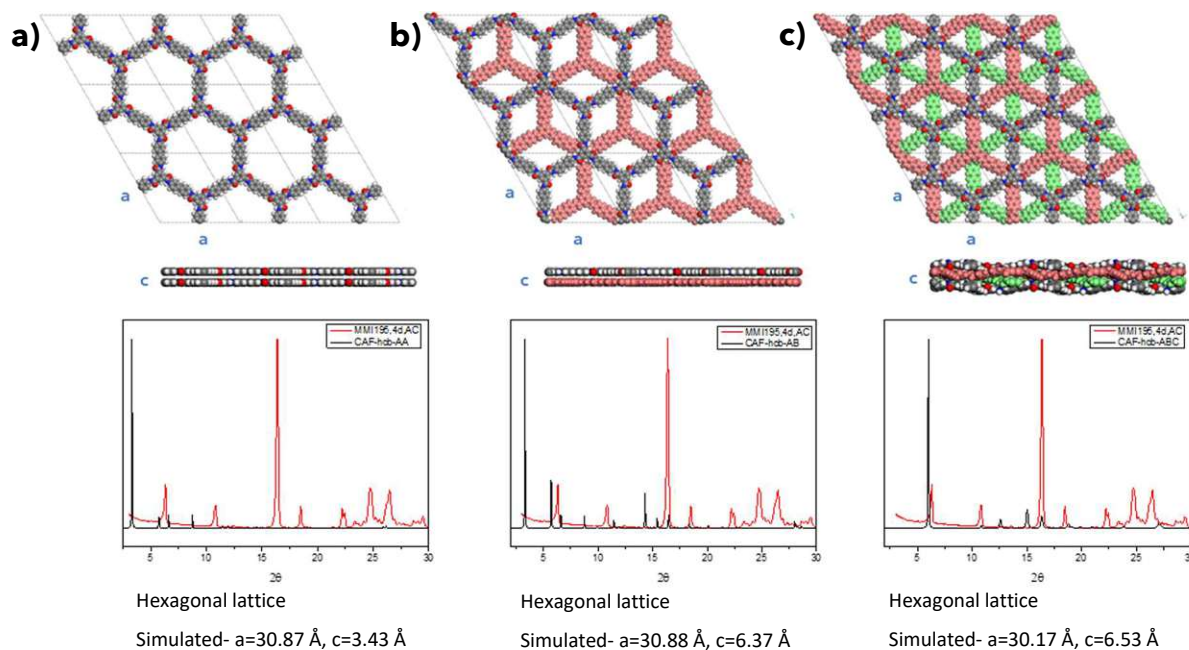
Figure A.15: Computational energy minimized frameworks in honeycomb net (hcb) and simulated PXRD patterns (black curve): a) CAF in hcb with AA stacking; b) CAF in hcb with AB stacking; c) CAF in hcb with ABC stacking
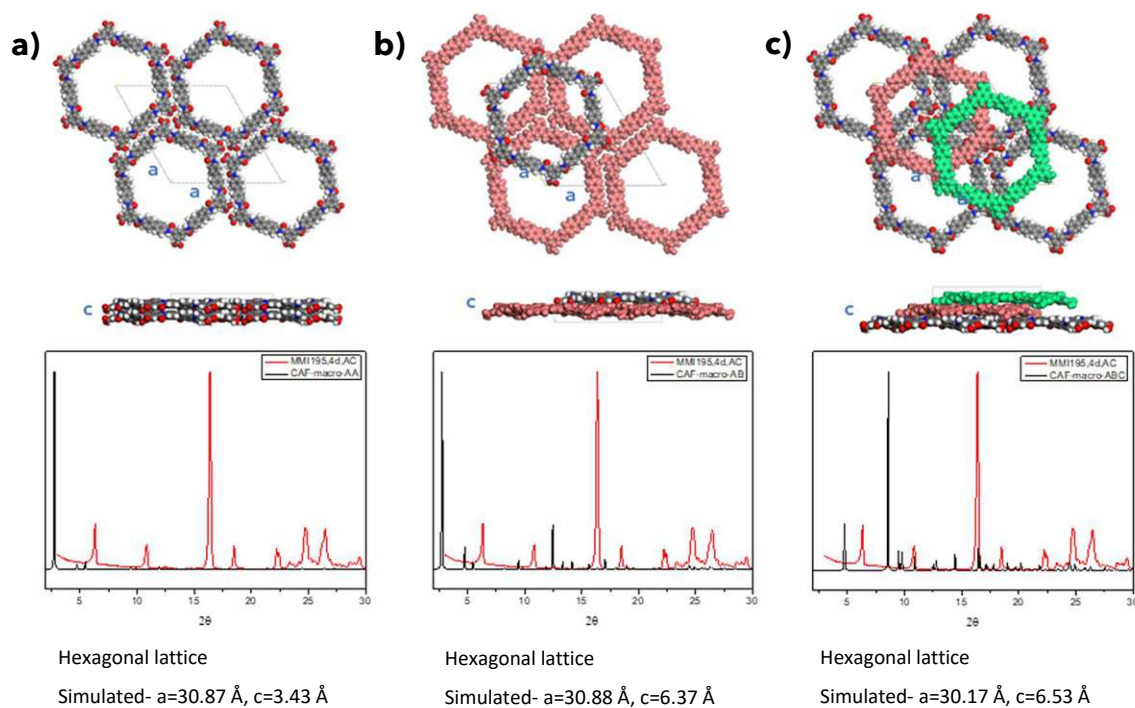
Figure A.16: Computational energy minimized macrocycles in honeycomb net (hcb) and simulated PXRD patterns (black curve): a) amide macrocycles in hcb with AA stacking; b) amide macrocycles in hcb with AB stacking; c) amide macrocycles in hcb with ABC stacking

A.3 Instrument Methods and Materials

A.3.1 Attenuated Total Reflectance Fourier Transform Infrared (ATR-FTIR) Spectroscopy

Fourier transform infrared (FT-IR) spectroscopy is based on the interaction of a molecule with infrared spectrum of the electromagnetic irradiation. The measurement is conducted by placing the sample (solid or liquid) into the IR beam chamber or a sample holder equipped with a ATR (attenuated total reflectance) crystal. When exposed to infrared radiation, sample molecules selectively absorb radiation of specific wavelengths according to the vibrational frequency of its chemical bonds, while letting others pass through it. The resulting signal at the detector is a spectrum representing the specific fingerprint signals which correspond to the frequencies of the particular chemical bond. Thus, it is a useful method to determine the presence of specific functional groups in a molecule. The commonly used region for infrared absorption spectroscopy is $4000 \sim 400$ cm^{-1} because the absorption radiation of most organic compounds and inorganic ions is within this region.

In this thesis, ATR-FTIR spectroscopy has been employed as an important technique for identifying the presence of specific functional groups in the products. ATR-FTIR spectra were recorded on a Bruker Tensor 27 in ATR mode, equipped with PIKE MIRacle single-reflection ATR unit, using Bruker OPUS software (version 4.0) for data collection and Spectragryph optical spectroscopy software (version 1.2.15) for data analysis. Resolution was set to 4 cm^{-1} and spectra were recorded from 4000 cm^{-1} to 500 cm^{-1}. In Table A.2 according to the absorption ranges, different functional molecule groups observed are listed.[125]

Table A.2: Range of absorption of different functional molecule groups observed.

Functional group	Wavenumber cm^{-1}
O-H	~3100 - 2700 (broad)
N-H (primary amine)	~3350 (doublet)
C=O (anhydrous acid)	~1850 – 1700 (broad/ doublet)
C=O (PPy)	~1760
C=O (acid)	~1700
C=O (amide)	~1630
C=C, C=N	~1600
Imidazole ring (in-plane)	~1450
C-N	~1360

A.3.2 Powder X-Ray Diffractometry (PXRD)

XRD is a very useful method to determine polymer crystallinity. The sample is bombarded with X-rays while rotating. Interaction of the X-rays with the material generates diffraction patterns that are used to describe sample crystallinity. PXRD measurements were conducted on a PANalytical X'Pert Pro multi-purpose diffractometer in Bragg Brentano geometry operating with a Cu anode at 40 kV, 40 mA and using an X-Celerator multichannel detector. Solid samples were in most cases ground and mounted as loose powders on (100) Si single crystal sample holders. For some samples with extremely low density, a drop of pentane was used for mounting. The method used for diffraction patterns recorded from 1° to 30° (2θ Cu-Kα1) employed 160.02 s/step with a step size of 0.0201 Å, and the method used for patterns from 5° to 60° (2θ Cu-Kα$_1$) employed 74.970 s/step with a step size of 0.01 Å. The sample holders were rotated with 4 s/turn during the measurement. PANalytical X'Pert Pro (version

2.2B and 2.2F) was used as instrument control software and for collecting measurement data PANalytical Data Collector 5.3- 6.0a were used.

A.3.3 Small Angle X-Ray Scattering (SAXS)

SAXS experiments were performed in a Nanostar (Bruker AXS) with X-rays from a microfocus source (Incoatec, High Brilliance, Cu-Kα radiation (λ = 0.1542 nm)) and a 2D position sensitive detector (Vantec 2000, Bruker AXS). SAXS data were collected at two to three different sample-to-detector distances (108 cm, 28 cm, 13 cm) to cover a wide q-range. The ground powders were placed between two tapes and measured under vacuum, depending on the scattering intensities of the samples and the sample-to-detector distances. SAXS patterns of the samples and the background (the tapes) were radially integrated to determine the SAXS intensities in dependence of the scattering vector q,

$$q = \left(\frac{4\pi}{\lambda}\right) \cdot \sin\theta$$

with 2θ being the scattering angle and λ = 0.1542 nm, the X-ray wavelength. The background was subtracted with a factor taking the transmission of sample and background into account. The factor was obtained from intensities of the primary beam measured with a partly transparent beamstop. All patterns were azimuthally integrated.

A.3.4 Thermogravimetric Analysis (TGA)

Thermogravimetric analysis was carried out using a Netzsch TG 209 analyzer at a heating rate of 10 K/min under nitrogen atmosphere, equipped with NETZSCH Proteus (Version 4.3) software.

A.3.5 Nuclear Magnetic Resonance (NMR) Spectroscopy

^{1}H-NMR Solution Spectroscopy

^{1}H-NMR spectra were recorded on a Bruker AC400 or AC600 spectrometer (400 and 600 MHz). Chemical shifts are reported in ppm (δ) relative to tetramethylsilane and calibrated using solvent residual peaks. Data are shown as follows: Chemical shift, multiplicity (s = singlet, d = doublet, t = triplet, q = quartet, quin = quintet, m = multiplet, b= broad signal), coupling constant (J, Hz) and integration. ACDLabs NMR Processor (Academic Edition) was used for data analysis.

^{13}C-CPMAS solid-state NMR Spectroscopy

The spectra were acquired on a Bruker Avance NEO 500 wide bore system (Bruker BioSpin, Rheinstetten, Germany) using a 4 mm triple resonance magic angle spinning (MAS) probe in a dual set-up. The resonance frequency for ^{13}C NMR was 125.78 MHz, and 500.22 MHz for ^{1}H, respectively. The MAS rotor spinning speed was set to 14 kHz. Cross polarization (CP) was achieved by a ramped contact pulse with a contact time of 3 ms. During acquisition ^{1}H was high power decoupled using SPINAL with 64 phase permutations. The chemical shifts are reported in ppm and are referenced external for ^{13}C to adamantane by setting the low field signal to 38.48 ppm. ACDLabs NMR Processor (Academic Edition) was used for data analysis.

A.3.6 Low Pressure Gas Sorption Measurements

N$_2$ as Analyzing Gas

Nitrogen adsorption/desorption using a Quantachrome Instruments Autosorb 1C, surface area analyser at 77 K. Samples were degassed at 140 °C for 24 h under vacuum before analysis.

Brunauer-Emmett- Teller (BET) surface area was calculated in relative pressure range (P/P_0) from 0.05 to 0.35.

CO_2 as Analyzing Gas

Low pressure CO_2 physisorption isotherms were measured volumetrically at 195 K and 273 K up to 1 bar using an Autosorb-IQ-MP from Quantachrome equipped with a Quantachrome CryoCooler for temperature regulation. Isotherm points chosen to calculate the BET surface area were subject to the consistency criteria detailed by Rouquerol.[126] The pore size distribution was derived from the adsorption isotherms at 273 K using the Monte Carlo model for carbon adsorbents.

A.3.7 X-ray Photoelectron Spectroscopy (XPS)

XPS measurements were performed with a Thermo Fisher Microlab 310/350-spectrometer equipped with a twin anode Al/Mg-Kα X-ray source (XR3) and a hemispherical analyser have been used. Samples were mounted onto the sample holders using double-sided carbon tape. Pass energies of 70 eV and 20 eV as well as energy resolutions of 1 eV and 100 meV were used for survey and detail spectra respectively (excitation energy: 1486.6 eV / 1253.6 eV, beam power: 100W, angle: 60° to sample surface normal, base pressure: $1x10^{-8}$ mbar, pressure during measurements: $2x10^{-8}$ mbar). All measurements were carried out with the sample in normal emission angle with respect to the analyser.

Data analysis was done using the CASA XPS software package employing Shirley backgrounds[127] and Scofield sensitivity factors[128]. Curve fits using combined Gaussian-Lorentzian peak shapes were used to discern the components of detail spectra if not stated otherwise. Charge correction was applied so the adventitious carbon peak (C-C peak) was shifted to approximately 284.8 eV binding energy (BE).

All elemental composition values shown are in units of relative atomic percent (at%), where the detection limit in survey measurements usually lies around 0.1-0.5 at%, depending on the element. The accuracy of XPS measurements is around 10-20% of the values shown. Assignment of different components was primarily done according to literature.[129,130]

A.3.8 Microscopy Methods

Light Microscopy

Light microscopy was carried out using a Leica microsystems microscope with input voltages 100-240 V ($\sim$ 15 W) and 50/60 Hz.

Scanning Electron Microscopy (SEM)

SEM was carried out with a Quanta 200F FEI microscope. Typically, the samples were measured at 5 kV, with a working distance of 9- 10 mm and spot size 2.0. Prior to imaging, samples were sprinkled over a carbon-tape on steel sample holders and coated by sputtering with Au/Pd 60/40 alloy layer of 17 nm thickness using a Quarum Q105TS sample preparation system.

Transmission Electron Microscopy (TEM)

TEM measurements were carried out using a TECNAI F20 microscope equipped with X-FEG using 200 kV acceleration voltage. The sample was mounted on a carbon coated Cu-grid prior to measurement.

A.3.9 Inert thermal curing

A temperature-controlled horizontal split tube furnace (Carbolite, Germany) was equipped with a cylindrical quartz glass reactor. A constant flow of inert gas, either Nitrogen or Argon, was passed from one end to the other end. The T-range used for curing was 25-310 °C.

A.3.10 Supercritical carbon dioxide (scCO₂) activation

The scCO$_2$ activation setup is presented in Figure A.15. All extractions were performed with a scCO$_2$ device manufactured by Jasco (Jasco Corporation, Tokyo, Japan). Liquid CO$_2$ (>99.995% purity; with ascension pipe; Messer GmbH, Vienna, Austria) was pressurized by two CO$_2$-pumps (PU-2086, Jasco Corporation, Tokyo, Japan) with cooled heads (CF40, JULABO GmbH, Seelbach, Germany). An HPLC pump (PU-2089, Jasco Corporation, Tokyo, Japan) supplied required solvent. An oven (CO-2060, Jasco Corporation, Tokyo, Japan) with a heating coil was used and was thermostated to the desired temperature. HPLC-cartridge (L 127 mm, 10 mm i.d.) filled with sample was placed in the oven, subsequently, connected to the scCO$_2$ device. A back-pressure regulator (BP-2080, Jasco Corporation, Tokyo, Japan), a gas/liquid separator (HC-2086-01, Jasco Corporation, Tokyo, Japan), and a product collector (SCF-Vch-Bp, Jasco Corporation, Tokyo, Japan) were used to obtain any byproducts from the sample.
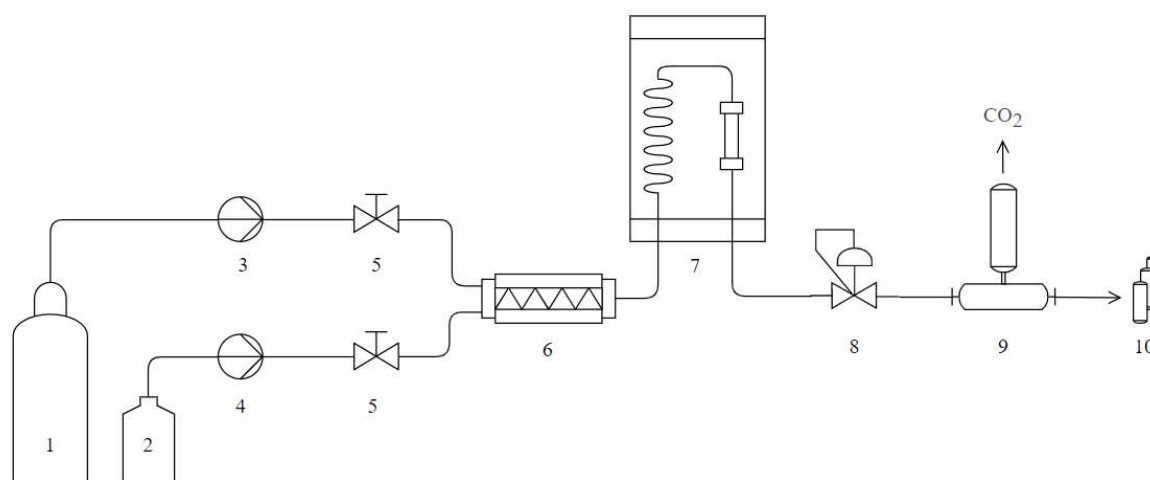
Figure A.17: Schematic representation of the continuous scCO$_2$ activation setup. 1) Liquid CO$_2$ supply; 2) solvent supply; 3) CO$_2$ pump; 4) solvent pump; 5) manually operated valve; 6) inline mixer; 7) thermostated oven with preheating coil and sample cartridge; 8) back pressure regulator; 9) gas-liquid separator; 10) fraction collector.

A.3.11 Materials

Trimesic acid (TmA, > 98 %, Merck), 3,3'-Diaminobenzidine (DABz, 98 %, TCI), benzidine (Bz, 98 %, Sigma Aldrich), o-phenylene diamine (OPDA, 99 %, Sigma Aldrich), 1,3,5-tris(4-aminophenyl)benzene (TAPB, 97 %, TCI) were purchased and used as received. Aniline, ethanol, acetone, THF, hydrochloric acid (>97%), sulphuric acid (>98%), DMF, glacial acetic acid (>99%), fuming nitric acid (>99%) and acetic anhydride were purchased from the university. Aniline and DMF were distilled prior to usage. For HTP, deionized and degassed (using nitrogen) water was used.

References

(1)   Ben, T.; Ren, H.; Ma, S.; Cao, D.; Lan, J.; Jing, X.; Wang, W.; Xu, J.; Deng, F.; Simmons, J. M.; Qiu, S.; Zhu, G. Targeted Synthesis of a Porous Aromatic Framework with High Stability and Exceptionally High Surface Area. *Angew. Chemie Int. Ed.* **2009**, *48* (50), 9457–9460. https://doi.org/10.1002/anie.200904637.

(2)   Li, Z.; Feng, X.; Zou, Y.; Zhang, Y.; Xia, H.; Liu, X.; Mu, Y. A 2D Azine-Linked Covalent Organic Framework for Gas Storage Applications. *Chem. Commun.* **2014**, *50* (89), 13825–13828. https://doi.org/10.1039/c4cc05665e.

(3)   Budd, P.; Msayib, K.; Tattershall, C.; Ghanem, B.; Reynolds, K.; Mckeown, N.; Fritsch, D. Gas Separation Membranes from Polymers of Intrinsic Microporosity. *J. Memb. Sci.* **2005**, *251* (1–2), 263–269. https://doi.org/10.1016/j.memsci.2005.01.009.

(4)   Gao, X.; Zou, X.; Ma, H.; Meng, S.; Zhu, G. Highly Selective and Permeable Porous Organic Framework Membrane for CO_2 Capture. *Adv. Mater.* **2014**, *26* (22), 3644–3648. https://doi.org/10.1002/adma.201400020.

(5)   Zhang, Y.; Riduan, S. N. Functional Porous Organic Polymers for Heterogeneous Catalysis. *Chem. Soc. Rev.* **2012**, *41* (6), 2083–2094. https://doi.org/10.1039/c1cs15227k.

(6)   Xiang, Z.; Cao, D. Synthesis of Luminescent Covalent-Organic Polymers for Detecting Nitroaromatic Explosives and Small Organic Molecules. *Macromol. Rapid Commun.* **2012**, *33* (14), 1184–1190. https://doi.org/10.1002/marc.201100865.

(7)   Liu, X.; Xu, Y.; Jiang, D. Conjugated Microporous Polymers as Molecular Sensing Devices: Microporous Architecture Enables Rapid Response and Enhances Sensitivity in Fluorescence-On and Fluorescence-Off Sensing. *J. Am. Chem. Soc.* **2012**, *134* (21), 8738–8741. https://doi.org/10.1021/ja303448r.

(8)   Singh, H.; Devi, M.; Jena, N.; Iqbal, M. M.; Nailwal, Y.; De Sarkar, A.; Pal, S. K. Proton-Triggered Fluorescence Switching in Self-Exfoliated Ionic Covalent Organic Nanosheets for Applications in Selective Detection of Anions. *ACS Appl. Mater. Interfaces* **2020**, *12* (11), 13248–13255. https://doi.org/10.1021/acsami.9b20743.

(9)   Fang, Q.; Wang, J.; Gu, S.; Kaspar, R. B.; Zhuang, Z.; Zheng, J.; Guo, H.; Qiu, S.; Yan, Y. 3D Porous Crystalline Polyimide Covalent Organic Frameworks for Drug Delivery. *J. Am. Chem. Soc.* **2015**, *137* (26), 8352–8355. https://doi.org/10.1021/jacs.5b04147.

(10)   Ding, S.-Y.; Dong, M.; Wang, Y.-W.; Chen, Y.-T.; Wang, H.-Z.; Su, C.-Y.; Wang, W. Thioether-Based Fluorescent Covalent Organic Framework for Selective Detection and Facile Removal of Mercury(II). *J. Am. Chem. Soc.* **2016**, *138* (9), 3031–3037. https://doi.org/10.1021/jacs.5b10754.

(11)   Ma, H.; Liu, B.; Li, B.; Zhang, L.; Li, Y. G.; Tan, H. Q.; Zang, H. Y.; Zhu, G. Cationic Covalent Organic Frameworks: A Simple Platform of Anionic Exchange for Porosity Tuning and Proton Conduction. *J. Am. Chem. Soc.* **2016**, *138* (18), 5897–5903. https://doi.org/10.1021/jacs.5b13490.

(12) Yang, R.-X.; Wang, T.-T.; Deng, W.-Q. Extraordinary Capability for Water Treatment Achieved by a Perfluorous Conjugated Microporous Polymer. *Sci. Rep.* **2015**, *5*, 10155. https://doi.org/10.1038/srep10155.

(13) Vyas, V. S.; Haase, F.; Stegbauer, L.; Savasci, G.; Podjaski, F.; Ochsenfeld, C.; Lotsch, B. V. A Tunable Azine Covalent Organic Framework Platform for Visible Light-Induced Hydrogen Generation. *Nat. Commun.* **2015**, *6* (1), 8508. https://doi.org/10.1038/ncomms9508.

(14) Liras, M.; Iglesias, M.; Sánchez, F. Conjugated Microporous Polymers Incorporating BODIPY Moieties as Light-Emitting Materials and Recyclable Visible-Light Photocatalysts. *Macromolecules* **2016**, *49* (5), 1666–1673. https://doi.org/10.1021/acs.macromol.5b02511.

(15) Xie, Z.; Wang, C.; deKrafft, K. E.; Lin, W. Highly Stable and Porous Cross-Linked Polymers for Efficient Photocatalysis. *J. Am. Chem. Soc.* **2011**, *133* (7), 2056–2059. https://doi.org/10.1021/ja109166b.

(16) Xu, Y.; Zhang, F.; Feng, X. Patterning of Conjugated Polymers for Organic Optoelectronic Devices. *Small* **2011**, *7* (10), 1338–1360. https://doi.org/10.1002/smll.201002336.

(17) Cheng, Y.-J.; Yang, S.-H.; Hsu, C.-S. Synthesis of Conjugated Polymers for Organic Solar Cell Applications. *Chem. Rev.* **2009**, *109* (11), 5868–5923. https://doi.org/10.1021/cr900182s.

(18) Suh, M. P.; Park, H. J.; Prasad, T. K.; Lim, D.-W. Hydrogen Storage in Metal–Organic Frameworks. *Chem. Rev.* **2011**, *112* (2), 782–835. https://doi.org/10.1021/cr200274s.

(19) Makowski, P.; Thomas, A.; Kuhn, P.; Goettmann, F. Organic Materials for Hydrogen Storage Applications: From Physisorption on Organic Solids to Chemisorption in Organic Molecules. *Energy Environ. Sci.* **2009**, *2* (5), 480. https://doi.org/10.1039/b822279g.

(20) Unterlass, M. Geomimetics and Extreme Biomimetics Inspired by Hydrothermal Systems—What Can We Learn from Nature for Materials Synthesis? *Biomimetics* **2017**, *2* (4), 8. https://doi.org/10.3390/biomimetics2020008.

(21) Baumgartner, B.; Bojdys, M. J.; Unterlass, M. M. Geomimetics for Green Polymer Synthesis: Highly Ordered Polyimides via Hydrothermal Techniques. *Polym. Chem.* **2014**, *5* (12), 3771–3776. https://doi.org/10.1039/c4py00263f.

(22) Unterlass, M. M. Hot Water Generates Crystalline Organic Materials. *Angew. Chemie Int. Ed.* **2018**, *57* (9), 2292–2294. https://doi.org/10.1002/anie.201713359.

(23) Barbour, L. J. Crystal Porosity and the Burden of Proof. *Chem. Commun.* **2006**, No. 11, 1163–1168. https://doi.org/10.1039/b515612m.

(24) Flanigen, E. M. Chapter 2 Zeolites and Molecular Sieves an Historical Perspective. *Studies in Surface Science and Catalysis*. Elsevier 1991, pp 13–34. https://doi.org/10.1016/s0167-2991(08)63599-5.

(25) Rouquerol, J.; Avnir, D.; Fairbridge, C. W.; Everett, D. H.; Haynes, J. M.; Pernicone, N.; Ramsay, J. D. F.; Sing, K. S. W.; Unger, K. K. Recommendations for the

Characterization of Porous Solids (Technical Report). *Pure Appl. Chem.* **1994**, *66* (8), 1739–1758. https://doi.org/10.1351/pac199466081739.

(26) Sing, K. S. W.; Everett, D. H.; Haul, R. A. W.; Moscou, L.; Pierotti, R. A.; Rouquerol, J.; Siemieniewska, T. Reporting Physisorption Data for Gas/Solid Systems. In *Handbook of Heterogeneous Catalysis*; Wiley-VCH Verlag GmbH & Co. KGaA, 2008. https://doi.org/10.1002/9783527610044.hetcat0065.

(27) Cundy, C. S.; Cox, P. A. The Hydrothermal Synthesis of Zeolites: History and Development from the Earliest Days to the Present Time. *Chem. Rev.* **2003**, *103* (3), 663–702. https://doi.org/10.1021/cr020060i.

(28) Park, D. H.; Kim, S. S.; Wang, H.; Pinnavaia, T. J.; Papapetrou, M. C.; Lappas, A. A.; Triantafyllidis, K. S. Selective Petroleum Refining Over a Zeolite Catalyst with Small Intracrystal Mesopores. *Angew. Chemie Int. Ed.* **2009**, *48* (41), 7645–7648. https://doi.org/10.1002/anie.200901551.

(29) Zhao, D.; Yuan, D.; Zhou, H.-C. The Current Status of Hydrogen Storage in Metal–Organic Frameworks. *Energy Environ. Sci.* **2008**, *1* (2), 222. https://doi.org/10.1039/b808322n.

(30) Tsyurupa, M. P.; Davankov, V. A. Hypercrosslinked Polymers: Basic Principle of Preparing the New Class of Polymeric Materials. *React. Funct. Polym.* **2002**, *53* (2–3), 193–203. https://doi.org/10.1016/s1381-5148(02)00173-6.

(31) Cooper, A. I. Conjugated Microporous Polymers. *Adv. Mater.* **2009**, *21* (12), 1291–1295. https://doi.org/10.1002/adma.200801971.

(32) McKeown, N. B.; Gahnem, B.; Msayib, K. J.; Budd, P. M.; Tattershall, C. E.; Mahmood, K.; Tan, S.; Book, D.; Langmi, H. W.; Walton, A. Towards Polymer-Based Hydrogen Storage Materials: Engineering Ultramicroporous Cavities within Polymers of Intrinsic Microporosity. *Angew. Chemie Int. Ed.* **2006**, *45* (11), 1804–1807. https://doi.org/10.1002/anie.200504241.

(33) Cote, A. P. Porous, Crystalline, Covalent Organic Frameworks. *Science* **2005**, *310* (5751), 1166–1170. https://doi.org/10.1126/science.1120411.

(34) El-Kaderi, H. M.; Hunt, J. R.; Mendoza-Cortes, J. L.; Cote, A. P.; Taylor, R. E.; O'Keeffe, M.; Yaghi, O. M. Designed Synthesis of 3D Covalent Organic Frameworks. *Science* **2007**, *316* (5822), 268–272. https://doi.org/10.1126/science.1139915.

(35) Spitler, E. L.; Koo, B. T.; Novotney, J. L.; Colson, J. W.; Uribe-Romo, F. J.; Gutierrez, G. D.; Clancy, P.; Dichtel, W. R. A 2D Covalent Organic Framework with 4.7-Nm Pores and Insight into Its Interlayer Stacking. *J. Am. Chem. Soc.* **2011**, *133* (48), 19416–19421. https://doi.org/10.1021/ja206242v.

(36) Uribe-Romo, F. J.; Hunt, J. R.; Furukawa, H.; Klöck, C.; O'Keeffe, M.; Yaghi, O. M. A Crystalline Imine-Linked 3-D Porous Covalent Organic Framework. *J. Am. Chem. Soc.* **2009**, *131* (13), 4570–4571. https://doi.org/10.1021/ja8096256.

(37) Kandambeth, S.; Mallick, A.; Lukose, B.; Mane, M. V.; Heine, T.; Banerjee, R. Construction of Crystalline 2D Covalent Organic Frameworks with Remarkable Chemical (Acid/Base) Stability via a Combined Reversible and Irreversible Route. *J.*

Am. Chem. Soc. **2012**, *134* (48), 19524–19527. https://doi.org/10.1021/ja308278w.

(38) Kuhn, P.; Antonietti, M.; Thomas, A. Porous, Covalent Triazine-Based Frameworks Prepared by Ionothermal Synthesis. *Angew. Chemie Int. Ed.* **2008**, *47* (18), 3450–3453. https://doi.org/10.1002/anie.200705710.

(39) Fang, Q.; Zhuang, Z.; Gu, S.; Kaspar, R. B.; Zheng, J.; Wang, J.; Qiu, S.; Yan, Y. Designed Synthesis of Large-Pore Crystalline Polyimide Covalent Organic Frameworks. *Nat. Commun.* **2014**, *5* (1), 1–8. https://doi.org/10.1038/ncomms5503.

(40) Jin, E.; Li, J.; Geng, K.; Jiang, Q.; Xu, H.; Xu, Q.; Jiang, D. Designed Synthesis of Stable Light-Emitting Two-Dimensional Sp(2) Carbon-Conjugated Covalent Organic Frameworks. *Nat. Commun.* **2018**, *9* (1), 4143. https://doi.org/10.1038/s41467-018-06719-8.

(41) Fang, Q.; Gu, S.; Zheng, J.; Zhuang, Z.; Qiu, S.; Yan, Y. 3D Microporous Base-Functionalized Covalent Organic Frameworks for Size-Selective Catalysis. *Angew. Chemie Int. Ed.* **2014**, *53* (11), 2878–2882. https://doi.org/10.1002/anie.201310500.

(42) Furukawa, H.; Yaghi, O. M. Storage of Hydrogen, Methane, and Carbon Dioxide in Highly Porous Covalent Organic Frameworks for Clean Energy Applications. *J. Am. Chem. Soc.* **2009**, *131* (25), 8875–8883. https://doi.org/10.1021/ja9015765.

(43) Doonan, C. J.; Tranchemontagne, D. J.; Glover, T. G.; Hunt, J. R.; Yaghi, O. M. Exceptional Ammonia Uptake by a Covalent Organic Framework. *Nat. Chem.* **2010**, *2* (3), 235–238. https://doi.org/10.1038/nchem.548.

(44) Li, Z.; Zhang, Y.; Xia, H.; Mu, Y.; Liu, X. A Robust and Luminescent Covalent Organic Framework as a Highly Sensitive and Selective Sensor for the Detection of Cu2+ions. *Chem. Commun.* **2016**, *52* (39), 6613–6616. https://doi.org/10.1039/c6cc01476c.

(45) Nagai, A.; Guo, Z.; Feng, X.; Jin, S.; Chen, X.; Ding, X.; Jiang, D. Pore Surface Engineering in Covalent Organic Frameworks. *Nat. Commun.* **2011**, *2* (1), 536–538. https://doi.org/10.1038/ncomms1542.

(46) Ding, S.-Y.; Gao, J.; Wang, Q.; Zhang, Y.; Song, W.-G.; Su, C.-Y.; Wang, W. Construction of Covalent Organic Framework for Catalysis: Pd/COF-LZU1 in Suzuki–Miyaura Coupling Reaction. *J. Am. Chem. Soc.* **2011**, *133* (49), 19816–19822. https://doi.org/10.1021/ja206846p.

(47) Stegbauer, L.; Schwinghammer, K.; Lotsch, B. V. A Hydrazone-Based Covalent Organic Framework for Photocatalytic Hydrogen Production. *Chem. Sci.* **2014**, *5* (7), 2789–2793. https://doi.org/10.1039/c4sc00016a.

(48) Aiyappa, H. B.; Thote, J.; Shinde, D. B.; Banerjee, R.; Kurungot, S. Cobalt-Modified Covalent Organic Framework as a Robust Water Oxidation Electrocatalyst. *Chem. Mater.* **2016**, *28* (12), 4375–4379. https://doi.org/10.1021/acs.chemmater.6b01370.

(49) Lin, S.; Diercks, C. S.; Zhang, Y. B.; Kornienko, N.; Nichols, E. M.; Zhao, Y.; Paris, A. R.; Kim, D.; Yang, P.; Yaghi, O. M.; Chang, C. J. Covalent Organic Frameworks Comprising Cobalt Porphyrins for Catalytic CO2 Reduction in Water. *Science* **2015**, *349* (6253), 1208–1213. https://doi.org/10.1126/science.aac8343.

(50) Yadav, R. K.; Kumar, A.; Park, N.-J. J.; Kong, K.-J. J.; Baeg, J.-O. O. A Highly Efficient

Covalent Organic Framework Film Photocatalyst for Selective Solar Fuel Production from CO2. *J. Mater. Chem. A* **2016**, *4* (24), 9413–9418. https://doi.org/10.1039/c6ta01625a.

(51) Dalapati, S.; Jin, E.; Addicoat, M.; Heine, T.; Jiang, D. Highly Emissive Covalent Organic Frameworks. *J. Am. Chem. Soc.* **2016**, *138* (18), 5797–5800. https://doi.org/10.1021/jacs.6b02700.

(52) Xu, F.; Jin, S.; Zhong, H.; Wu, D.; Yang, X.; Chen, X.; Wei, H.; Fu, R.; Jiang, D. Electrochemically Active, Crystalline, Mesoporous Covalent Organic Frameworks on Carbon Nanotubes for Synergistic Lithium-Ion Battery Energy Storage. *Sci. Rep.* **2015**, *5*, 8225. https://doi.org/10.1038/srep08225.

(53) Liao, H.; Wang, H.; Ding, H.; Meng, X.; Xu, H.; Wang, B.; Ai, X.; Wang, C. A 2D Porous Porphyrin-Based Covalent Organic Framework for Sulfur Storage in Lithium–Sulfur Batteries. *J. Mater. Chem. A* **2016**, *4* (19), 7416–7421. https://doi.org/10.1039/c6ta00483k.

(54) Yaghi, O. M. Reticular Chemistry in All Dimensions. *ACS Cent. Sci.* **2019**, *5* (8), 1295–1300. https://doi.org/10.1021/acscentsci.9b00750.

(55) Davankov, V. A.; Tsyurupa, M. P. Structure and Properties of Hypercrosslinked Polystyrene—the First Representative of a New Class of Polymer Networks. *React. Polym.* **1990**, *13* (1–2), 27–42. https://doi.org/10.1016/0923-1137(90)90038-6.

(56) Jiang, J.-X.; Su, F.; Trewin, A.; Wood, C. D.; Campbell, N. L.; Niu, H.; Dickinson, C.; Ganin, A. Y.; Rosseinsky, M. J.; Khimyak, Y. Z.; Cooper, A. I. Conjugated Microporous Poly(Aryleneethynylene) Networks. *Angew. Chemie Int. Ed.* **2007**, *46* (45), 8574–8578. https://doi.org/10.1002/anie.200701595.

(57) Budd, P. M.; Ghanem, B. S.; Makhseed, S.; McKeown, N. B.; Msayib, K. J.; Tattershall, C. E. Polymers of Intrinsic Microporosity (PIMs): Robust, Solution-Processable, Organic Nanoporous Materials. *Chem. Commun.* **2004**, No. 2, 230. https://doi.org/10.1039/b311764b.

(58) Hernández, G.; Casado, N.; Zamarayeva, A. M.; Duey, J. K.; Armand, M.; Arias, A. C.; Mecerreyes, D. Perylene Polyimide-Polyether Anodes for Aqueous All-Organic Polymer Batteries. *ACS Appl. Energy Mater.* **2018**, *1* (12), 7199–7205. https://doi.org/10.1021/acsaem.8b01663.

(59) Volksen, W.; Miller, R. D.; Dubois, G. Low Dielectric Constant Materials. *Chem. Rev.* **2010**, *110* (1), 56–110. https://doi.org/10.1021/cr9002819.

(60) Gurchinoff, S.; Fish, D.; Stern, B. *High Performance Polymers for Small Engine Applications*; SAE International, 2013. https://doi.org/10.4271/2013-32-9012.

(61) McDanels, D. L.; Serafini, T. T.; DiCarlo, J. A. Polymer, Metal, and Ceramic Matrix Composites for Advanced Aircraft Engine Applications. *J. Mater. Energy Syst.* **1986**, *8* (1), 80–91. https://doi.org/10.1007/bf02833463.

(62) Hergenrother, P. M. The Use, Design, Synthesis, and Properties of High Performance/High Temperature Polymers: An Overview. *High Perform. Polym.* **2003**, *15* (1), 3–45. https://doi.org/10.1177/095400830301500101.

(63) Lee, J.; Kalin, A. J.; Yuan, T.; Al-Hashimi, M.; Fang, L. Fully Conjugated Ladder Polymers. *Chem. Sci.* **2017**, *8* (4), 2503–2521. https://doi.org/10.1039/c7sc00154a.

(64) Dawans, F.; Marvel, C. S. Polymers from Ortho Aromatic Tetraamines and Aromatic Dianhydrides. *J. Polym. Sci. Part A Gen. Pap.* **1965**, *3* (10), 3549–3571. https://doi.org/10.1002/pol.1965.100031019.

(65) Bell, V. L.; Pezdirtz, G. F. Polyimidazopyrrolones: A New Route to Ladder Polymer. *J. Polym. Sci. Part B Polym. Lett.* **1965**, *3* (12), 977–984. https://doi.org/10.1002/pol.1965.110031202.

(66) Bell, V. L. Preparation and Properties of Imide–Pyrone Copolymers. *J. Appl. Polym. Sci.* **1970**, *14* (9), 2385–2398. https://doi.org/10.1002/app.1970.070140917.

(67) Jiang, Z.; Jin, X.; Gao, X.; Zhou, W.; Lu, F.; Luo, Y. Thermal Degradation of Polybenzimidazopyrrolones. *J. Anal. Appl. Pyrolysis* **1995**, *33*, 231–242. https://doi.org/10.1016/0165-2370(94)00845-r.

(68) Zimmerman, C. M.; Koros, W. J. Polypyrrolones for Membrane Gas Separations. I. Structural Comparison of Gas Transport and Sorption Properties. *J. Polym. Sci. Part B Polym. Phys.* **1999**, *37* (12), 1235–1249. https://doi.org/10.1002/(sici)1099-0488(19990615)37:12<1235::aid-polb5>3.0.co;2-j.

(69) Jenekhe, S. A.; Tibbetts, S. J. Ion Implantation Doping and Electrical Properties of High-Temperature Ladder Polymers. *J. Polym. Sci. Part B Polym. Phys.* **1988**, *26* (1), 201–209. https://doi.org/10.1002/polb.1988.090260111.

(70) Babel, A.; Jenekhe, S. A. High Electron Mobility in Ladder Polymer Field-Effect Transistors. *J. Am. Chem. Soc.* **2003**, *125* (45), 13656–13657. https://doi.org/10.1021/ja0371810.

(71) Anastas, P. T.; Warner, J. C. Green Chemistry. Oxford University PressOxford 2000. https://doi.org/10.1093/oso/9780198506980.001.0001.

(72) Sheldon, R. A. The E Factor: Fifteen Years On. *Green Chem.* **2007**, *9* (12), 1273. https://doi.org/10.1039/b713736m.

(73) Unterlass, M. M. Creating Geomimetic Polymers. *Mater. Today* **2015**, *18* (5), 242–243. https://doi.org/10.1016/j.mattod.2015.02.013.

(74) Mizan, T. I.; Savage, P. E.; Ziff, R. M. Temperature Dependence of Hydrogen Bonding in Supercritical Water. *J. Phys. Chem.* **1996**, *100* (1), 403–408. https://doi.org/10.1021/jp951561t.

(75) Savage, P. E.; Rebacz, N. A. Water Under Extreme Conditions for Green Chemistry. In *Handbook of Green Chemistry*; Wiley-VCH Verlag GmbH & Co. KGaA, 2010. https://doi.org/10.1002/9783527628698.hgc057.

(76) Savage, P. E. Organic Chemical Reactions in Supercritical Water. *Chem. Rev.* **1999**, *99* (2), 603–622. https://doi.org/10.1021/cr9700989.

(77) Akiya, N.; Savage, P. E. Roles of Water for Chemical Reactions in High-Temperature Water. *Chem. Rev.* **2002**, *102* (8), 2725–2750. https://doi.org/10.1021/cr000668w.

(78) Quarch, K.; Kind, M. Inorganic Precipitated Silica Gel. Part 1: Gelation Kinetics and Gel Properties. *Chem. Eng. Technol.* **2010**, *33* (6), 1034–1039. https://doi.org/10.1002/ceat.201000080.

(79) Stock, N.; Biswas, S. Synthesis of Metal-Organic Frameworks (MOFs): Routes to Various MOF Topologies, Morphologies, and Composites. *Chem. Rev.* **2011**, *112* (2), 933–969. https://doi.org/10.1021/cr200304e.

(80) Byrappa, K.; Yoshimura, M. History of Hydrothermal Technology. *Handbook of Hydrothermal Technology*. Elsevier 2013, pp 51–73. https://doi.org/10.1016/b978-0-12-375090-7.00002-5.

(81) Rabenau, A. The Role of Hydrothermal Synthesis in Preparative Chemistry. *Angew. Chemie Int. Ed. English* **1985**, *24* (12), 1026–1040. https://doi.org/10.1002/anie.198510261.

(82) Cundy, C. S.; Cox, P. A. The Hydrothermal Synthesis of Zeolites: Precursors, Intermediates and Reaction Mechanism. *Microporous Mesoporous Mater.* **2005**, *82* (1–2), 1–78. https://doi.org/10.1016/j.micromeso.2005.02.016.

(83) WALKER, A. C. Hydrothermal Synthesis of Quartz Crystals. *J. Am. Ceram. Soc.* **1953**, *36* (8), 250–256. https://doi.org/10.1111/j.1151-2916.1953.tb12877.x.

(84) Laudise, R. A.; Ballman, A. A. Hydrothermal Synthesis of Sapphire1. *J. Am. Chem. Soc.* **1958**, *80* (11), 2655–2657. https://doi.org/10.1021/ja01544a014.

(85) Chiefari, J.; Dao, B.; Groth, A. M.; Hodgkin, J. H. Water as Solvent in Polyimide Synthesis: Thermoset and Thermoplastic Examples. *High Perform. Polym.* **2003**, *15* (3), 269–279. https://doi.org/10.1177/0954008303015003004.

(86) Chiefari, J.; Dao, B.; Groth, A. M.; Hodgkin, J. H. Water as Solvent in Polyimide Synthesis II: Processable Aromatic Polyimides. *High Perform. Polym.* **2006**, *18* (1), 31–44. https://doi.org/10.1177/0954008306055181.

(87) Chiefari, J.; Dao, B.; Groth, A. M.; Hodgkin, J. H. Water as Solvent in Polyimide Synthesis III: Towards the Synthesis of Polyamideimides. *High Perform. Polym.* **2006**, *18* (4), 437–451. https://doi.org/10.1177/0954008306064906.

(88) Baumgartner, B.; Puchberger, M.; Unterlass, M. M. Towards a General Understanding of Hydrothermal Polymerization of Polyimides. *Polym. Chem.* **2015**, *6* (31), 5773–5781. https://doi.org/10.1039/c5py00231a.

(89) Baumgartner, B.; Bojdys, M. J.; Skrinjar, P.; Unterlass, M. M. Design Strategies in Hydrothermal Polymerization of Polyimides. *Macromol. Chem. Phys.* **2016**, *217* (3), 485–500. https://doi.org/10.1002/macp.201500287.

(90) Taublaender, M. J.; Mezzavilla, S.; Thiele, S.; Glöcklhofer, F.; Unterlass, M. M. Hydrothermal Generation of Conjugated Polymers Using the Example of Pyrrone Polymers and Polybenzimidazoles. *Angew. Chem. Int. Ed. Engl.* **2020**, *59* (35), 15050–15060. https://doi.org/10.1002/anie.202000367.

(91) Stewart, D.; Antypov, D.; Dyer, M. S.; Pitcher, M. J.; Katsoulidis, A. P.; Chater, P. A.; Blanc, F.; Rosseinsky, M. J. Stable and Ordered Amide Frameworks Synthesised under Reversible Conditions Which Facilitate Error Checking. *Nat. Commun.* **2017**, *8* (1),

1102. https://doi.org/10.1038/s41467-017-01423-5.

(92)   Baumgartner, B.; Svirkova, A.; Bintinger, J.; Hametner, C.; Marchetti-Deschmann, M.; Unterlass, M. M. Green and Highly Efficient Synthesis of Perylene and Naphthalene Bisimides in Nothing but Water. *Chem. Commun.* **2017**, *53* (7), 1229–1232. https://doi.org/10.1039/c6cc06567h.

(93)   Taublaender, M. J.; Glöcklhofer, F.; Marchetti-Deschmann, M.; Unterlass, M. M. Green and Rapid Hydrothermal Crystallization and Synthesis of Fully Conjugated Aromatic Compounds. *Angew. Chem. Int. Ed. Engl.* **2018**, *57* (38), 12270–12274. https://doi.org/10.1002/anie.201801277.

(94)   Anbazhagan, R.; Dinh, T. T. Van; Krishnamoorthi, R.; Thankachan, D.; Tsai, H.-C.; Chang, Y.-H.; Yang, J.-M. Flower-Shaped Covalent Organic Framework Synthesis and Its Anticancer Drug Delivery Application. *Mater. Chem. Phys.* **2024**, *312* (October 2023), 128612. https://doi.org/10.1016/j.matchemphys.2023.128612.

(95)   Du, Y.; Mao, K.; Kamakoti, P.; Ravikovitch, P.; Paur, C.; Cundy, S.; Li, Q.; Calabro, D. Experimental and Computational Studies of Pyridine-Assisted Post-Synthesis Modified Air Stable Covalent–Organic Frameworks. *Chem. Commun.* **2012**, *48* (38), 4606. https://doi.org/10.1039/c2cc30781b.

(96)   Fang, Q.; Wang, J.; Gu, S.; Kaspar, R. B.; Zhuang, Z.; Zheng, J.; Guo, H.; Qiu, S.; Yan, Y. 3D Porous Crystalline Polyimide Covalent Organic Frameworks for Drug Delivery. *J. Am. Chem. Soc.* **2015**, *137* (26), 8352–8355. https://doi.org/10.1021/jacs.5b04147.

(97)   Ma, Y.; Liu, X.; Guan, X.; Li, H.; Yusran, Y.; Xue, M.; Fang, Q.; Yan, Y.; Qiu, S.; Valtchev, V. One-Pot Cascade Syntheses of Microporous and Mesoporous Pyrazine-Linked Covalent Organic Frameworks as Lewis-Acid Catalysts. *Dalt. Trans.* **2019**, *48* (21), 7352–7357. https://doi.org/10.1039/c8dt05056b.

(98)   Deblase, C. R.; Silberstein, K. E.; Truong, T. T.; Abruña, H. D.; Dichtel, W. R. B-Ketoenamine-Linked Covalent Organic Frameworks Capable of Pseudocapacitive Energy Storage. *J. Am. Chem. Soc.* **2013**, *135* (45), 16821–16824. https://doi.org/10.1021/ja409421d.

(99)   Waller, P. J.; Lyle, S. J.; Osborn Popp, T. M.; Diercks, C. S.; Reimer, J. A.; Yaghi, O. M. Chemical Conversion of Linkages in Covalent Organic Frameworks. *J. Am. Chem. Soc.* **2016**, *138* (48), 15519–15522. https://doi.org/10.1021/jacs.6b08377.

(100)   Han, X.; Huang, J.; Yuan, C.; Liu, Y.; Cui, Y. Chiral 3D Covalent Organic Frameworks for High Performance Liquid Chromatographic Enantioseparation. *J. Am. Chem. Soc.* **2018**, *140* (3), 892–895. https://doi.org/10.1021/jacs.7b12110.

(101)   Mujika, J. I.; Matxain, J. M.; Eriksson, L. A.; Lopez, X. Resonance Structures of the Amide Bond: The Advantages of Planarity. *Chem. - A Eur. J.* **2006**, *12* (27), 7215–7224. https://doi.org/10.1002/chem.200600052.

(102)   Tanner, D.; Fitzgerald, J. A.; Phillips, B. R. The Kevlar Story?An Advanced Materials Case Study. *Angew. Chemie Int. Ed. English* **1989**, *28* (5), 649–654. https://doi.org/10.1002/anie.198906491.

(103) Rajput, L.; Banerjee, R. Mechanochemical Synthesis of Amide Functionalized Porous Organic Polymers. *Cryst. Growth Des.* **2014**, *14* (6), 2729–2732. https://doi.org/10.1021/cg500439f.

(104) Hu, C.; Chen, L.; Gu, R.; Yu, J.; Zhu, J.; Hu, Z. Thermal Decomposition Behavior of a Heterocyclic Aramid Fiber. *J. Macromol. Sci. Part B* **2013**, *52* (5), 726–737. https://doi.org/10.1080/00222348.2012.725641.

(105) Vogel, H.; Marvel, C. S. Polybenzimidazoles, New Thermally Stable Polymers. *J. Polym. Sci.* **1961**, *50* (154), 511–539. https://doi.org/10.1002/pol.1961.1205015419.

(106) Lee, L.-H. Adhesives, Sealants, and Coatings for Space and Harsh Environments. In Adhesives, Sealants, and Coatings for Space and Harsh Environments; Springer US: Boston, MA, **1988**; pp 5–29. https://doi.org/10.1007/978-1-4613-1047-1_2.

(107) Powers, E. J.; Serad, G. A. History and Development of Polybenzimidazoles. In High Performance Polymers: Their Origin and Development; Springer Netherlands: Dordrecht, **1986**; pp 355–373. https://doi.org/10.1007/978-94-011-7073-4_34.

(108) Nandi, S.; Singh, S. K.; Mullangi, D.; Illathvalappil, R.; George, L.; Vinod, C. P.; Kurungot, S.; Vaidhyanathan, R. Low Band Gap Benzimidazole COF Supported Ni3N as Highly Active OER Catalyst. *Adv. Energy Mater.* **2016**, *6* (24), 1601189. https://doi.org/10.1002/aenm.201601189.

(109) Das, P.; Mandal, S. K. In-Depth Experimental and Computational Investigations for Remarkable Gas/Vapor Sorption, Selectivity, and Affinity by a Porous Nitrogen-Rich Covalent Organic Framework- SI. *Chem. Mater.* **2019**, *31* (5), 1584–1596. https://doi.org/10.1021/acs.chemmater.8b04683.

(110) Wang, P. L.; Ding, S. Y.; Zhang, Z. C.; Wang, Z. P.; Wang, W. Constructing Robust Covalent Organic Frameworks via Multicomponent Reactions. *J. Am. Chem. Soc.* **2019**, *141* (45), 18004-18008. https://doi.org/10.1021/jacs.9b10625.

(111) Bae, S.-Y. Y.; Kweon, D. H.; Mahmood, J.; Kim, M.-J. J.; Yu, S.-Y. Y.; Jung, S.-M. M.; Shin, S.-H. H.; Ju, M. J.; Baek, J.-B. B. Nitrogen-Rich Two-Dimensional Porous Polybenzimidazole Network as a Durable Metal-Free Electrocatalyst for a Cobalt Reduction Reaction in Organic Dye-Sensitized Solar Cells. *Nano Energy* **2017**, *34*, 533–540. https://doi.org/10.1016/j.nanoen.2017.03.023.

(112) Gole, B.; Stepanenko, V.; Rager, S.; Grüne, M.; Medina, D. D.; Bein, T.; Würthner, F.; Beuerle, F. Microtubular Self-Assembly of Covalent Organic Frameworks. *Angew. Chemie - Int. Ed.* **2018**, *57* (3), 846–850. https://doi.org/10.1002/anie.201708526.

(113) Crespy, D.; Bozonnet, M.; Meier, M. 100 Years of Bakelite, the Material of a 1000 Uses. *Angew. Chemie Int. Ed.* **2008**, *47* (18), 3322–3328. https://doi.org/10.1002/anie.200704281.

(114) Taublaender, M. J.; Reiter, M.; Unterlass, M. M. Highly Crystalline, Nanostructured Polyimide Microparticles via Green and Tunable Solvothermal Polymerization. *Macromolecules* **2019**, *52* (16), 6318–6329. https://doi.org/10.1021/acs.macromol.9b00985.

(115) Johnson, C. L.; Bagley, E. B.; Tolbert, T. L. High-Temperature Molding of Pyrrones. *Polym. Eng. Sci.* **1970***, 10* (6), 340–344. https://doi.org/10.1002/pen.760100606.

(116) Tao, L.; Yang, H.; Liu, J.; Fan, L.; Yang, S. Fluorinated Polybenzimidazopyrrolones with Excellent Alkaline-Hydrolysis Resistance. *J. Appl. Polym. Sci.* **2014***, 131* (6), n/a-n/a. https://doi.org/10.1002/app.40041.

(117) Walker, D. R. B.; Koros, W. J. Transport Characterization of a Polypyrrolone for Gas Separations. *J. Memb. Sci.* **1991***, 55* (1–2), 99–117. https://doi.org/10.1016/s0376-7388(00)82329-7.

(118) Abramovitch, R. A. Applications Of Microwave Energy In Organic Chemistry. A Review. *Org. Prep. Proced. Int.* **1991***, 23* (6), 683–711. https://doi.org/10.1080/00304949109458244.

(119) Sęk, D.; Schab-Balcerzak, E.; Grabiec, E. New Semiladder Polymers: 1. Synthesis and Properties of New Poly(Esterimidazopyrrolone)S. *Polymer (Guildf).* **1998***, 39* (26), 7001–7008. https://doi.org/10.1016/s0032-3861(98)00149-9.

(120) Sęk, D.; Schab-Balcerzak, E.; Grabiec, E. New Semiladder Polymers. Part II: Synthesis and Properties of New Poly(Amideimidazopyrrolones). *Polymer (Guildf).* **1999***, 40* (9), 2419–2428. https://doi.org/10.1016/s0032-3861(98)00447-9.

(121) Sęk, D.; Schab-Balcerzak, E.; Grabiec, E.; Volozhin, A.; Chamenko, T. New Semiladder Polymers: III. Synthesis and Properties of New Poly(Etherimidazopyrrolone)S. *Polymer (Guildf).* **2000***, 41* (1), 49–56. https://doi.org/10.1016/s0032-3861(99)00157-3.

(122) Alexander, L. X-Ray Diffraction Methods in Polymer Science. *J. Mater. Sci.* **1971***, 6* (1), 93–93. https://doi.org/10.1007/BF00550300.

(123) Zhu, S.; Hamielec, A. Polymerization Kinetic Modeling and Macromolecular Reaction Engineering. In Polymer Science: a Comprehensive Reference: Volume 1-10; Elsevier, **2012**; Vol. 1–10, pp 779–831. https://doi.org/10.1016/B978-0-444-53349-4.00127-8.

(124) Zhu, D.; Verduzco, R. Ultralow Surface Tension Solvents Enable Facile COF Activation with Reduced Pore Collapse. ACS Appl. Mater. & Interfaces 2020, 12 (29), 33121–33127. https://doi.org/10.1021/acsami.0c09173.

(125) Mohrig, J. R.; Hammond, C. N.; Schatz, P. F.; Morrill, T. C. Infrared Spectroscopy. In Techniques in Organic Chemistry: Miniscale, Standard Taper Microscale, and Williamson Microscale; W. H. Freeman and Co.: New York, **2003**; pp 277–314.

(126) Thommes, M.; Kaneko, K.; Neimark, A. V; Olivier, J. P.; Rodriguez-Reinoso, F.; Rouquerol, J.; Sing, K. S. W. Physisorption of Gases, with Special Reference to the Evaluation of Surface Area and Pore Size Distribution (IUPAC Technical Report). *Pure Appl. Chem.* **2015***, 87* (9–10), 1051–1069. https://doi.org/10.1515/pac-2014-1117.

(127) Shirley, D. A. High-Resolution X-Ray Photoemission Spectrum of the Valence Bands of Gold. *Phys. Rev. B* **1972***, 5* (12), 4709–4714. https://doi.org/10.1103/physrevb.5.4709.

(128)   Scofield, J. H. Hartree-Slater Subshell Photoionization Cross-Sections at 1254 and 1487 EV. *J. Electron Spectros. Relat. Phenomena* **1976**, *8* (2), 129–137. https://doi.org/10.1016/0368-2048(76)80015-1.

(129)   Wagner, C. D. NIST X-Ray Photoelectron Spectroscopy (XPS) Database; National Bureau of Standards, **1990**. https://doi.org/10.6028/nist.tn.1289.

(130)   Beamson, G.; Briggs, D. Appendices 3.1 and 3.2. In High resolution XPS of organic polymers : the Scienta ESCA300 database; Wiley, 1992.